Contents of issue 1 vol. LVI

HYDROMAGNETIC UNSTEADY MIXED CONVECTION AND MASS TRANSFER FLOW PAST A VERTICAL POROUS PLATE IMMERSED IN A POROUS MEDIUM WITH THE HALL EFFECT

B. K. S h a r m a [1], R. C. C h a u d h a r y [2]

[1] **Mathematics Group, Birla Institute of Technology and Science – Pilani**
Pilani (Rajasthan), India

[2] **Department of Mathematics, University of Rajasthan**
Jaipur-302004, India

The present work is concerned with unsteady mixed convection and mass transfer flow with Hall effect of an electrically conducting incompressible viscous fluid through a porous medium bounded by an infinite vertical plate subjected to suction/injection velocity in the presence of a constant magnetic field. The magnetic field is applied transversely to the direction of the flow. The resulting problem has been solved analytically and the solutions are found for velocity, temperature, concentration of the species, skin-friction, surface heat flux and mass flux. The effects of material parameters on the flow characteristics are expressed and illustrated/discussed by graphs and table.

Key words: Hall effect, porous medium, mixed convection, mass transfer.

NOTATIONS

H	applied magnetic field,
J	current density vector,
E	electric field,
e	charge of electron,
n_e	number density of electrons,
P_e	electron pressure,
$B_0 = \mu_e H_0$	magnetic field induction,
K	permeability of porous medium,
$m = \omega_e T_e$	Hall parameter,
κ	thermal conductivity,
T_∞	temperature of the fluid far away from the plate,
C_∞	concentration of the species far away from the plate,
B	induced magnetic field,
V	velocity vector,
g	acceleration due to gravity,
C_p	specific heat of the fluid at constant pressure,
M	magnetic field parameter,
Pr	Prandtl number,
Sc	Schmidt number,

G	Grashof number,
Gc	modified Grashof number,
θ	non-dimensional temperature,
C	non-dimensional concentration,
D	the chemical molecular diffusivity,
t	non-dimensional time,
T	reference temperature,
u	x-component of flow velocity,
v	y-component of flow velocity,
w	z-component of flow velocity,
x, y, z	Cartesian co-ordinate system,
V_0	injection velocity,
ω_e	cyclotron frequency,
τe	electron collision time,
μ	coefficient of viscosity of the fluid,
μe	magnetic permeability,
ρ	density of the fluid,
σ	electrical conductivity,
ν	kinematic viscosity,
β	free convection term,
β^*	volumetric coefficient,
η	modified y-coordinate,
Ω	frequency parameter,
ω	angular frequency,
Ψ	velocity function,
γ	phase angle for temperature field,
τ_1	skin friction along x-axis,
τ_2	skin friction along z-axis,
r	real part,
i	imaginary part.

1. Introduction

The phenomenon of heat and mass transfer has been the object of extensive research due to its applications in science and technology. Such phenomenon is observed in buoyancy – induced motions in the atmosphere, in bodies of water, quasi-solid bodies such as earth and so on. Some of the convective heat and mass transfer processes with phase change include the evaporation of a liquid at the interface between a gas and a liquid or the sublimation at a gas-solid interface. They can be described using the method for convective heat and mass transfer. Separation process in chemical engineering such as drying of solid materials, distillation, extraction and absorption, are all affected by the process of mass transfer. They also play a role in the production of materials in order to obtain the desired properties of a substance. Chemical reactions, including the combustion process, are often decisively determined by mass transfer. As examples of these types of processes, the evaporation, condensations, distillation, rectification and absorption of a fluid should all be mentioned (Baehr [1]).

The requirements of modern technology have stimulated interest in fluid flow studies which involve the interaction of several phenomena. One of them is related to the effect of free convection flow through a porous medium which plays an important role in agriculture, engineering, petroleum industries and heat transfer. The convection problem in a porous medium has also important applications in geothermal reservoirs and geothermal energy extractions. In order to utilize the geothermal energy to a maximum, one should have a complete and precise knowledge of the amount of perturbations needed to generate the convection currents in geothermal fluids. A comprehensive review of the studies of convective heat transfer mechanism through porous media has been made by NIELD and BEJAN [2]. Free convection flow past a vertical plate has been studied extensively by OSTRACH [3–6], RILEY et al. [7], DEY et al. [8], KAWOSE et al. [9], WEISS et al. [10] and PANTOKRATORAS [11] in numerous ways to include various physical aspects. GALLAHAN et al. [12], SOUNDALGEKAR et al. [13, 14], KHAIR et al. [15], LIN et al. [16, 17] and RAPTIS [18] have also studied the combined effect of thermal and mass diffusion along the vertical plate in numerous ways. The problem of magnetohydrodynamic viscous flow through porous medium past a vertical plate has been studied by TAKHAR et al. [19], ALCHAR et al. [20], ALDOSS et al. [21], SINGH et al. [22], SATTAR et al. [23], K.A. HELMY [24], with different physical conditions.

Important progress has been made during the last few decades in the development of magnetohydrodynamics due to its importance in engineering applications. The interest in these new problems stems from their importance in liquid metals, electrolytes and ionized gases. The thermal physics of MHD processes and MHD mass transfer are of interest in power engineering and metallurgy. The boundary zone between hydraulics and thermal physics is the area of many cross galvano and thermomagnetic effects. These phenomena are important in the study of semiconductor materials. In magnetohydrodynamics, serious attention has been given only to the transverse galvanomagnetic effect, i.e. the Hall effect: crossed phenomena also occur in the interaction of heat and mass transfer and hydraulics and mass transfer processes. The mechanism of conduction in ionized gases (low density) in presence of strong magnetic field is different from that in a metallic substance. The electric current in ionized gas is usually carried by electrons which undergo successive collisions with other charged or neutral particles. In case of ionized gas, the current is not proportional to the applied potential except when the electric field is very weak. When the electric field is strong, the conductivity parallel to the electric field is reduced and current is induced in the direction normal to both the electric and magnetic fields. This phenomenon is known as the Hall effect. The effect can be taken into account within the range of magnetohydrodynamical approximation.

The Hall effect on the fluid with variable concentration has a lot of applications in MHD power generations, several astrophysical and meteorological studies as well as in flow of plasma through MHD power generators. From the point of view of applications, model studies on the Hall effect on the free and forced convection flows have been made by several investigators. Some of them are DATTA et al. [25], ACHARYA et al. [26–27] and BISWAL [28]. However, the authors [25–28] studied the Hall effect on convection and mass transfer flow past a porous plate only, while [28] considered the effect of Hall on free convection flow of a visco-elastic fluid.

The problem investigated here is the study of the Hall effect on the combined heat and mass transfer unsteady flow, which occur due to buoyancy forces caused by thermal diffusion (temperature differences) and mass diffusion (concentration differences) of comparable magnitude, past a vertical porous plate which is immersed in porous medium with a constant magnetic field applied perpendicular to the plate. The plate is kept at the oscillating temperature and concentration.

2. FORMULATION

Consider the unsteady flow of a viscous incompressible and electrically conducting fluid past an infinite vertical porous plate in presence of transverse magnetic field. The x-axis is chosen along the plate in the upward direction while the y-axis is chosen normal to it and pointing away from the plate surface. All the properties of the fluid are assumed to be constant, except the body force term causing the buoyancy effect. The effect of Hall current gives rise to a force in the z-direction which induces a cross-flow in that direction. Thus the flow becomes three-dimensional. The physical configuration considered here is shown in the figure A. The equation governing the flow of fluid together with Maxwell's electromagnetic equations are as follows:

Continuity equation

$$(2.1) \qquad\qquad\qquad \nabla.\mathbf{V} = 0,$$

Momentum equation

$$(2.2) \quad \frac{\partial \mathbf{V}}{\partial t} + (\mathbf{V}.\nabla)\mathbf{V} = -\frac{1}{\rho}\nabla P + \nu\nabla^2\mathbf{V} + g\beta(T - T_\infty) + g\beta^*(C - C_\infty) + \frac{1}{\rho}(\mathbf{J}\times\mathbf{B}),$$

Energy equation

$$(2.3) \qquad\qquad\qquad \frac{\partial T}{\partial t} + (\mathbf{V}.\nabla)T = \kappa\nabla^2 T,$$

Generlized Ohm's Law

$$(2.4) \qquad \mathbf{J} = \sigma(\mathbf{E} + \mathbf{V} \times \mathbf{B}) - \frac{\sigma}{en_e}(\mathbf{J} \times \mathbf{B} - \nabla P_e),$$

Maxwell's equation

$$(2.5) \qquad \nabla \times \mathbf{H} = \mathbf{J}, \qquad \nabla \times \mathbf{E} = 0, \qquad \nabla.\mathbf{B} = 0.$$
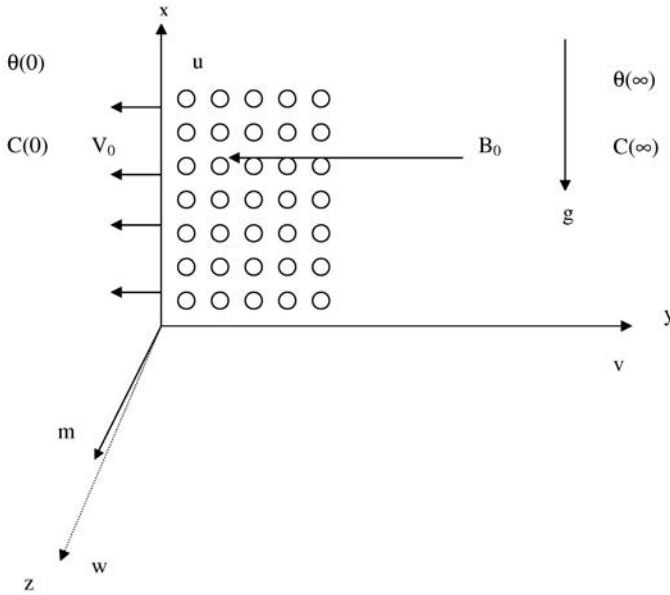

Fig. A. Physical model of the problem.

By assuming a very small magnetic Reynolds number, the induced magnetic field is neglected [29] in comparison to the applied magnetic field, so that $\mathbf{B} = (0, B_0, 0)$. Since no applied or polarization voltage is imposed on the flow field, the electric field vector $\mathbf{E} = 0$. This then corresponds to the case when no energy is added or extracted from the fluid by the electric field. The equation of conservation of electric charge $\nabla.\mathbf{J} = 0$ gives $J_y = $ constant, where $\mathbf{J} = (J_x, J_y, J_z)$. As the plate is non-conducting, $J_y = 0$ at the plate and hence vanishes everywhere. Considering the magnetic field strength to be very large, the corresponding generalized Ohm's law in the absence of electric field takes the following form:

$$(2.6) \qquad \mathbf{J} + \frac{\omega_e \tau_e}{B_0}(\mathbf{J} \times \mathbf{B}) = \sigma \left(\mathbf{V} \times \mathbf{B} + \frac{\nabla P_e}{en_e} \right).$$

For weakly ionized gases, the electron pressure gradient and ion slip effects (arising out of imperfect coupling between ions and neutrals) are neglected. Then Eq. (2.6) reduces to

(2.7)
$$J_x = \frac{\sigma B_0}{1+m^2}(mu - w),$$

$$J_z = \frac{\sigma B_0}{1+m^2}(u + mw).$$

The equations of motion, energy and concentration governing the flow under the usual Boussinesq approximation are:

Momentum equations

(2.8) $$\frac{\partial u}{\partial t} + v\frac{\partial u}{\partial y} = \nu\frac{\partial^2 u}{\partial y^2} - \frac{\sigma B_0^2(u + mw)}{\rho(1+m^2)} + g\beta(T - T_\infty) + g\beta^*(C - C_\infty) - \frac{\nu u}{K},$$

(2.9) $$\frac{\partial w}{\partial t} + v\frac{\partial w}{\partial y} = \nu\frac{\partial^2 w}{\partial y^2} + \sigma\frac{B_0^2(mu - w)}{\rho(1+m^2)} - \frac{\nu w}{K},$$

Energy equation

(2.10) $$\frac{\partial}{\partial t}(T - T_\infty) + v\frac{\partial(T - T_\infty)}{\partial y} = \frac{\kappa}{\rho C_p}\frac{\partial^2(T - T_\infty)}{\partial y^2},$$

Concentration equation

(2.11) $$\frac{\partial}{\partial t}(C - C_\infty) + v\frac{\partial(C - C_\infty)}{\partial y} = \frac{D\partial^2(C - C_\infty)}{\partial y^2}.$$

In Eq. (2.10), the viscous dissipation and Ohmic dissipation are neglected and in Eq. (2.11), the term due to chemical reaction is assumed to be absent. Now using $v = -V_0$ in Eqs. (2.8) and (2.9), $T(y,t) - T_\infty = \theta(y,t)$ in Eq. (2.10) and $C(y,t) - C_\infty = C^*(y,t)$ in Eq. (2.11), subjected to the initial boundary conditions

(2.12)
$$t \leq 0: \quad u(y,t) = w(y,t) = 0, \quad \theta = 0, \qquad C^* = 0 \qquad \text{for all } y,$$
$$t > 0: \begin{cases} u(0,t) = w(0,t) = 0, & \theta(0,t) = ae^{i\omega t}, \ C^*(0,t) = be^{i\omega t}, \ \text{at } y = 0, \\ u(\infty,t) = w(\infty,t) = 0, & \theta(\infty,t) = 0, \quad C^*(\infty,t) = 0 \quad \text{as } y \to \infty, \end{cases}$$

and using non-dimensional parameters

$$\eta = \frac{V_0 y}{\nu}, \qquad t' = \frac{V_0^2 t}{4\nu}, \qquad u' = \frac{u}{V_0}, \qquad w' = \frac{w}{V_0},$$

(2.13) $\quad \theta' = \dfrac{\theta}{a}, \qquad C' = \dfrac{C^*}{b}, \qquad G = \dfrac{4g\beta\nu a}{V_0^3}, \qquad Gc = \dfrac{4g\beta^*\nu b}{V_0^3},$

$$M = \frac{4\beta_0^2 \sigma \nu}{\rho V_0^3}, \qquad \Pr = \frac{\nu \rho C_p}{\kappa}, \qquad K' = \frac{V_0^2 K}{4\nu^2}, \qquad Sc = \frac{\nu}{D},$$

Eqs. (2.8) to (2.11) are transformed to their corresponding non-dimensional form (dropping the dashes) as

(2.14) $\qquad \dfrac{\partial u}{\partial t} - 4\dfrac{\partial u}{\partial \eta} = 4\dfrac{\partial^2 u}{\partial \eta^2} - \dfrac{M}{1+m^2}(mw+u) + G\theta + GcC - \dfrac{u}{K},$

(2.15) $\qquad \dfrac{\partial w}{\partial t} - 4\dfrac{\partial w}{\partial \eta} = 4\dfrac{\partial^2 w}{\partial \eta^2} + \dfrac{M}{1+m^2}(mu-w) - \dfrac{w}{K},$

(2.16) $\qquad \dfrac{\partial \theta}{\partial t} - 4\dfrac{\partial \theta}{\partial \eta} = \dfrac{4}{\Pr}\dfrac{\partial^2 \theta}{\partial \eta^2},$

(2.17) $\qquad \dfrac{\partial C}{\partial t} - 4\dfrac{\partial C}{\partial \eta} = \dfrac{4}{Sc}\dfrac{\partial^2 C}{\partial \eta^2}.$

The modified boundary conditions become

(2.18) $\begin{aligned} & t \leq 0: \quad u(\eta,t) = w(\eta,t) = 0, \quad \theta = 0, \qquad\qquad C = 0 \qquad\qquad \forall \eta, \\ & t > 0: \begin{cases} u(0,t) = w(0,t) = 0, \quad \theta(0,t) = e^{i\omega t}, \quad C(0,t) = e^{i\omega t}, \text{ at } \eta = 0, \\ u(\infty,t) = w(\infty,t) = 0, \; \theta(\infty,t) = 0, \qquad C(\infty,t) = 0 \qquad \text{as } \eta \to \infty, \end{cases} \end{aligned}$

3. SOLUTION

Equations (2.14) and (2.15) can be combined using the complex variable

(3.1) $$\Psi = u + iw$$

giving

(3.2) $\quad \dfrac{\partial^2 \Psi}{\partial \eta^2} + \dfrac{\partial \Psi}{\partial \eta} - \dfrac{1}{4}\dfrac{\partial \Psi}{\partial t} - \dfrac{1}{4}\left[\dfrac{M}{1+m^2}(1-im) + \dfrac{1}{K}\right]\Psi = -\dfrac{1}{4}G\theta - \dfrac{1}{4}GcC.$

Introducing the non-dimensional parameter $\Omega = \dfrac{4\nu\omega}{V_0^2}$ and using Eq. (3.1), the boundary conditions in (2.18) are transformed to

(3.3)
$$\Psi(0,t) = \Psi(\infty,t) = 0 \quad \text{and} \quad C(0,t) = e^{i\Omega t},$$
$$\theta(0,t) = e^{i\Omega t}, \quad \theta(\infty,t) = 0, \quad C(\infty,t) = 0.$$

Putting $\theta(\eta,t) = e^{i\Omega t} f(\eta)$ in Eq. (2.16), we get

(3.4)
$$f''(\eta) + \Pr f'(\eta) - \frac{i\Omega \Pr}{4} f(\eta) = 0,$$

which has to be solved under the boundary condition

(3.5)
$$f(0) = 1, \quad f(\infty) = 0.$$

Hence
$$f(\eta) = e^{-\frac{\eta}{2}\left[\Pr + \sqrt{\Pr^2 + i\Omega \Pr}\right]}$$

(3.6)
$$\Rightarrow \theta(\eta,t) = e^{i\Omega t - \frac{\eta}{2}\left[\Pr + \sqrt{\Pr^2 + i\Omega \Pr}\right]}.$$

Separating real and imaginary parts, the real part is given by

(3.7)
$$\theta_r(\eta,t) = \cos\left\{\Omega t - \frac{\eta}{2} R_1 \sin\frac{\alpha}{2}\right\} e^{-\frac{\eta}{2}\left(\Pr + R_1 \cos\frac{\alpha}{2}\right)}$$

where

(3.8)
$$R_1 = \Pr^{1/2}(\Pr^2 + \Omega^2)^{1/4},$$
$$\alpha = \tan^{-1}\left(\frac{\Omega}{\Pr}\right).$$

Putting $C(\eta,t) = e^{i\Omega t} g(\eta)$ in Eq. (2.17), we get

(3.9)
$$g''(\eta) + \mathrm{Sc}\, g'(\eta) - \frac{i\Omega \mathrm{Sc}}{4} g(\eta) = 0,$$

which has to be solved under the boundary condition

(3.10)
$$g(0) = 1, \quad g(\infty) = 0.$$

Hence
$$g(\eta) = e^{\frac{1}{2}\eta\left[-\mathrm{Sc} - \sqrt{\mathrm{Sc}^2 + i\Omega \mathrm{Sc}}\right]},$$

so that

(3.11) $$C(\eta, t) = e^{i\Omega t - \frac{\eta}{2}\left[\text{Sc} + \sqrt{\text{Sc}^2 + i\Omega\text{Sc}}\right]}.$$

Separating real and imaginary parts, the real part is given by

(3.12) $$C_r(\eta, t) = \cos\left\{\Omega t - \frac{\eta}{2}R_2 \sin\frac{\beta}{2}\right\} e^{-\frac{\eta}{2}\left(\text{Sc} + R_2 \cos\frac{\beta}{2}\right)},$$

where

$$R_2 = \text{Sc}^{1/2}(\text{Sc}^2 + \Omega^2)^{1/4},$$

(3.13)

$$\beta = \tan^{-1}\left(\frac{\Omega}{\text{Sc}}\right).$$

In order to solve Eq. (3.2), substituting $\Psi = e^{i\Omega t}f(\eta)$ and using boundary conditions

(3.14) $$F(0) = 0, \qquad F(\infty) = 0.$$

and then separating real and imaginary parts, we obtain

(3.15) $$u = \Big[\{A_{18}\eta_{12}\cos(A_{21}\eta/2) + A_{19}\sin(A_{21}\eta/2)\}e^{-A_{20}\eta/2}$$
$$- \{A_{22}\cos(\Omega t - A_3\eta/2)e^{-A_2\eta/2} + A_{23}\sin(\Omega t - A_3\eta/2)e^{-A_3\eta/2}\}A_{26}$$
$$- \{A_{24}\cos(\Omega t - A_{10}\eta/2)e^{-A_9\eta/2} + A_{25}\sin(\Omega t - A_{10}\eta/2)e^{-A_{10}\eta/2}\}A_{27}\Big]\cos\Omega t$$
$$- \Big[\{A_{19}\cos(A_{21}\eta/2) - A_{18}\sin(A_{21}\eta/2)\}e^{-A_{20}\eta/2}$$
$$- \{A_{22}\sin(\Omega t - A_3\eta/2)e^{-A_3\eta/2} - A_{23}\cos(\Omega t - A_3\eta/2)e^{-A_2\eta/2}\}A_{26}$$
$$- \{A_{24}\sin(\Omega t - A_{10}\eta/2)e^{-A_{10}\eta/2}$$
$$- A_{25}\cos(\Omega t - A_{10}\eta/2)e^{-A_9\eta/2}\}A_{27}\Big]\sin\Omega t,$$

(3.16) $$w = \Big[\{A_{18}\cos(A_{21}\eta/2) + A_{19}\sin(A_{21}\eta/2)\}e^{-A_{20}\eta/2}$$
$$- \{A_{22}\cos(\Omega t - A_3\eta/2)e^{-A_2\eta/2} + A_{23}\sin(\Omega t - A_3\eta/2)e^{-A_3\eta/2}\}A_{26}$$
$$- \{A_{24}\cos(\Omega t - A_{10}\eta/2)e^{-A_9\eta/2} + A_{25}\sin(\Omega t - A_{10}\eta/2)e^{-A_{10}\eta/2}\}A_{27}\Big]\sin\Omega t$$
$$+ \Big[\{A_{19}\cos(A_{21}\eta/2) - A_{18}\sin(A_{21}\eta/2)\}e^{-A_{20}\eta/2}$$
$$- \{A_{22}\sin(\Omega t - A_3\eta/2)e^{-A_3\eta/2} - A_{23}\cos(\Omega t - A_3\eta/2)e^{-A_2\eta/2}\}A_{26}$$
$$- \{A_{24}\sin(\Omega t - A_{10}\eta/2)e^{-A_{10}\eta/2}$$
$$- A_{25}\cos(\Omega t - A_{10}\eta/2)e^{-A_9\eta/2}\}A_{27}\Big]\sin\Omega t.$$

The shearing stress at the wall along the x-axis is given by

$$(3.17) \qquad \tau_1 = \left(\frac{\partial u}{\partial \eta}\right)_{\eta=0},$$

and the shearing stress at the wall along the z-axis is given by

$$(3.18) \qquad \tau_2 = \left(\frac{\partial w}{\partial \eta}\right)_{\eta=0},$$

The surface heat flux is given by

$$(3.19) \qquad Q(t) = \frac{1}{2}\left[\Pr\cos\Omega t + R_1\cos\left(\Omega t + \frac{\alpha}{2}\right)\right],$$

and the mass flux is given by

$$(3.20) \qquad C(t) = \frac{1}{2}\left[\mathrm{Sc}\cos\Omega t + R_2\cos\left(\Omega t + \frac{\beta}{2}\right)\right],$$

where

$$R_1 = \Pr{}^{1/2}(\Pr{}^2 + \Omega^2)^{1/4}, \qquad R_2 = \mathrm{Sc}^{1/2}(\mathrm{Sc}^2 + \Omega^2)^{1/4},$$

$$R_3 = \left[\left(\frac{1}{K}+1+\frac{M}{1+m^2}\right)^2 + \left(\Omega - \frac{Mm}{1+m^2}\right)^2\right]^{1/4},$$

$$\alpha = \tan^{-1}\left(\frac{\Omega}{\Pr}\right), \qquad \beta = \tan^{-1}\left(\frac{\Omega}{\mathrm{Sc}}\right), \qquad \gamma = \tan^{-1}\frac{\left(\Omega - \dfrac{Mm}{1+m^2}\right)}{A_1},$$

$$A_1 = \frac{1}{K}+1+\frac{M}{1+m^2}, \qquad A_2 = \Pr + R_1\cos\alpha/2, \qquad A_3 = R_1\sin\alpha/2,$$

$$A_4 = \frac{1}{K}+\frac{M}{1+m^2}, \qquad A_5 = \Omega - \frac{Mm}{1+m^2}, \qquad A_6 = (A_2^2 - A_3^2 - 2A_2 - A_4),$$

$$A_7 = (2A_2A_3 - 2A_3 - A_5), \qquad A_8 = A_6^2 + A_7^2, \qquad A_9 = \mathrm{Sc} + R_2\cos\beta/2,$$

$$A_{10} = R_2\sin\beta/2, \qquad A_{11} = (A_9^2 - A_{10}^2 - 2A_9 - A_4),$$

$$A_{12} = (2A_9A_{10} - 2A_{10} - A_5), \qquad A_{13} = (GA_6\cos\Omega t + GA_7\sin +\Omega t)A_{26},$$

$$A_{14} = (GA_6\sin\Omega t - GA_7\cos\Omega t)A_{26},$$

$$A_{15} = (GcA_{11}\cos\Omega t + GcA_{12}\sin\Omega t)A_{27},$$

$$A_{16} = (GcA_{11}\sin\Omega t - GcA_{12}\cos\Omega t)A_{27}, \qquad A_{17} = A_{11}^2 + A_{12}^2,$$

$$A_{18} = A_{13} + A_{15}, \qquad A_{19} = A_{14} + A_{16}, \qquad A_{20} = 1 + R_3 \cos\gamma/2,$$

$$A_{21} = R_3 \sin\gamma/2, \qquad A_{22} = GA_6, \qquad A_{23} = GA_7, \qquad A_{24} = GcA_{11},$$

$$A_{25} = GcA_{12}, \qquad A_{26} = 1/A_8, \qquad A_{27} = 1/A_{17}.$$

4. Results and discussion

A study of the velocity field, variations of temperature and concentration, shearing stresses, surface heat flux and mass flux in hydromagnetic mixed convective flow past an infinite vertical plate through porous medium with Hall effect, has been carried out in the preceding sections. Approximate solutions are obtained for various flow variables. In order to get insight into the physical situation of the problem, we have computed the numerical values of the velocity, temperature, concentration, shearing stress, surface heat flux and mass flux for different values of m (Hall parameter), M (Magnetic parameter), Sc (Schmidt number), Pr (Prandtl number) and Ω (Frequency parameter). The values of G (Grashof number for heat transfer) are taken equal to 5.0 (G > 0, cooled Newtonian fluid) and −5.0 (G < 0 heated Newtonian fluid). The values of modified Grashoff number (Gc, for mass transfer) Ωt and permeability (K) are taken equal to 2.0, $\pi/2$ and 1, respectively. The obtained numerical results are illustrated and tabulated in Figs. 1 to 10 and Table 1. The velocity components, temperature and concentration versus η are shown in Figs. 1 to 6, but shearing stress versus m are shown in Fig. 7 to 10.

Table 1. Variations of $C(t)$ and $Q(t)$ for different values of Ω, Sc and Pr.

Ω	$C(t)$			$Q(t)$		
	Sc = 0.22	Sc = 0.30	Sc = 0.78	Pr = 0.025	Pr = 0.71	Pr = 7.0
0	0.22	0.30	0.78	0.025	0.71	7.0
0.2	0.08	0.12	0.38	0.012	0.34	3.74
0.4	−0.17	−0.21	−0.41	−0.011	−0.38	−3.00
0.6	−0.27	−0.35	−0.81	−0.024	−0.74	−6.95
0.8	−0.08	−0.12	0.39	−0.013	−0.35	−4.42
1.0	0.21	0.26	0.44	0.011	0.42	2.22

Figures 1 and 2 depict the velocity component u for a cooled Newtonian fluid (G > 0) and for a heated Newtonian fluid (G < 0), respectively. It is drawn for Pr = 0.71 (Prandtl number for air at 20°C) and Pr = 7.0 (Prandtl number for water at 20°C), taking different values of m, M, Ω and Sc. It is observed that an
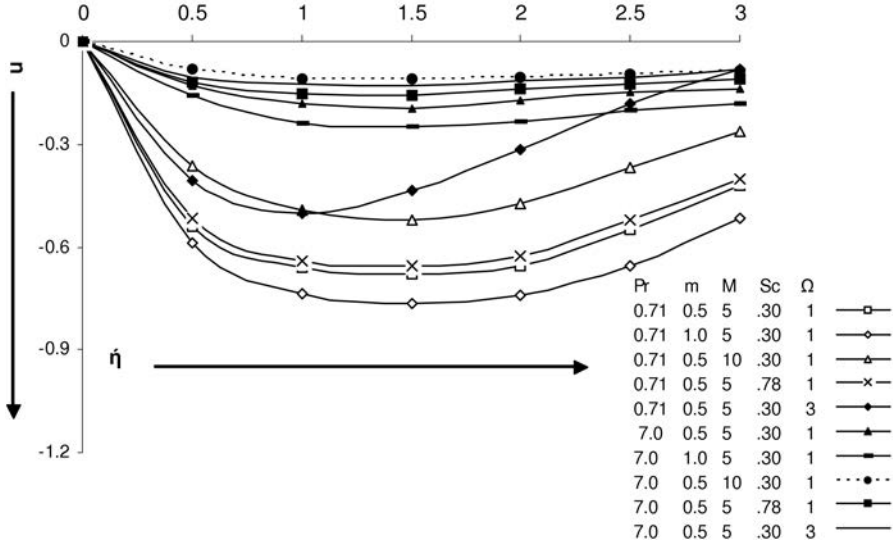
Pr	m	M	Sc	Ω	
0.71	0.5	5	.30	1	—□—
0.71	1.0	5	.30	1	—◇—
0.71	0.5	10	.30	1	—△—
0.71	0.5	5	.78	1	—×—
0.71	0.5	5	.30	3	—◆—
7.0	0.5	5	.30	1	—▲—
7.0	1.0	5	.30	1	—■—
7.0	0.5	10	.30	1	···●···
7.0	0.5	5	.78	1	—■—
7.0	0.5	5	.30	3	———

FIG. 1.   Variation of velocity component u for Gc $= 2.0$, G $= 5.0$, $\Omega t = \pi/2$.

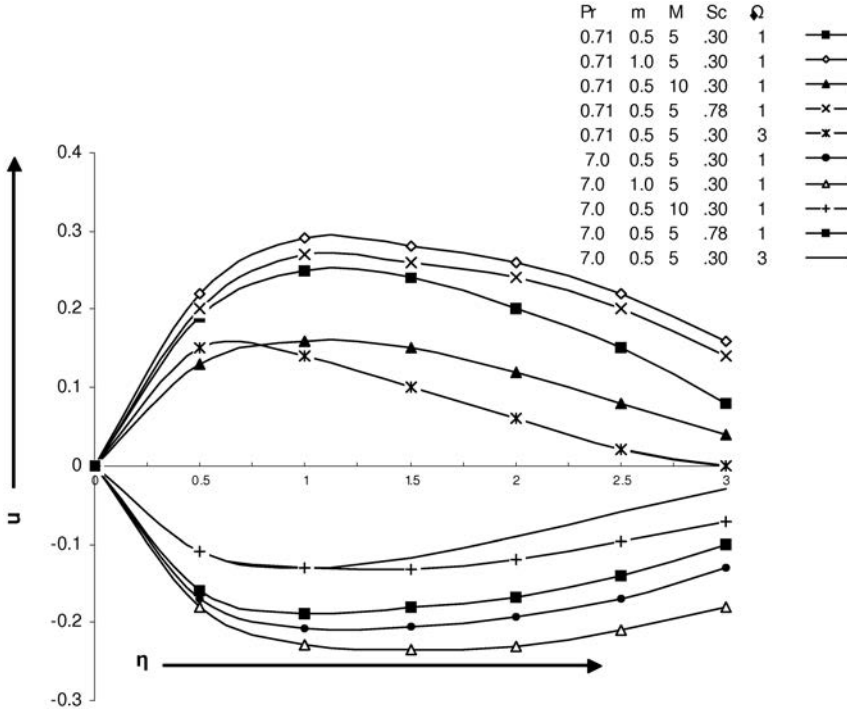| Pr	m	M	Sc	Ω	
0.71	0.5	5	.30	1	—■—
0.71	1.0	5	.30	1	—◇—
0.71	0.5	10	.30	1	—▲—
0.71	0.5	5	.78	1	—×—
0.71	0.5	5	.30	3	—×—
7.0	0.5	5	.30	1	—●—
7.0	1.0	5	.30	1	—△—
7.0	0.5	10	.30	1	—+—
7.0	0.5	5	.78	1	—■—
7.0	0.5	5	.30	3	———

FIG. 2.   Variation of velocity component u for Gc $= 2.0$, G $= -5.0$, $\Omega t = \pi/2$.

increase in the Hall parameter leads to decrease in the velocity for both air and water in a cooled Newtonian fluid. For a heated Newtonian fluid, the velocity increases with increasing Hall parameter (m) for air, but in the case of water, a reverse effect is observed. It is noticed that an increase in the magnetic parameter (M) leads to a rise in the velocity for both air and water for an externally cooled (Gr > 0) plate. In the case of externally heated plate (Gr < 0) and Pr = 0.71 (air), we have observed that an increase in the magnetic parameter decreases the velocity, while a reverse effect is noticed in water (Pr = 7.0). The velocity is greater for Ammonia (Sc = 0.78, at temperature 25°C and 1 atmosphere) than that of Helium (Sc = 0.30, at temperature 25°C and 1 atmosphere) for Pr = 0.71 or 7.0 and G > or < 0. We also observe that an increase in the frequency parameter (Ω) gives rise to the velocity for air/water and G > 0. For the heated plate in the air, it is found that an increase in Ω leads to a fall in the values of the velocity, while a reverse effect is observed for water. Further, it is noticed that the velocity distribution increases/decreases gradually near the plate ($0 < \eta \leq 1$) and then decreases/increases slowly far away from the plate ($\eta \gg 1$). A comparative study of the curves reveals that the values of the velocity increase/decrease at each point with variations in m or M or Sc or Ω or Pr. It is concluded that the maximum/minimum of the velocity occurs in the vicinity of the plate and the rise and fall in the values of the velocity are more dominant in the case of air (Pr = 0.71) than those of water (Pr = 7.0). The velocity profiles remain negative for Gr > 0 (cooled Newtonian fluid) and positive for G < 0 (heated Newtonian fluid) in the case of Pr = 0.71 near the plate and fade far away from the plate. However, in the case when Pr = 7.0, the velocity profiles remain negative for cooled/heated fluid. In all the situations, the velocity profiles remain always in phase.

The velocity component w has been shown in Figs. 3 and 4 for cooled Newtonian fluid (G > 0) and heated Newtonian fluid (G < 0), respectively. An increase in the Hall parameter leads to an increase in the velocity for both air and water in a cooled Newtonian fluid. For a heated Newtonian fluid, the velocity decreases with increasing Hall parameter for air, while reverse effect is observed in the case of water. It is observed that an increase in the magnetic parameter (M) leads to a rise in the velocity for both air and water for externally cooled (G > 0) plate. For an increasing M, there is a fall in the velocity for air but a rise in the case of water for externally heated plate (G < 0). The velocity is greater for Ammonia than that for Helium with Pr = 0.71 or 7.0 and G > 0 or G < 0. Increasing Ω, the velocity decreases for air and water and G > 0. When G < 0 and Ω is increasing, w increases for Pr = 0.71, while it decreases for Pr = 7.0. The maximum/minimum of w occurs away from the plate ($\eta > 1$) and becomes almost constant as we move farther from the plate. The w remains positive in a Newtonian cooled fluid for both Pr = 0.71 or 7.0. For G < 0 (heated
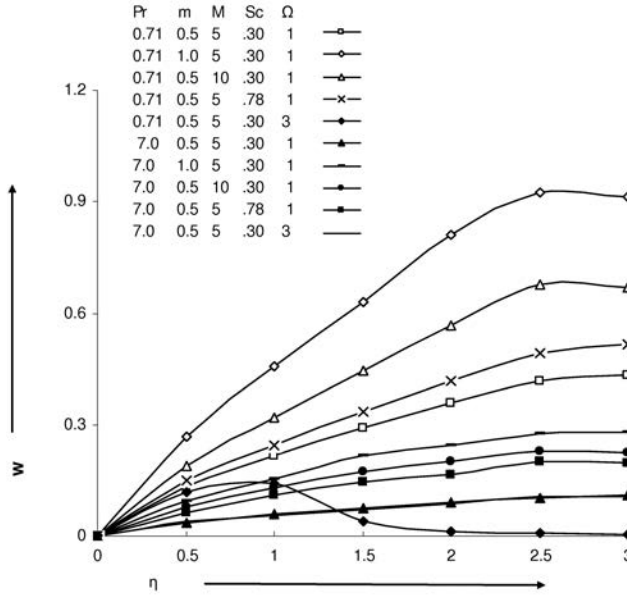
FIG. 3. Variation of velocity component w for Gc $= 2.0$, G $= 5.0$, $\Omega t = \pi/2$.
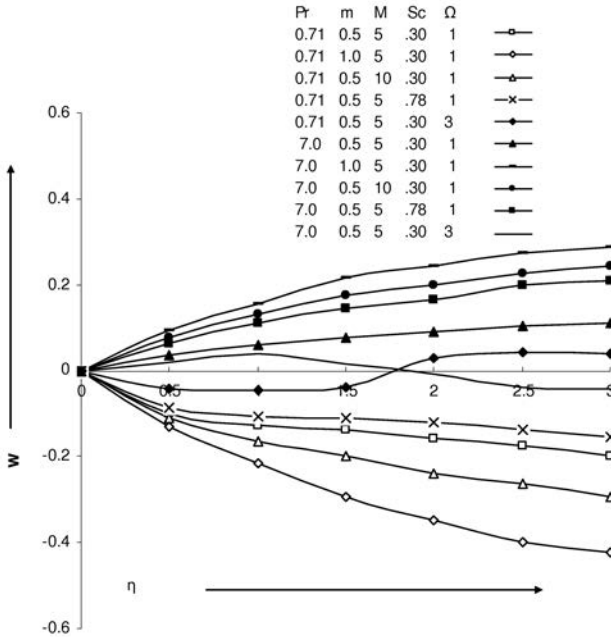

FIG. 4. Variation of velocity component w for Gc $= 2.0$, G $= -5.0$, $\Omega t = \pi/2$.

Newtonian fluid), the w remains negative for $Pr = 0.71$, while it is positive for $Pr = 7.0$. However, for increasing Ω, its value oscillates between negative and positive values for $G < 0$.

The variation of temperature θ_r has been shown in Fig. 5 for $Pr = 0.71$ (air) and $Pr = 7.0$ (water) and for different values of Ω. It is noticed that an increase in Ω leads to a rise in the temperature for both air and water. It is observed that maximum of θ_r occurs more quickly in water than that in air, in the neighbourhood of the plate and as the distance from the plate increases it decays faster in water than in air. An increase in Ω gives a rise in θ_r at each point. Figure 6 depicts the variation of concentration Cr for Helium ($Sc = 0.30$) and Ammonia ($Sc = 0.78$) for different values of Ω. An increase in Ω leads to a rise in Cr for both Helium and Ammonia. A comparative study of the curves reveals that the values of Cr increase/decrease at each point with variation in Ω and the same pattern is found as that of θ_r. It is further observed that the values of Cr are higher in Ammonia (heavier particles) than in Helium (lighter particles) near the plate ($0 < \eta < 1$). The shearing stress τ_1 is presented in Figs. 7 and 8 for cooled Newtonian fluid ($G > 0$) and heated Newtonian fluid ($G < 0$), respectively. τ_1 is drawn for $Pr = 0.71$ and $Pr = 7.0$, taking different values of M and Sc as a function of m. It is observed that for increasing M that the τ_1 first increases, reaches a maximum (at $m = 0.2$) and then becomes constant for $G > 0$ both in air and water. For extremely heated plate, the values of τ_1 first decrease, reach a minimum (at $m = 0.2$) and then become constant for large values of M in air, but a reverse effect is observed for water. We have
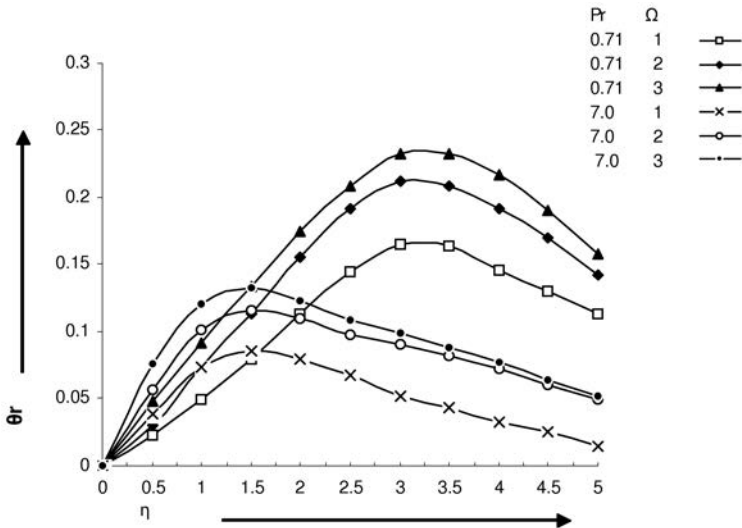

FIG. 5. Variation of temperature θ_r.

noticed that the values of τ_1 are greater for Helium than Ammonia, for both air and water and $G > 0$ or $G < 0$. Further, it is found that the values of τ_1 are smaller in air than in water for cooled Newtonian fluid, while a reverse effect is observed for a heated Newtonian fluid. Also, the values of τ_1 increase/decrease for small values of m and then remain constant for $m \geq 0.2$.
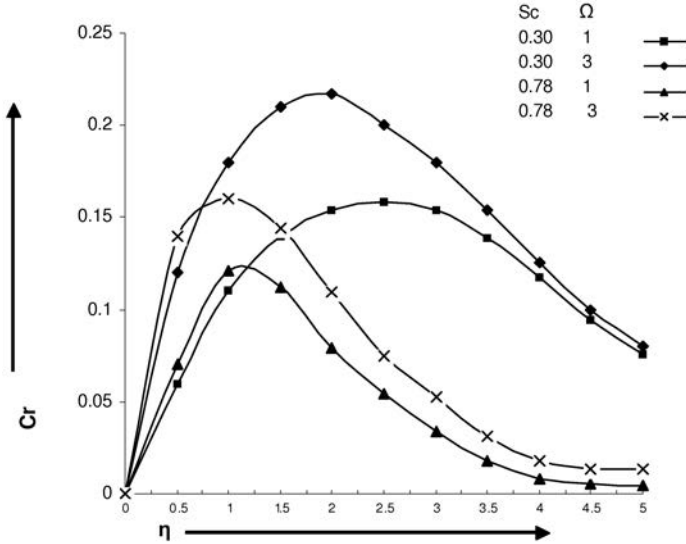
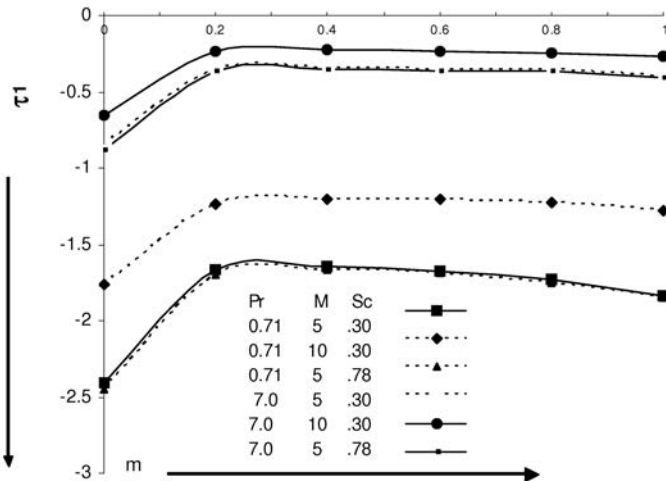FIG. 6. Variation of concentration Cr.

FIG. 7. Variation of shearing stress τ_1 for $Gc = 2.0$, $G = 5.0$, $\Omega t = \pi/2$.
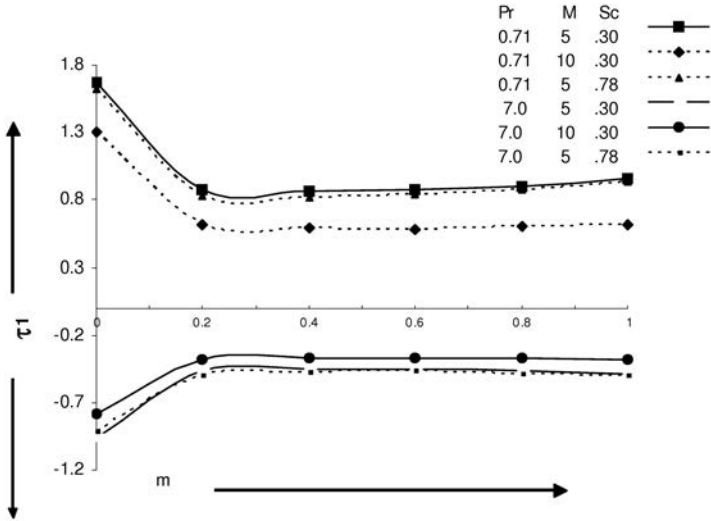
Pr	M	Sc
0.71	5	.30
0.71	10	.30
0.71	5	.78
7.0	5	.30
7.0	10	.30
7.0	5	.78

FIG. 8. Variation of shearing stress τ_1 for Gc $= 2.0$, G $= -5.0$, $\Omega t = \pi/2$.

Figures 9 and 10 depict the variation of the shearing stress τ_2 for different values of M, Sc and Pr versus the Hall parameter (m). It is observed that an increase in M leads to a fall in τ_2 for both air and water and G > 0. However, the values of the skin friction are greater in air than those of water for small Hall parameter, but for large parameter a reverse effect is observed. For G < 0 and
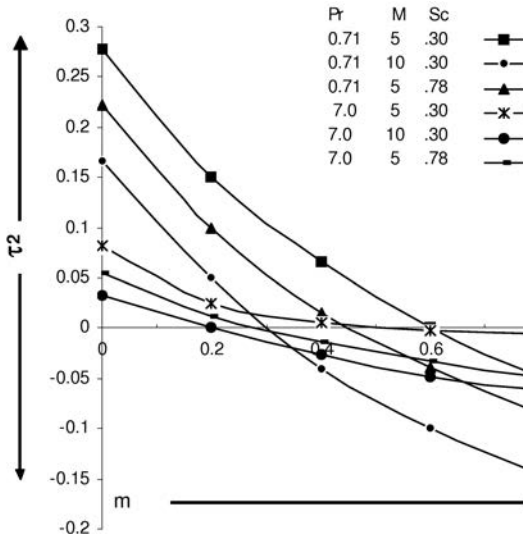

Pr	M	Sc
0.71	5	.30
0.71	10	.30
0.71	5	.78
7.0	5	.30
7.0	10	.30
7.0	5	.78

FIG. 9. Variation of shearing stress τ_2 for Gc $= 2.0$, G $= 5.0$, $\Omega t = \pi/2$.

$Pr = 0.71$ it is found that for increasing M, the values of τ_2 rise, while a reverse effect is observed for water. The effect of small induced magnetic field is greater for $Pr = 7.0$ than that for $Pr = 0.71$. We have found that the values of τ_2 are greater in Helium than in Ammonia for air or water and $G > 0$ or $G < 0$. For large induced magnetic field ($m \geq 1$) the skin friction becomes almost constant in all situations.
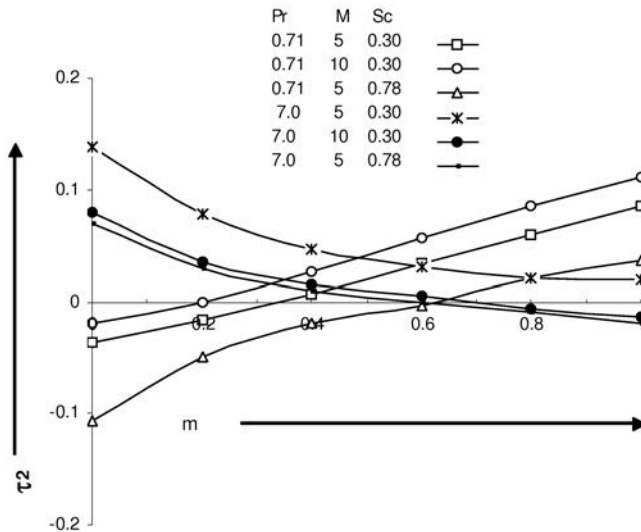

Pr	M	Sc	
0.71	5	0.30	—□—
0.71	10	0.30	—○—
0.71	5	0.78	—△—
7.0	5	0.30	—×—
7.0	10	0.30	—●—
7.0	5	0.78	—•—

FIG. 10. Variation of shearing stress τ_2 for $Gc = 2.0$, $G = -5.0$, $\Omega t = \pi/2$.

One would also certainly like to know the quantity of heat exchange between the body and the fluid. The heat flux across the surface $Q(t)$ is given in the table for different values of $Pr = 0.025$ (Mercury), 0.71 (air) and 7.0 (water). The variation of $Q(t)$ is reported for various values of Ω (frequency). It is noted that for increasing Prandtl number, the flux increases for small values of the frequency. However, it oscillates i.e. it increases/decreases with the increasing values of Ω or Pr. The mass flux across the surface $C(t)$ is also given in the table for different values of $Sc = 0.22$ (Hydrogen), 0.30 (Helium) and 0.78 (Ammonia). The variation of $C(t)$ is reported for various values of Ω (frequency). It is noticed that for increasing Sc, the flux increases for small values of the frequency, however it oscillates, i.e. it increases/decreases with the increasing values of Ω or Sc.

5. CONCLUSIONS

In this work the problem of unsteady mixed convection and mass transfer flow with Hall effect of a viscous, electrically conducting fluid through a porous

medium, bounded by an infinite vertical plate under the action of a uniform transverse magnetic field is investigated. The resulting governing equations are solved by a perturbation scheme. The results are presented for variations of major parameters, including the magnetic field parameter, the Prandtl number, the Grashof number, the Schmidt number and Hall parameter. A systematic study of the effects of the various parameters of flow, heat and mass flux characteristics is carried out. Some of the important findings, obtained from the graphs and table are listed here with:

1. An increase in magnetic parameter (M) or Hall parameter (m) leads to a rise in the velocity for both air and water for a cooled Newtonian fluid.
2. The velocity is higher for Ammonia than that for Helium with Pr = 0.71 or 7.0 and G > 0 or G < 0.
3. For a cooled Newtonian fluid, an increase in frequency parameter (Ω) gives a rise in the velocity for both air and water.
4. The values of concentration (Cr) are higher in Ammonia than that in Helium near the plate.
5. An increase in Ω leads to a rise in the temperature and concentration for air/water and Helium/Ammonia, respectively.
6. The values of shearing stresses are greater in Helium than in Ammonia for air or water and G > 0 or G < 0.
7. The mass flux across the surface oscillates with increasing Ω or Sc.
8. The heat flux across the surface oscillates with increasing Ω or Pr.

It is hoped that the present investigation of the study of physics of flow over a vertical surface can be utilized, as the basis for many scientific and engineering applications, for studying more complex problems involving the flow of electrically conducting fluids. The findings may be useful for the study of movement of oil or gas and water through the reservoir of oil or gas field, in migration of underground water and in the filtration and water purification processes. The results of the problem are also of great interest in geophysics in the study of interaction of the geomagnetic field with the fluid in the geothermal region.

REFERENCES

1. H. D. BAEHR, K. STEPHAN, *Heat and mass transfer*, Springer-Verlag, Berlin 1998.

2. D. A. NIELD, A. BEJAN, *Convection in porous media*, 2-nd edition, Springer Verlarg, Berlin 1998.

3. S. OSTRACH, *Laminar natural convection flow and heat transfer of fluids with and without heat sources in channels with wall temperatures*, NACA TN No. 2863, 1952.

4. Ibid, *An analysis of laminar free-convection flow and heat transfer about a flat plate parallel to the direction of the generating body force*, NACA TN No. 1111, 1953.

5. Ibid, *New aspects of natural convection heat transfer*, Trans. Am. Soc. Mech. Eng., **75**, 1287, 1953.

6. Ibid, *Unstable convection in vertical channels with heating from below, including effects of heat source and frictional heating*, NACA TN, No. 3458, 1955.

7. D. S. RILEY, D. G. DRAKE, *Higher approximations to the free convection flow from a heated vertical flat plate*, Appl. Sci. Res., **30**, 193, 1975.

8. J. DEY, G. NATH, *Mixed convection flow on vertical surfaces*, Wärme und Stoffübertragung, **15**, 279, 1981.

9. Y. KAWOSE, J. J. ULBRECHT, *Approximate solution to the natural convection heat transfer from a vertical plate*, Int. Comm. Heat Mass Transfer, **11**, 143, 1984.

10. Y. WEISS, Y. AHORAN, I. SHAI, *Natural convection on a vertical flat plate of general boundary conditions*, Heat Transfer 1994, Proc. Int. Heat Transfer Conference, 7, 179, 1994.

11. A. PANTOKRATORAS, *Laminar free convection over a vertical isothermal plate with uniform blowing or suction in water with variable physical properties*, Int. J. Heat Mass Transfer, **45**, 963, 2002.

12. G. D. GALLAHAN, W. J. MARNER, *Transient free convection with mass transfer on an isothermal flat plate*, Int. J. Heat Mass Transfer, **19**, 165, 1976.

13. V. M. SOUNDALGEKAR, P. GANESAN, *Finite difference analysis of transient free convection with mass transfer on an isothermal vertical flat plate*, Int. J. Engineering Science, **19**, 757, 1981.

14. V. M. SOUNDALGEKAR, P. D. WARVE, *Unsteady free convection flow past an infinite vertical plate with constant suction and mass transfer*, Int. J. Heat Mass Transfer, **20**, 1363, 1977.

15. K. R. KHAIR, A. BEJAN, *Mass transfer to natural convection boundary layer flow driven by heat transfer*, ASME J. of Heat Transfer, **107**, 979, 1985.

16. H. T. LIN, C. M. WU, *Combined heat and mass transfer by laminar natural convection from a vertical plate with uniform heat flux and concentration*, Heat and Mass Transfer, **32**, 293, 1997.

17. Ibid, *Combined heat and mass transfer by laminar natural convection from a vertical plate*, Heat and Mass Transfer, **30**, 369, 1995.

18. A. A. RAPTIS, *Free convection and mass transfer effects on the flow past an infinite moving vertical porous plate with constant suction and heat source*, Astrophys. Space Sci., **86**, 43, 1982.

19. H. S. Takhar, P. C. Ram, *Magnetohydrodynamic free convection flow of water at 4° C through a porous medium*, Int. J. Heat Mass Transfer, **21**, 371, 1994.

20. S. Alchar, P. Vasseur, E. Bilgen, *Effects of a magnetic field on the onset of convection in a porous medium*, Heat Mass Transfer, **30**, 259, 1995.

21. T. K. Aldoss, M. A. Alnimr, M. A. Jarrah, B. J. Alshear, *Magnetohydrodynamic mixed convection from a vertical plate embedded in a porous medium*, Numer. Heat Transfer A, **28**, 635, 1995.

22. N. P. Singh, Ajay Kumar, Yadav Manoj Kumar, Singh Atul Kumar, *Hydromagnetic free convective and mass transfer flow of a viscous stratified liquid*, J. of Energy, Heat and Mass transfer, **21**, 111, 1999.

23. Md. Abdus Sattar, M. Mansur Rahman, Md. Mahmud Alam, *Free convection flow and heat transfer through a porous vertical flat plate immersed in a porous medium with variable suction*, J. of Energy, Heat and Mass Transfer, **22**, 17, 2000.

24. K. A. Helmy, *Unsteady free convection flow past a vertical porous plate*, ZAMM, **78**, 4, 255, 1998.

25. N. Datta, R. N. Jana, *Oscillatory magnetohydrodynamic flow past a flat plate with Hall effects*, Jour. Phys. Soc. Japan, **40**, 1469, 1976.

26. M. Acharya, G. C. Dash, L. P. Singh, *Effect of chemical and thermal diffusion with Hall current on unsteady hydromagnetic flow near an infinite vertical porous plate*, J. Phys. D: Appl. Phys., **28**, 2455, 1995.

27. M. Acharya, G. C. Dash, L. P. Singh, *Hall effect with simultaneous thermal and mass diffusion on unsteady hydromagnetic flow near an accelerated vertical plate*, Indian J. of Physics B, **75B** 1, 168, 2001.

28. S. Biswal, P. K. Sahoo, *Hall effect on oscillatory hydromagnetic free convective flow of a visco-elastic fluid past an infinite vertical porous flat plate with mass transfer*, Proc. Nat. Acad. Sci., **69(A)**, 46, 1999.

29. G. W. Suttan, A. Sherman, *Engineering Magnetohydrodynamics*, McGraw-Hill, New York 1965.

THE FIRST HALF-TURN OF AN INERTIAL VIBRATOR

G. C i e p l o k

AGH University of Science and Technology
Department of Mechanics and Vibroacoustics
Al. Mickiewicza 30, 30-059 Kraków, Poland

The paper concerns the starting of an inertial vibrator which, due to a high value of static unbalance, is unable to perform the first half-turn in the gravitational field of force. The problem plays an essential role in the selection of driving units for the wide class of over–resonance machines.

On the basis of the Pontryagin's Maximum Principle the problem was formulated in terms of a dynamic optimisation. Thus, the driving moment performs the function of control – which is being looked for – while equations of motion and start-end conditions related to the position of a vibrator, act as constrains equations and boundary conditions. The possible simplifications in description of the motion of the vibrator, as well as the influence of the variable asynchronous motor driving moment on the optimal solutions, are discussed in the paper. On the basis of the work-energy equivalence principle, the minimum values of the driving moment – which warrants the performance of the first half-turn of the vibrator at a given number of the moment switch-overs – were determined. The problem of thermal loads of the motor during the first half-turn was also considered. The theoretical results were confirmed by the computer simulations.

Key words: starting, vibratory machine, dynamic optimisation.

1. Introduction

The problem of selecting the driving unit power is very important for a wide class of over-resonance vibrating machines, such as: conveyers, screens, tables, grids etc. The demand for the driving moment for these machines is related to the need of overcoming two critical states. The first state concerns the necessity to surmount the gravitational force of an unbalanced mass during the first half-turn, while the second state corresponds to overcoming the rapidly increased resistance to motion during passing through the resonance zone. The estimated – in such a way – driving unit power exceeds, in many cases, several times the power demand for realization of the in-coming steady state. In the steady state, the energy dissipation occurs due to the technological or transporting processes, due to overcoming the resistance to the motion of vibrators and elements of machine suspension, or losses related to the driving moment transmission. The problem has been repeatedly pointed out and discussed in scientific papers. For example, the paper by Banaszewski [2], describes the start of the one- and two-mass

vibrator at the given moment of force and the resistances from the rolling friction and bearing seal. MICHALCZYK [8] determined the minimum value of the moment of force:

$$(1.1) \qquad\qquad\qquad M_{\min} = 0.7246 \, meg \, ,$$

which allows to perform the first half-turn when the motor starts from the arrested lowest position (me – static unbalance of a vibrator, g – gravitational acceleration). However, the approaches applied in the papers mentioned above were restricted to the vibrator model presented as a pendulum – at the assumption that the value of the driving moment as well as its sense are constant.

2. PROBLEM FORMULATED IN TERMS OF THE MAXIMUM PRINCIPLE

Let us consider the problem in a more general way. Thus, *let us find the form of the moment acting on the vibrator shaft, which will allow to move the centre of its mass from the lower to upper position – without imposing at that moment any limitations concerning the value and direction of operation.* It is obvious that there is an infinite number of such forms; however, only some of them can are of practical significance. The selection of the criterion deciding upon the chosen solution is an open problem. However, it should be taken into account that not all criteria are useful. E.g. an instinctively appearing criterion related to minimalisation of the work being done by the driving moment, when applied to the loss-less model of a physical pendulum, will not provide the expected results. The optimal solution can be easily guessed since it is related to the state, in which the kinetic energy is zeroing at the upper position of the vibrator. But again – such a state can be obtained by an unlimited number of measures. This diversity of solutions requires either imposing of an additional condition on the criterion or the task formulation in the form of a multi-optimisation expression.

The most reasonable and convenient criterion seems to be the time-minimal criterion, which:

1. Provides directly an explicit solution.
2. Due to the time decrease in which the driving motor is present within the range of short-circuit currents, it directly causes lowering of the heat produced in rotor windings.

Thus the origin for further considerations becomes the form quality functional (2.1) as well as the equations of motion of the vibrating machine (2.2) – the model of which is presented in Fig. 1.

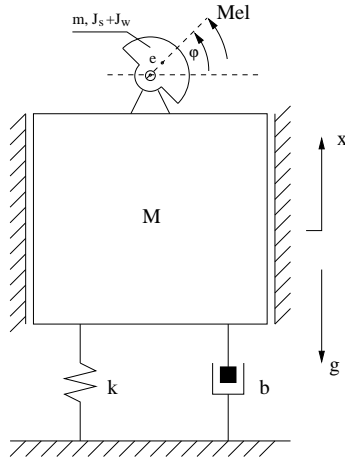$$(2.1) \qquad\qquad\qquad T = \int_{t=0}^{t=t_k} dt \rightarrow \min \, ,$$

FIG. 1. The vibrating machine model.

$$(2.2) \quad \begin{aligned} (M + m)\ddot{x} + me\ddot{\varphi}\cos(\varphi) - me\dot{\varphi}^2\sin(\varphi) + b\dot{x} + kx = 0, \\ (J_s + me_w^2 + J_w)\ddot{\varphi} + me\ddot{x}\cos(\varphi) = M_{el} - mge\cos(\varphi), \end{aligned}$$

J_s – central moment of the vibrator inertia, J_w – axial moment of the motor rotor inertia.

The problem presented hereby can be formulated and solved by means of the theory of calculus of variations, based on the Pontryagin's Maximum Principle. Due to the reasons of the presentation clarity, two variants of the problem will be discussed in the paper. At first the simplified variant – in which mutual interactions of the machine body and the vibrator are disregarded – will be presented. In this variant, the mechanical system becomes a physical pendulum subjected to the influence of the gravitational field and to the moment – which is being looked for. Later on, the second variant, that takes into account the previously omitted interactions and which is based on Eqs. (2.3) – will be discussed.

2.1. Simplified variant

On the basis of equations of motion of the pendulum (2.3) being subjected to the influence of $M(t)$ moment and referring to the Maximum Principle [4], the Hamiltonian function – due to the criterion (2.1) – takes the form given by Eq. (2.4).

$$(2.3) \quad \begin{aligned} \frac{d\omega}{dt} &= \frac{1}{J_{zr}}\left(M(t) - mge\sin(\varphi)\right), \\ \frac{d\varphi}{dt} &= \omega, \end{aligned}$$
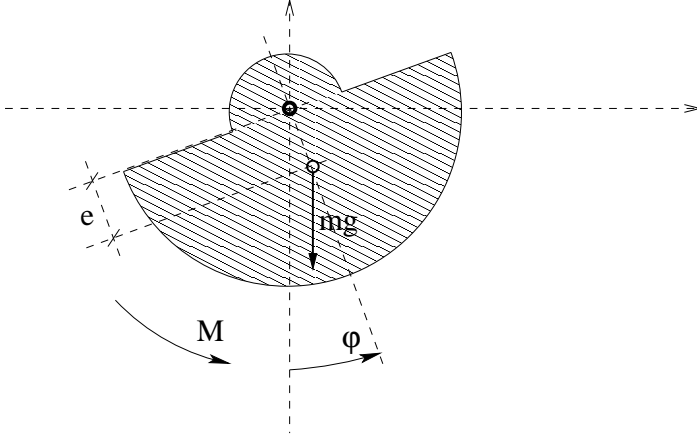
Fig. 2. Inertial vibrator model presented in the form of a physical pendulum.

$$(2.4) \qquad H = \frac{\Psi_1}{J_{zr}}\left(M(t) - mge\sin(\varphi)\right) + \omega\Psi_2 - 1.$$

The Hamiltonian function linear dependence on the $M(t)$ value implicates immediately the form of the moment maximising the Hamiltonian along the optimal trajectory to the trajectory contained within the boundary of variability of the force moment. Thus, limiting the $M(t)$ moment to the set:

$$(2.5) \qquad M(t) \subset [-M_0, +M_0]$$

we may observe that:

$$(2.6) \qquad M(t) = M_0 \cdot \mathrm{sgn}(\Psi_1),$$

where M_0 is given value.

On the grounds of the conditions necessary for existing of the Hamiltonian extremum, the system (2.3) can be supplemented with equations for the coupled functions Ψ_1, Ψ_2:

$$(2.7) \qquad \begin{aligned} \frac{d\Psi_1}{dt} &= -\frac{\partial H}{\partial \omega} = -\Psi_2, \\[2mm] \frac{d\Psi_2}{dt} &= -\frac{\partial H}{\partial \varphi} = \frac{mge\cos(\varphi)\Psi_1}{J_{zr}}. \end{aligned}$$

In turn, due to the time-minimal variant of the Maximum Principle, the final positions of coupled functions should fulfil the transversality conditions, which – in a general form [1] – can be written as:

$$(2.8) \qquad \bar{\Psi}^* = \sum_{\alpha=1}^{m} k_\alpha \frac{\partial g_\alpha[\bar{x}^*, t_k^*]}{\partial \bar{x}^*[t_k^*]},$$

where $g_\alpha[x^*(t_k), t_k^*]$ – equations imposed on the motion coordinates at time $t = t_k^*$.

In the problem discussed hereby, we have only one condition imposed on the final positions of the motion coordinates:

(2.9)
$$g_1 : \varphi^*(t_k^*) - \pi = 0$$

and on its basis we determine:

$$\Psi_1^*(t_k^*) = k_1 \frac{\partial g_1}{\partial \omega} = 0,$$

(2.10)

$$\Psi_2^*(t_k^*) = k_1 \frac{\partial g_1}{\partial \varphi} = k_1,$$

where k_1 – certain constant.

The fact of explicit independence of the final conditions of the time imposes one additional condition on the Hamilton's function: zeroing of its value along the optimal trajectory.

Thus, supplementing the final conditions (2.10) with conditions at the start:

(2.11)
$$\omega^*(0) = 0,$$
$$\varphi^*(0) = 0,$$

and condition of zeroing of the Hamiltonian e.g. at $t = t_k$:

(2.12)
$$H(t_k^*) = 0$$

we obtain the set of dependences needed for an explicit solution of systems (2.3) and (2.7).

The task being considered here belongs to the so-called two-point boundary value problems, which in a general case cannot be solved by traditional methods of numerical integration and requires a special approach. However, the preliminary analysis provides already some interesting conclusions.

Using the Eq. (2.7) we obtain the following equation:

(2.13)
$$\frac{d^2\Psi_1}{dt^2} + \frac{mge}{J_{zr}}\Psi_1 \cos(\varphi) = 0$$

which, for small values of φ angle, becomes a homogeneous differential equation with constant coefficients. One can state – on its basis – that the time form of the moment is a switch-over type function with the switching frequency being equal to the double frequency of the pendulum free vibrations:

(2.14)
$$f_0 = \frac{1}{\pi}\sqrt{\frac{mge}{J_{zr}}}.$$

The system (2.7) – for any chosen value of angle φ – can be solved e.g. by application of the gradient shooting method [6].

Applying such an approach, the problem was solved for two values of moment M_0, namely for $M_0 = 16.47$ [Nm] and $M_0 = 65.88$ [Nm]. The values $J_{zr} = 1.98$ [kg m^2], $m_w = 382.3$ [kg], $e = 0.04$ [m] were assumed for the pendulum.

The solution for the first M_0 value is presented in Fig. 3. As it can be seen from the graph, the moment changes its sign eight times and finally, the angle
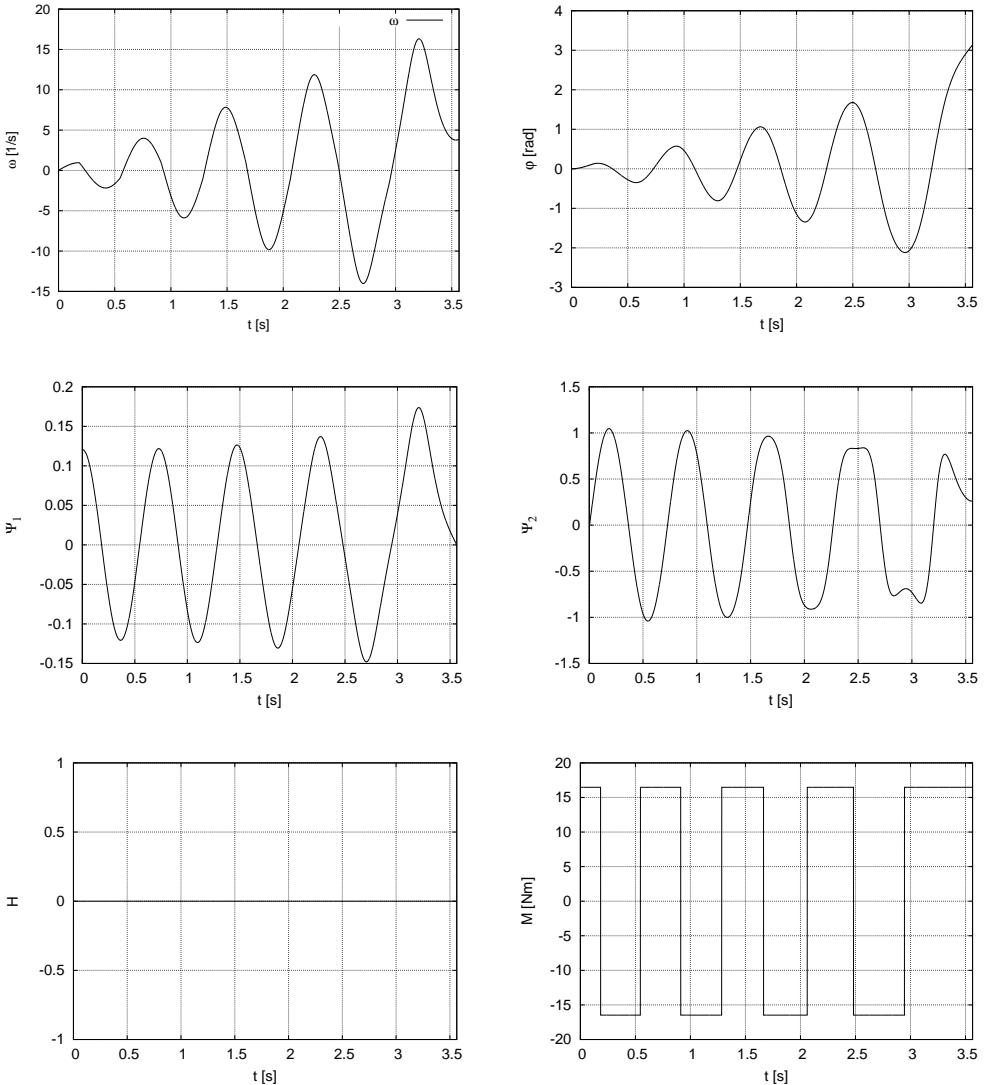

FIG. 3. Graphical presentation of solutions for the set of Eqs. (2.3) and (2.7), for $M_0 = 16.47$ [Nm].

coordinate φ reaches the value π. In accordance with Eq. (2.6), the time when the coupled coordinate Ψ_1 passes zero indicates the switch-over time and equals successively: 0.185 [s], 0.548 [s], 0.914 [s], 1.286 [s], 1.666 [s], 2.064 [s], 2.484 [s] and 2.947 [s].

The solution for the second M_0 value (being 4 times larger then the previous one) is presented in Fig. 4. In this case the moment changes its sign only once at $t = 0.36$ [s].
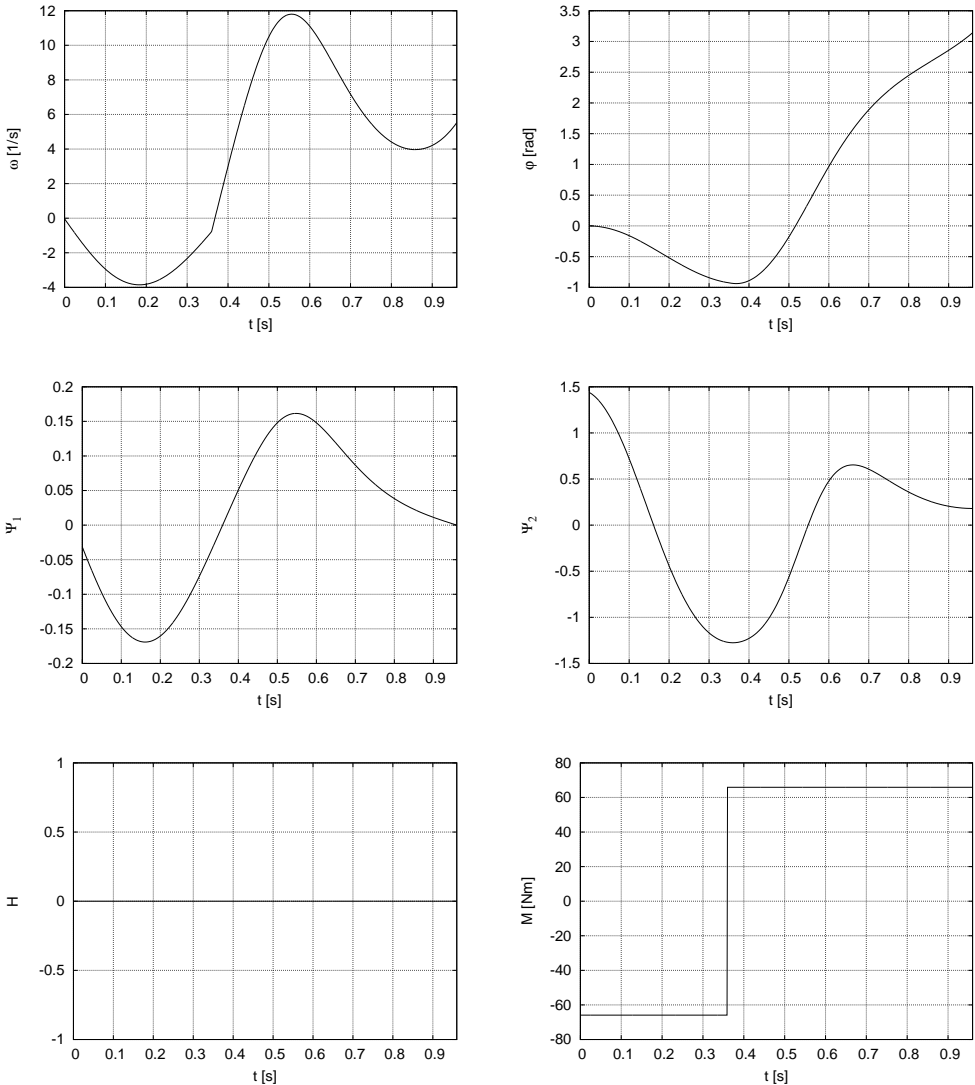

FIG. 4. Graphical presentation of solutions for the set of Eqs. (2.3) and (2.7), for $M_0 = 65.88$ [Nm].

2.2. *Full variant*

Proceeding in a similar fashion as in the previous chapter, we determine the Hamilton's function, which after rearrangement of Eqs. (2.2) to a standard form (2.15)

(2.15)

$$
\frac{dv}{dt} = \frac{(J_w + me^2)(me\omega^2 \sin(\varphi) - kx - bv - Mg - mg)}{\Delta}
$$
$$
- \frac{me \cos(\varphi)(Mel - mge \cos(\varphi))}{\Delta},
$$

$$
\frac{d\omega}{dt} = \frac{-me \cos(\varphi)(me\omega^2 \sin(\varphi) - kx - bv - Mg - mg)}{\Delta}
$$
$$
+ \frac{(M + m)(Mel - mge \cos(\varphi))}{\Delta},
$$

$$
\frac{dx}{dt} = v,
$$

$$
\frac{d\varphi}{dt} = \omega,
$$

$$
\Delta = (M + m)(J_w + me^2) - (me \cos(\varphi))^2
$$

assumes the following form:

(2.16)
$$
H = \Psi_1 \frac{dv}{dt} + \Psi_2 \frac{d\omega}{dt} + \Psi_3 \frac{dx}{dt} + \Psi_4 \frac{d\varphi}{dt} - 1 \; .
$$

On the basis of Eq. (2.16) and criterion (2.1) we determine the formulae for derivatives of coupled functions (2.17):

(2.17)

$$
\frac{d\Psi_1}{dt} = \frac{(J_w + me^2)b\Psi_1 - me \cos(\varphi)b\Psi_2}{\Delta} - \Psi_3,
$$

$$
\frac{d\Psi_2}{dt} = \frac{-2(J_w + me^2)me\omega \sin(\varphi)\Psi_1 + 2m^2e^2 \cos(\varphi)\omega \sin(\varphi)\Psi_2}{\Delta} - \Psi_4,
$$

$$
\frac{d\Psi_3}{dt} = \frac{(J_w + me^2)k\Psi_1 - me \cos(\varphi)k\Psi_2}{\Delta},
$$

$$\text{(2.17)} \quad \frac{d\Psi_4}{dt} = -\Big[(J_w + me^2)me\omega^2 \cos(\varphi) + me\sin(\varphi)(Mel - mge\cos(\varphi))$$

$$- m^2 e^2 g \cos(\varphi)\sin(\varphi)\Big]\frac{\Psi_1}{\Delta}$$

$$+ 2\Big[(J_w + me^2)(me\omega^2 \sin\varphi - kx - bv - Mg - mg)$$

$$- me\cos\varphi(Mel - mge\cos\varphi)\Big]\frac{\Psi_1 m^2 e^2 \cos\varphi \sin\varphi}{\Delta^2}$$

$$- \Big[me\sin\varphi(me\omega^2 \sin\varphi - k - bv - Mg - mg) - m^2 e^2 (\cos\varphi)^2 \omega^2$$

$$+ (m+M)mge\sin\varphi\Big]\frac{\Psi_2}{\Delta}$$

$$+ \Big[(m+M)(Mel - mge\cos\varphi) - me\cos\varphi(me\omega^2 \sin\varphi - kx - bv$$

$$- Mg - mg)\Big]\frac{\Psi_2 m^2 e^2 \cos\varphi \sin\varphi}{\Delta^2}.$$

Then – on the grounds of extremalising the conditions of the Hamilton's function versus moment $M(t)_{el}$ – we formulate the Law of Control in the form (2.18):

$$\text{(2.18)} \qquad M_{el} = M_0 \mathrm{sgn}\left[\frac{(M+m)\Psi_2 - me\cos\varphi\Psi_1}{\Delta}\right],$$

where M_0 – given value of the moment of force.

Using the transversality conditions (2.8) for coupled functions, Hamiltonian zeroing along the optimal trajectory as well as the start conditions for the motion coordinates of the system, we are able to determine the set of start-end conditions (2.19), which allow to solve the system (2.15) and (2.17) in an explicit way.

$$v(0) = 0, \qquad x(0) = -\frac{(M+m)g}{k}, \qquad H(t_k^*) = 0,$$

$$\omega(0) = 0, \qquad \varphi(0) = -\frac{\pi}{2},$$

$$\text{(2.19)}$$

$$\varphi(t_k^*) = +\frac{\pi}{2}, \qquad \Psi_1(t_k^*) = 0,$$

$$\Psi_2(t_k^*) = 0, \qquad \Psi_3(t_k^*) = 0.$$

The problem has been solved numerically for $M_0 = 65.88$ [Nm], using the set of parameters given in Table 1. The results are presented in Fig. 5.

Table 1.

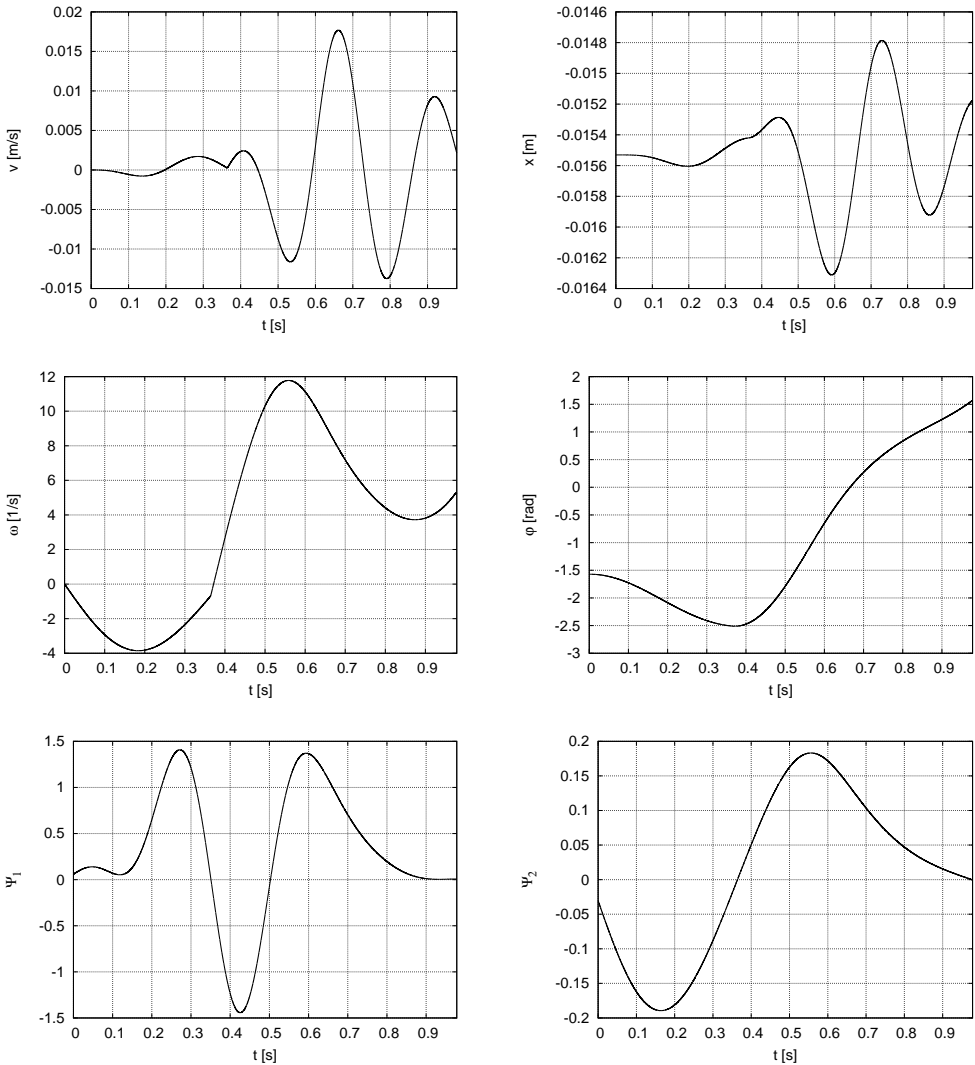|	
Vibrator mass	382.3 [kg]
Radius of vibrator unbalance	0.04 [m]
Moment of inertia reduced to the axis of rotation	1.3 [kgm^2]
Machine body mass	7263.2 [kg]
Coefficient of elasticity of the machine body support	4.83·10^6 [N/m]
Viscous damping coefficient of the machine body support	3.84·10^4 [Ns/m]

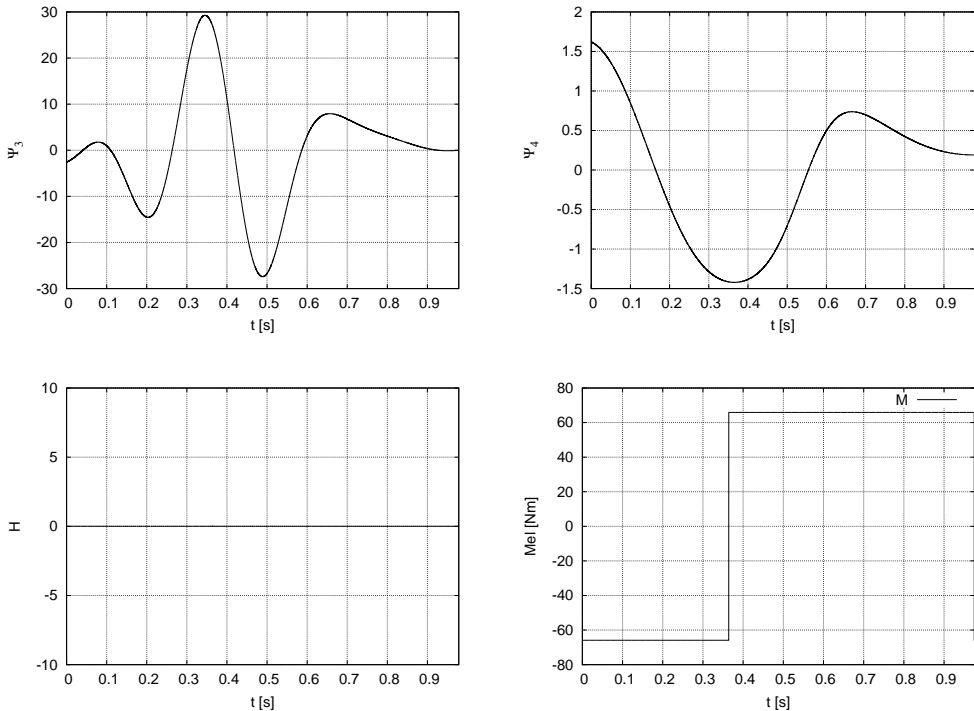FIG. 5. The solutions of systems Eqs. (2.15) and (2.17).

FIG. 6. The solutions of systems Eqs. (2.15) and (2.17) – continuation.

3. INFLUENCE OF VARIABILITY OF THE ELECTRIC DRIVING MOTOR MOMENT ON THE OPTIMAL SOLUTIONS

The most popular source of the moment of force in vibrating machine drives is – in practice – an asynchronous motor. The instantaneous form of the moment of this motor – in the velocity range being near zero – is far from constant and exhibits very strong oscillations with the power network frequency. However, its mean value is – in this velocity range – near the value of the starting moment determined on the basis of the mechanical characteristic of the motor. Assuming this value as M_0 in the previously given models, the comparing simulations can be performed. They will allow estimate the influence of the electromagnetic moment variability on the optimal solutions determined for models with bi-stable moments. The interdependence of the electromagnetic moment of the driving motor and the vibrator shaft was determined in simulations based on the grounds of the asynchronous machine equations obtained as the result of two transformations applied separately for the stator circuit and for the rotor circuit. The first transformation, the Park's one described by the transformation matrix $[T]$ (3.1), changes the phase system of stator circuit equations into

quasi-coordinates $0, d, q$. The second transformation, the Clark's transformation (3.2), transforms the phase system of rotor circuit equations to the coordinates $0, \alpha, \beta$.

$$
(3.1) \qquad [T] = \sqrt{\frac{2}{3}} \begin{bmatrix} \dfrac{1}{\sqrt{2}} & \dfrac{1}{\sqrt{2}} & \dfrac{1}{\sqrt{2}} \\[2mm] \cos\left(p_b\varphi\right) & \cos\left(p_b\varphi - \dfrac{2}{3}\pi\right) & \cos\left(p_b\varphi - \dfrac{4}{3}\pi\right) \\[2mm] -\sin\left(p_b\varphi\right) & -\sin\left(p_b\varphi - \dfrac{2}{3}\pi\right) & -\sin\left(p_b\varphi - \dfrac{4}{3}\pi\right) \end{bmatrix},
$$

$$
(3.2) \qquad [C] = \sqrt{\frac{2}{3}} \begin{bmatrix} \dfrac{1}{\sqrt{2}} & \dfrac{1}{\sqrt{2}} & \dfrac{1}{\sqrt{2}} \\[2mm] 1 & -\dfrac{1}{2} & -\dfrac{1}{2} \\[2mm] 0 & \dfrac{\sqrt{3}}{2} & -\dfrac{\sqrt{3}}{2} \end{bmatrix}.
$$

The relations between currents and quasi-currents $i'_{\alpha r}\ i'_{\beta r}\ i_{ds}\ i_{dq}$ and the transformed power voltages $u_{ds},\ u_{qs}$ can be presented in the following matrix notation:

$$
(3.3) \qquad
\begin{bmatrix} u_{ds} \\ u_{qs} \\ 0 \\ 0 \end{bmatrix} =
\begin{bmatrix} L_{\sigma s} + L_m & 0 & L_m & 0 \\ 0 & L_{\sigma s} + L_m & 0 & L_m \\ L_m & 0 & L'_{\sigma r} + L_m & 0 \\ 0 & L_m & 0 & L'_{\sigma r} + L_m \end{bmatrix} \frac{d}{dt} \begin{bmatrix} i_{ds} \\ i_{qs} \\ i'_{\alpha r} \\ i'_{\beta r} \end{bmatrix} +
$$

$$
+ p_b\dot\varphi \begin{bmatrix} 0 & -(L_{\sigma s} + L_m) & 0 & -L_m \\ L_{\sigma s} + L_m & 0 & L_m & 0 \\ 0 & 0 & 0 & 0 \\ 0 & 0 & 0 & 0 \end{bmatrix} \begin{bmatrix} i_{ds} \\ i_{qs} \\ i'_{\alpha r} \\ i'_{\beta r} \end{bmatrix} +
$$

$$
+ \begin{bmatrix} R_s & 0 & 0 & 0 \\ 0 & R_s & 0 & 0 \\ 0 & 0 & R'_r & 0 \\ 0 & 0 & 0 & R'_r \end{bmatrix} \begin{bmatrix} i_{ds} \\ i_{qs} \\ i'_{\alpha r} \\ i'_{\beta r} \end{bmatrix},
$$

while the electric moment is formulated as:

$$
(3.4) \qquad M_{el} = p_b\left(\Psi_{ds} i_{qs} - \Psi_{qs} i_{ds}\right),
$$

where Ψ_{ds}, Ψ_{qs} – components of the electromagnetic flow associated with the stator and rotor, which can be presented in the matrix notation (3.5):

$$
(3.5) \quad
\begin{bmatrix}
\Psi_{ds} \\
\Psi_{qs} \\
\Psi_{\alpha r} \\
\Psi_{\beta r}
\end{bmatrix}
=
\begin{bmatrix}
L_{\sigma s} + L_m & 0 & L_m & 0 \\
0 & L_{\sigma s} + L_m & 0 & L_m \\
L_m & 0 & L'_{\sigma r} + L_m & 0 \\
0 & L_m & 0 & L'_{\sigma r} + L_m
\end{bmatrix}
\begin{bmatrix}
i_{ds} \\
i_{qs} \\
i'_{\alpha r} \\
i'_{\beta r}
\end{bmatrix}.
$$

The commutation process related to switching-over the phase sequence of the stator circuit, being done in order to change the sense of the moment to the opposite one, was determined on the basis of the Continuity Principle of the electromagnetic flow associated with the rotor circuit. Taking into account Eq. (3.5) – the components of the relevant currents – we can state that: $\Psi_{\alpha r}^- = \Psi_{\alpha r}^+$ and $\Psi_{\beta r}^- = \Psi_{\beta r}^+$, where indices „+" and „−" mark the time just before and just after the switch-over, respectively.

The continuity of the flow associated with the rotor leads to the formulae for the current components values just after the switch-over, in the form:

$$
(3.6) \quad
\begin{aligned}
i_{ds}^+ &= 0, \\
i_{qs}^+ &= 0, \\
i'^+_{\alpha r} &= \frac{L_m i_{ds}^- + (L'_{\sigma r} + L_m) i'^-_{\alpha r}}{L'_{\sigma r} + L_m}, \\
i'^+_{\beta r} &= \frac{L_m i_{qs}^- + (L'_{\sigma r} + L_m) i'^-_{\beta r}}{L'_{\sigma r} + L_m}.
\end{aligned}
$$

Table 2. Parameters of the asynchronous motor.

Motor power rating P_n	8.1 [kW]
Motor rated velocity n_n	1420 [rot/min]
Stator leakage inductance $L_{\sigma s}$	4.77 [mH]
Rotor leakage inductance in stator terms $L'_{\sigma w}$	4.77 [mH]
Magnetic induction L_μ	82.4 [mH]
Stator resistance R_s	0.62 [Ω]
Rotor resistance in stator terms R'_w	0.84 [Ω]

The simulation results presented in Fig. 7 indicate that the switch-over performed at the times determined for models presented in Secs. 2.1 and 2.2, does not cause any significant differences, neither in the curve of the angular coordinate nor in the curve of the angular velocity mean value – regardless of the visible oscillatory influence on the driving moment.
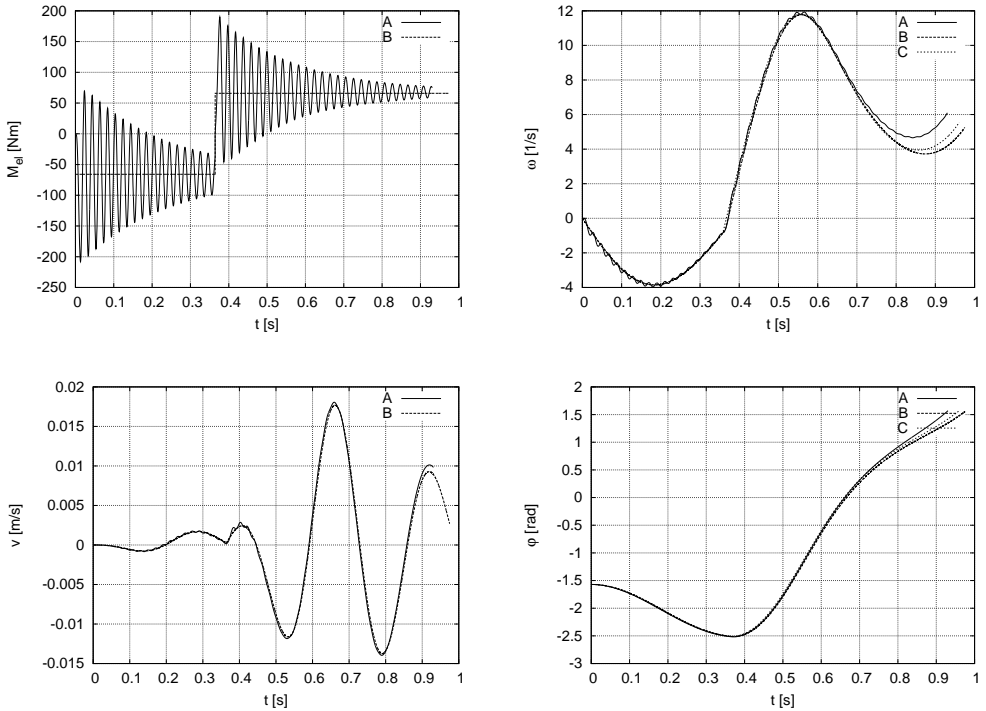
FIG. 7. Graphs of the motion coordinates for: A – model with an electric moment originated from an asynchronous motor, B – full variant with a bi-stable moment of force, C – simplified variant with a bi-stable moment of force.

4. NUMBER OF SWITCH-OVERS OF THE DRIVING MOMENT

The need to determine the number of the moment switch-overs realizing the first half-turn of the vibrator for the given M_0 value, might be essential in the preliminary designing process. For the simplified model this problem can be solved analytically, without the necessity of performing an explicit solution of the pendulum equation of motion. Thus, on the basis of the condition of the mass lifting – in the gravitational field of force [8] – subjected to the influence of the constant value M_0 moment, for the case in which only one switch-over occurs, we are entitled to state the following:

1. During lifting of the vibrator mass centre, the motion will take place until the work performed by the moment of force equals the potential energy stored in the vibrator. Denoting by φ_1 the angular distance at which this equalisation occurs, we obtain the formula:

(4.1) $$M_0\varphi_1 = mge(1 - \cos\varphi_1).$$

2. During the reverse in the intermediate point, related to the lowest position of the vibrator mass centre, the vibrator kinetic energy constitutes the sum of the recovered potential energy connected with the height determined by angle φ_1 and the work performed at returning at the angular distance φ_1. This energy – increased by the work performed on the further part of the distance φ and decreased by the potential energy of the repeated lifting of the mass centre - should retain its positive value to avoid the stopping of motion and changing its direction. Thus, we can write:

(4.2) $E = mge(1 - \cos\varphi_1) + M_0\varphi_1 + M_0\varphi - mge(1 - \cos\varphi) > 0.$

3. To quarantee the fulfilment of inequality (4.2), which after rearrangement assumes the form:

(4.3) $$\frac{M_0}{mge}(2\varphi_1 + \varphi) > 1 - \cos\varphi,$$

the care should be taken that the straight line of the left-hand side of the inequality should be above the function value of the right-hand side. The smallest M_0 value corresponds to the situation when tangents to the function on its both sides are equal at certain critical point φ_{kr} and the function values are also equal at this point. Thus, respectively:

(4.4) $$\frac{M_{0\,\min}}{mge} = \sin\varphi_{kr},$$

(4.5) $$\frac{M_{0\,\min}}{mge}(2\varphi_1 + \varphi_{kr}) = 1 - \cos\varphi_{kr}.$$

4. Solution of the set of Eqs. (4.1), (4.4), (4.5):

$$M_{0\,\min} = 0.422mge,$$

(4.6) $$\varphi_1 = 0.905 \text{ [rad]},$$

$$\varphi_{kr} = 2.706 \text{ [rad]}$$

determines the smallest value of the driving moment $M_{0\,\min}$, which allows to perform the first half-turn with only one switch-over of the moment. It also determines two angles: φ_1 and φ_{kr}, for which the angular velocity of the vibrator equals zero.

By means of a similar reasoning we can determine the switch-over times and the minimum moment M_0 for a larger number of switch-overs. Table 3 presents the determined dependences, with notations: n – number of switch-overs, $k = \dfrac{M_{0\,\min}}{mge}$, φ_i – successive angles corresponding to switch-overs of the moment, φ_{kr} – critical value of the angle of rotation.

Table 3.

n	k	φ_i [rad]	φ_{kr} [rad]
0	0.724	$-$	$+2.31$
1	0.422	-0.905	$+2.706$
2	0.293	$+0.605, -1.306$	$+2.844$
3	0.224	$-0.456, +0.948, -1.546$	$+2.916$

Knowing the switch-over number of the moment, it is possible to estimate the least upper bound of the time needed for performing the first half-turn. Fig. 8 presents the nomogram, obtained by solving the pendulum equation of
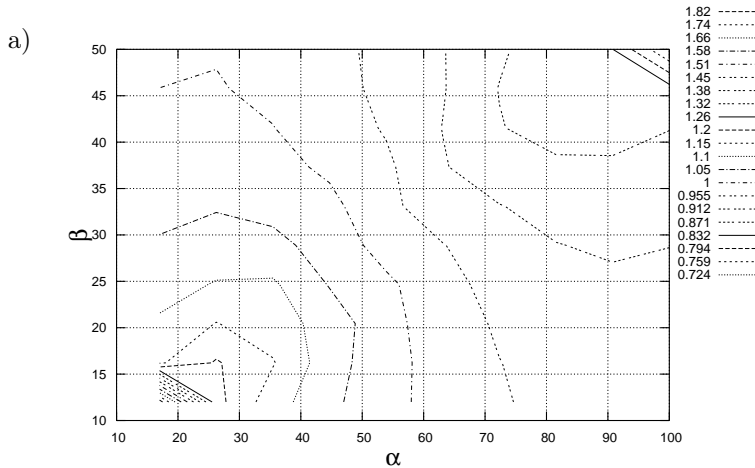
alpha	beta	t [s]
...	...	...
75.650	34.000	0.924
75.700	33.000	0.993
75.700	33.050	0.988
75.700	33.100	0.983
75.700	33.150	0.979
75.700	33.200	0.975
*75.700	33.250	0.971
75.700	33.300	0.967
75.700	33.350	0.963
...	...	...

FIG. 8. Time of the first half-turn as a function of α and β parameters for the case of one switch-over of the moment. a) Nomogram, b) Table of data (* – indicates data for the example discussed in the paper).

motion, relating the time – which is looked for – to two parameters $\alpha = \dfrac{mge}{J_{zr}}$ and $\beta = \dfrac{M_0}{J_{zr}}$ for the case of one switch-over of the moment.

5. CONCLUSIONS

Summarising the problem of the first half-turn, we can state that:

1. It is possible to find the driving moment of the variable sense, which will allow the first half-turn to be performed by vibrators, without unnecessery overmotoring.

   (a) The driving moment is contained within the boundary of this moment variability, and due to this feature – for the values being in the range $[-M_0, +M_0]$ – it becomes the bi-stable moment of the value $\pm M_0$.

   (b) Times of the switch-over of the driving moment can be estimated on the basis of Eq. (2.18) and dependences (2.15), (2.17), (2.19) necessary for solving the Hamiltonian extreme (2.16).

2. The start, in which the first half-turn is put into practice by switch-overs of the sense of the moment, allows to decrease radically the starting moment of the motor, which corresponds to decreasing the driving unit power. As a result, the system efficiency at the nominal operations improves significantly.

3. Simplifications – following from the assumption that the driving moment is of a constant value and from the omission of body and vibrator interactions – do not introduce any essential errors, concerning the determination of the switch-over time of the moment of force, for typical driving systems of vibratory machines. It means for such systems, in which an asynchronous motor is the source of the moment of force and the vibrator is fixed to the elastically supported machine body. The value of the motor starting moment found directly from the catalogue data or determined on the basis of the Kloss mechanical characteristics – with taking into consideration the displacement of current for deep-groove motors (like in B NEMA [National Electrical Manufacturers Association] design) and for multi-cage motors (like in C NEMA design) – should be applied in calculations as the M_0 value.

4. When determining the M_0 value for over-resonance machines, special attention should be directed towards the situation when the vibrator is passing through the resonance zone. When the selected value of the moment (although allowing to perform the first half-turn and to overcome the motion resistance at nominal operations) is too low, it might be not sufficient to

overcome the increased resistance during passing through the resonance zone. In consequence, the stall of a motor in this zone occurs.

5. If the start is realised at low values of the M_0 moment, which prolongs the time when the motor stays in the zone of short-circuit currents, the problem of motor thermal load and the selection of safety measures should be considered. For estimation of the lowest upper bound of the time of the first half-turn and for determination of the minimum number of switch-overs of the moment, one can use dependences presented in Sec. 4.

References

1. M. ATHANS, P. FALB, *Optimal Control. An Introduction to the Theory and Its Applications*, WNT, Warsaw 1966.

2. T. BANASZEWSKI, *Screens*, Publ. Śląsk, 1990.

3. I. GELFAND, S. FOMIN, *Calculus of Variations*, PWN, Warsaw 1975.

4. H. GÓRECKI, *Optimization of Dynamical Systems*, PWN, Warsaw 1993.

5. J. ŁAWRYNOWICZ, *Calculus of Variations with an Introduction to the Mathematical Programming*, WNT, Warsaw 1977.

6. *Numerical Recipes in C. The Art of Scientific Computing*, Cambridge University Press, New York 1992.

7. A. JAGIEŁŁO, *Non-Holonomic Transformations in the Electric Machines Theory*, PWN, Warsaw 2002.

8. J. MICHALCZYK, *Vibratory Machines. Dynamical Calculations, Vibrations, Noise*, WNT, Warsaw 1995.

9. W. PASZEK, *Transient States of Alternating Current Electric Machines*, WNT, Warsaw 1986.

RESISTANCE OF RC ANNULAR CROSS-SECTIONS WITH OPENINGS SUBJECTED TO AXIAL FORCE AND BENDING

M. L e c h m a n

Building Research Institute

ul. Filtrowa 1, 00-611 Warszawa, Poland

This paper presents ultimate limit state analysis of the resistance of reinforced concrete (RC) annular cross-sections with openings, subjected to the axial force and the bending moment. Based on nonlinear material laws for concrete and reinforcing steel and using the method of mathematical induction, analytical formulae are derived in the case when the cross-section is weakened by an arbitrary number of openings located symmetrically with respect to the bending direction. In this approach, the additional reinforcement at openings is also taken into account. The results of numerical calculations are presented in the form of interaction diagrams with the design values of the normalized cross-sectional forces n_u and m_u for the sections weakened by openings as well as for the closed ones. This approach has been applied to investigate the influence of different parameters such as the size and the number of openings, the reinforcement ratio, the additional reinforcement at the opening, the form of stress-strain relationships for concrete and the thickness/radius ratio, on the section resistance.

NOTATIONS

E_s — modulus of elasticity of steel,

F_{ad1} — area of the additional reinforcement at the opening specified by α_1,

F_{ad2} — area of the additional reinforcement at the opening specified by α_2,

M_{Sd} — design bending moment,

M_u — ultimate bending moment,

N_{Sd} — design axial force,

N_u — ultimate axial force,

R — outer radius of ring,

c_{cs} — coefficient of concrete softening,

c_{sh} — coefficient of steel hardening,

f_{ck} — characteristic strength of concrete in compression,

f_{yk} — yield stress of steel,

$m_{Rd} = m_u$ — design normalized ultimate bending moment,

$n_{Rd} = n_u$ — design normalized ultimate axial force,

r — inner radius of the ring,

r_m — mean radius of the ring,

r_s — radius of the circumference on which reinforcing steel is located,

$t = R - r$ — thickness of the cross-section,

α angle describing the location of the neutral axis ($\alpha_1 \le \alpha \le \alpha_2$), rad,

α_1 angle describing the location of the first opening, rad,

α_2 angle describing the location of the second opening, rad,

m number of openings,

$(\alpha_1, \alpha_2), (\alpha_3, \alpha_4), ..., (\alpha_{m-1}, \alpha_m)$ couples of angular coordinates determining the locations of openings, rad,

α_b angle determining the depth of the zone of plastified concrete, rad,

α_{a1} angle determining the depth of the zone of plastified steel in compression, rad,

α_{a2} angle determining the depth of the zone of plastified steel in tension, rad,

ε strain expressed in ‰,

ε_c strain in concrete, [‰],

ε_{cu} ultimate strain in concrete, [‰],

ε_s strain in steel, [‰],

ε_{su} ultimate strain in steel, [‰],

ε_{sy} strain related to the yield stress of steel, [‰],

ε_0 the given numerical parameter,

γ_c partial safety factor for concrete,

γ_s partial safety factor for steel,

μ the ratio of cross-sectional areas, steel to concrete,

$\mu_{\alpha1}, \mu_{\alpha2}$ the ratios of cross-sectional areas, additional reinforcement located at the openings specified by α_1, α_2 to concrete,

$\mu_{\alpha i}$ the ratio of cross-sectional areas, additional reinforcement located at the opening side specified by α_i to concrete,

σ_c compressive stress in concrete,

σ_s stress in steel.

1. INTRODUCTION

Structures and members with the annular cross-section weakened by openings subjected to the axial force and bending moment are frequently encountered in engineering practice (towers, chimneys, lamp posts, columns etc.).

Determination of the resistance of the cross-sections of RC chimneys and tower structures has been reported in the literature by several authors. The ultimate load analysis of a shell with a circular cross-section weakened by one and two openings is presented in the monograph by PINFOLD [1]. A similar approach is also used by NIESER and ENGEL [2], in DIN 1056 and CICIND codes [3, 4], assuming the central layout of steel reinforcement in the wall of tower or chimney structures and ignoring the effect of additional reinforcement at the sides of openings. The generalized linear section model for analysis of RC chimneys weakened by openings was proposed by LECHMAN and LEWIŃSKI [5].

When RC cross-sections under consideration are subjected to the given design axial force N_{Sd} and bending moment M_{Sd} and a nonlinear behavior of concrete and steel reinforcement is assumed, the problem is described mathematically by a set of equations which are nonlinear and difficult to solve. Therefore, a numerical strategy must be used. For this purpose the modified BFGS method has been successfully applied by LECHMAN and STACHURSKI [6].

Despite the generality of the papers mentioned, there are no appropriate analytical formulae for determining the resistance of the annular sections weakened by an arbitrary number of openings and taking into consideration the physical nonlinearity of concrete and reinforcing steel. Such a task has been undertaken in the present paper.

2. DERIVATION OF FORMULAE FOR THE SECTION WITH ONE OR TWO DIAMETRICALLY OPPOSITE OPENINGS

As the first step of the proposed approach, the annular cross-section, described by the outer radius – R and the inner radius – r, is assumed to be weakened by one or two openings. The locations of the openings are determined by couples of the angular coordinates $(0, \alpha_1)$, (α_2, π), $0 \leq \alpha_1 \leq \alpha_2 \leq \pi$. The reinforcing steel spaced in a general case continuously at l layers can be replaced by a continuous ring of equivalent area located on the reference circumference of radius r_s (Fig. 1a). The section under consideration is subjected to the axial force N_u and the bending moment M_u at ultimate limit state. If $\alpha_1 \neq 0$ and $\alpha_2 = \pi$, it forms the cross-section weakened by a single opening, while $\alpha_1 = 0$ and $\alpha_2 = \pi$ describe the closed annular one.

In the present derivation, the following assumptions have been introduced:

   (i) plane cross-sections remain plane,
  (ii) the tensile strength of concrete is ignored,
 (iii) the reinforcement in both the tension and compression zone is taken into account,
 (iv) the thickness of the section is thin compared with its diameter,
  (v) elasto-plastic stress/strain relationships for concrete and steel are used,
 (vi) the ultimate strain for concrete is defined as $-3.5‰$ or $-2‰$, while for reinforcement as $5‰$ (tension) and $-5‰$ (compression).

For determining the resistance of cross-sections, the stress-strain relationships for concrete in compression with softening in the plastic range is given by (Fig. 1b):

$$(2.1) \quad \begin{aligned} \sigma_c &= \frac{f_{ck}}{\gamma_c} \frac{2}{\varepsilon_0} \left(1 + \frac{\varepsilon}{2\varepsilon_0} \right) \varepsilon, & \text{for } -\varepsilon_0 \leq \varepsilon \leq 0, \\ \sigma_c &= -\frac{f_{ck}}{\gamma_c} \left(1 - c_{cs} \frac{\varepsilon + \varepsilon_0}{\varepsilon_{cu} + \varepsilon_0} \right), & \text{for } -3.5 \leq \varepsilon \leq -\varepsilon_0, \end{aligned}$$

where ε_0 – the given numerical parameter, f_{ck} – characteristic strength of concrete in compression, γ_c – partial safety factor for concrete, $c_{cs} = (f_{cd} - f_{cu})/f_{cd}$ – coefficient of concrete softening in the plastic range, f_{cd} – design value of the compressive strength of concrete, $f_{cu} = \sigma_c(\varepsilon_{cu})$.
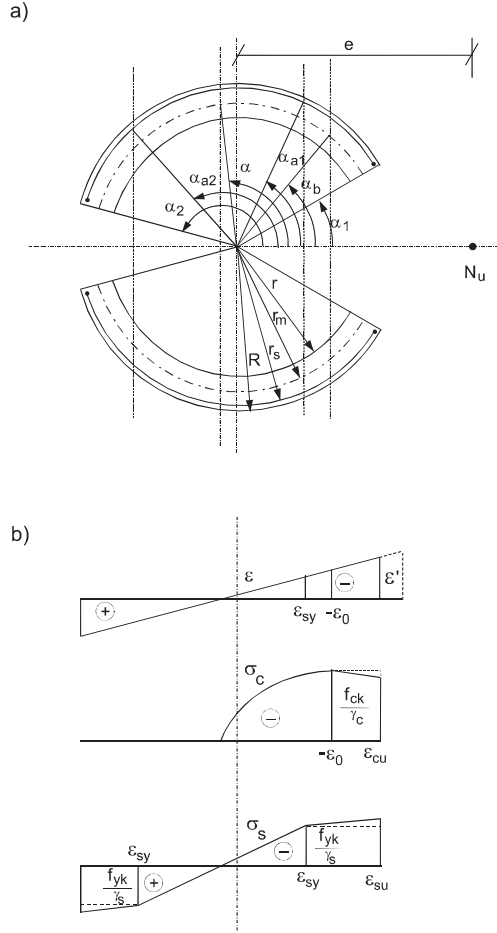
a)

b)

FIG. 1. a) The cross-section weakened by two openings, b) distribution of strains ε, stresses in concrete σ_c and in steel σ_s across the section.

To determine the resistance of the cross-sections, the stress-strain relations for reinforcing steel with hardening in the plastic range are assumed as (Fig. 1b):

$$
\begin{aligned}
\sigma_s &= \frac{f_{yk}}{\varepsilon_{ss}}\varepsilon, & \text{for} \quad -\varepsilon_{sy} \le \varepsilon \le \varepsilon_{sy}, \\[2mm]
\sigma_s &= \frac{f_{yk}}{\gamma_s}\left(1 + c_{sh}\frac{\varepsilon - \varepsilon_{sy}}{\varepsilon_{su} - \varepsilon_{sy}}\right), & \text{for} \quad \varepsilon_{sy} \le \varepsilon \le 10, \\[2mm]
\sigma_s &= -\frac{f_{yk}}{\gamma_s}\left(1 - c_{sh}\frac{\varepsilon + \varepsilon_{sy}}{\varepsilon_{su} - \varepsilon_{sy}}\right), & \text{for} \quad -10 \le \varepsilon \le -\varepsilon_{sy}, \\[2mm]
\varepsilon_{ss} &= \frac{f_{yk}}{E_s}, \qquad \varepsilon_{sy} = \frac{\varepsilon_{ss}}{\gamma_s},
\end{aligned}
$$

(2.2)

where f_{yk} – yield stress of steel, E_s – modulus of elasticity of steel, γ_s – partial safety factor for steel, c_{sh} – coefficient of steel hardening in the plastic range expressed as:

$$c_{sh} = \frac{f_{su} - f_{yd}}{f_{yd}},$$

f_{yd} – design value of the yield stress of steel, $f_{su} = \sigma_s(\varepsilon_{su})$.

Let us consider the cross-section under combined compression and bending. Due to the Bernoulli assumption we obtain:

(2.3)
$$\varepsilon_c = \frac{\cos\varphi - \cos\alpha}{\rho_R - \cos\alpha}\varepsilon' = (\cos\varphi - \cos\alpha)\varepsilon'_\alpha,$$

$$\varepsilon_s = \frac{\rho\cos\varphi - \cos\alpha}{\rho_R - \cos\alpha}\varepsilon' = (\rho\cos\varphi - \cos\alpha)\varepsilon'_\alpha,$$

where ε' – the maximum compressive strain in concrete at the point $(0, R)$, [‰], α – angle describing the location of the neutral axis, rad, φ – angular coordinate, rad, ρ – coefficient, $\rho = r_s/r_m$, ρ_R – coefficient, $\rho_R = R/r_m$, $\varepsilon'_\alpha = \dfrac{\varepsilon'}{\rho_R - \cos\alpha}$.

The conditions of the strain conformity for the concrete and the steel in compression and in tension are expressed, respectively, by

(2.4)
$$(\cos\alpha_b - \cos\alpha)\varepsilon'_\alpha = -\varepsilon_0,$$

(2.5)
$$(\rho\cos\alpha_{a1} - \cos\alpha)\varepsilon'_\alpha = -\varepsilon_{sy},$$

(2.6)
$$(\rho\cos\alpha_{a2} - \cos\alpha)\varepsilon'_\alpha = \varepsilon_{sy},$$

where α_b – angle determining the depth of the zone of the plastified concrete, α_{a1} – angle determining the depth of the zone of the plastified steel in compression, α_{a2} – angle determining the depth of the zone of the plastified steel in tension.

The resistance of the cross-section is reached when either the ultimate strain in concrete ε_{cu} or in steel ε_{su} is reached anywhere in that section, i.e. the following conditions must be satisfied:

(2.7)
$$(\cos\alpha_1 - \cos\alpha)\varepsilon'_\alpha = \varepsilon_{cu},$$

(2.8)
$$(\rho\cos\alpha_2 - \cos\alpha)\varepsilon'_\alpha = \varepsilon_{su}.$$

On the basis of a combinatorial approach, eight possible forms of the stress distribution in the section are to be considered:

1) elastic phase of the concrete and steel,
2) plastic phase of the concrete, elastic phase of the steel,

3) plastic phase of the concrete and the steel in compression, elastic phase of the steel in tension,

4) plastic phase of the concrete and the steel in tension, elastic phase of the steel in compression,

5) elastic phase of the concrete and the steel in compression, plastic phase of the steel in tension,

6) elastic phase of the concrete and the steel in tension, plastic phase of the steel in compression steel,

7) elastic phase of the concrete, plastic phase of the steel in compression and the steel in tension,

8) plastic phase of the concrete and steel.

Let us consider the case 8). The equilibrium equation of the normal forces in the cross-section weakened by one or two openings at ultimate limit state takes the following form:

$$
\begin{aligned}
(2.9) \quad 2 &\left(\int_{\alpha_1}^{\alpha_b} \sigma_c^{pl} dA_c + \int_{\alpha_b}^{\alpha} \sigma_c^{e} dA_c \right) + 2 \left(\int_{\alpha_1}^{\alpha_{a1}} \sigma_s^{pl} dA_s + \int_{\alpha_{a1}}^{\alpha_{a2}} \sigma_s^{e} dA_s \right. \\
&\left. + \int_{\alpha_{a2}}^{\alpha_2} \sigma_s^{pl} dA_s \right) + 2F_{a\alpha1}\sigma_s^{pl}(\alpha_1) + 2F_{a\alpha2}\sigma_s^{pl}(\alpha_2) + N_u = 0,
\end{aligned}
$$

where σ_c^{pl} – the stress function of concrete in the plastic range given by $(2.1)_2$, σ_c^{e} – the stress function of concrete in the elastic range given by $(2.1)_1$, σ_s^{pl} – the stress function of steel in the plastic range given by $(2.2)_2$, $(2.2)_3$, σ_s^{e} – the stress function of steel in the elastic range given by $(2.2)_1$, dA_c – element of the concrete area, dA_s – element of the steel area, $F_{a\alpha1}$ – area of the additional reinforcement at the opening specified by α_1, $F_{a\alpha2}$ – area of the additional reinforcement at the opening specified by α_2.

Using the relation $dA_c + dA_s = dA = r_m t d\varphi$, the equilibrium equation of the sectional bending moments at ultimate limit state with respect to the line perpendicular to the symmetry axis and crossing it at the centre of the section, can be written in the form

$$
\begin{aligned}
(2.10) \quad r_m t(1-\mu) &\left(\int_{\alpha_1}^{\alpha_b} \sigma_c^{pl} r_m \cos\varphi d\varphi + \int_{\alpha_b}^{\alpha} \sigma_c^{e} r_m \cos\varphi d\varphi \right) \\
&+ r_m t \mu \left(\int_{\alpha_1}^{\alpha_{a1}} \sigma_s^{pl} r_s \cos\varphi d\varphi + \int_{\alpha_{a1}}^{\alpha_{a2}} \sigma_s^{e} r_s \cos\varphi d\varphi + \int_{\alpha_{a2}}^{\alpha_2} \sigma_s^{pl} r_s \cos\varphi d\varphi \right) \\
&+ F_{a\alpha1}\sigma_s^{pl}(\alpha_1) r_s \cos\alpha_1 + F_{a\alpha2}\sigma_s^{pl}(\alpha_2) r_s \cos\alpha_2 + M_u = 0.
\end{aligned}
$$

Taking into account the relationships (2.1)–(2.3), after integration and rearrangement of (2.9), (2.10) we obtain

$$(2.11) \qquad \alpha = \text{arc } \cos\left(\frac{\rho_R(\varepsilon_{su}\cos\alpha_1 - \varepsilon_{cu}\cos\alpha_2)}{\varepsilon_{su} - \varepsilon_{cu}}\right),$$

$$(2.12) \qquad \varepsilon' = \varepsilon_{cu}\frac{\rho_R - \cos\alpha}{\rho_R\cos\alpha_1 - \cos\alpha},$$

$$(2.13) \qquad \alpha_b = \begin{cases} \alpha_1 & \text{elastic phase,} \\ \text{arc } \cos\left(\cos\alpha - \varepsilon_0\dfrac{1}{\varepsilon'_\alpha}\right) & \text{plastic phase,} \end{cases}$$

$$(2.14) \qquad \alpha_{a1} = \begin{cases} \alpha_1 & \text{elastic phase,} \\ \text{arc } \cos\left[\dfrac{1}{\rho}\left(\cos\alpha - \varepsilon_{sy}\dfrac{1}{\varepsilon'_\alpha}\right)\right] & \text{plastic phase,} \end{cases}$$

$$(2.15) \qquad \alpha_{a2} = \begin{cases} \alpha_2 & \text{elastic phase,} \\ \text{arc } \cos\left[\dfrac{1}{\rho}\left(\cos\alpha + \varepsilon_{sy}\dfrac{1}{\varepsilon'_\alpha}\right)\right] & \text{plastic phase,} \end{cases}$$

$$(2.16) \quad n_u = -\frac{1}{\pi}\left\{-\frac{1-\mu}{\gamma_c}[X_7(\alpha_b) + \frac{c_{cs}}{\varepsilon_{cu} + \varepsilon_0}[\varepsilon'_\alpha X_4(\alpha,\alpha_b) + \varepsilon_0 X_7(\alpha_b)]\right.$$

$$+ \frac{1-\mu}{\gamma_c}\varepsilon'_\alpha\frac{2}{\varepsilon_0}\left[X_1(\alpha,\alpha_b) + \frac{1}{2\varepsilon_0}\varepsilon'_\alpha X_2(\alpha,\alpha_b)\right] + \mu\frac{f_{yk}}{f_{ck}}\left\{-\frac{1}{\gamma_s}[X_8(\alpha_{a1})\right.$$

$$+ \frac{c_{sh}}{\varepsilon_{su} - \varepsilon_{sy}}[\varepsilon'_\alpha X_5(\alpha,\alpha_{a1}) - \varepsilon_{sy}X_8(\alpha_{a1})] + \frac{1}{\varepsilon_{ss}}\varepsilon'_\alpha X_3(\alpha,\alpha_{a1},\alpha_{a2})$$

$$+ \left\{\frac{1}{\gamma_s}[X_9(\alpha_{a2}) + \frac{c_{sh}}{\varepsilon_{su} - \varepsilon_{sy}}[\varepsilon'_\alpha X_6(\alpha,\alpha_{a2}) - \varepsilon_{sy}X_9(\alpha_{a2})]\right\}$$

$$+ \frac{f_{yk}}{f_{ck}}\mu_{\alpha1}\left\{-\delta_{k1}\frac{1}{\gamma_s}\left[1 - \frac{c_{sh}}{\varepsilon_{su} - \varepsilon_{sy}}[\varepsilon'_\alpha(\rho\cos\alpha_1 - \cos\alpha) + \varepsilon_{sy}]\right]\right.$$

$$\left. + \delta_{k1+1}\frac{\varepsilon'_\alpha}{\varepsilon_{ss}}(\rho\cos\alpha_1 - \cos\alpha)\right\}$$

$$+ \frac{f_{yk}}{f_{ck}}\mu_{\alpha2}\left\{\delta_{k2}\frac{1}{\gamma_s}\left[1 + \frac{c_{sh}}{\varepsilon_{su} - \varepsilon_{sy}}[\varepsilon'_\alpha(\rho\cos\alpha_2 - \cos\alpha) - \varepsilon_{sy}]\right]\right.$$

$$\left.\left.\left. + \delta_{k2+1}\frac{\varepsilon'_\alpha}{\varepsilon_{ss}}(\rho\cos\alpha_2 - \cos\alpha)\right\}\right\}.$$

$$(2.17) \quad m_u = -\frac{1}{\pi}\left\{-0.5\frac{1-\mu}{\gamma_c}\left[Y_7(\alpha_b) + \frac{c_{cs}}{\varepsilon_{cu}+\varepsilon_0}(\varepsilon'_\alpha Y_4(\alpha,\alpha_b) + \varepsilon_0 Y_7(\alpha_b))\right]\right.$$

$$+ 0.5\frac{1-\mu}{\gamma_c}\varepsilon'_\alpha\frac{2}{\varepsilon_0}\left[Y_1(\alpha,\alpha_b) + \frac{1}{2\varepsilon_0}\varepsilon'_\alpha Y_2(\alpha,\alpha_b)\right] + 0.5\mu\frac{f_{yk}}{f_{ck}}\left[-\frac{1}{\gamma_s}\rho\left[Y_8(\alpha_{a1})\right.\right.$$

$$+ \frac{c_{sh}}{\varepsilon_{su}-\varepsilon_{sy}}(\varepsilon'_\alpha Y_5(\alpha,\alpha_{a1}) - \varepsilon_{sy}Y_8(\alpha_b))\Big] + \frac{1}{\varepsilon_{ss}}\varepsilon'_\alpha Y_3(\alpha_{a1},\alpha_{a2})$$

$$+ \frac{1}{\gamma_s}\rho\left[Y_9(\alpha_{a2}) - \sin\alpha_{a2} + \frac{c_{sh}}{\varepsilon_{su}-\varepsilon_{sy}}(\varepsilon'_\alpha Y_6(\alpha,\alpha_{a2}) - \varepsilon_{sy}Y_9(\alpha_{a2}))\right]\Big]$$

$$+ \frac{f_{yk}}{f_{ck}}\rho\mu_{\alpha1}\left\{-\delta_{k1}\frac{1}{\gamma_s}\left[1 - \frac{c_{sh}}{\varepsilon_{su}-\varepsilon_{sy}}[\varepsilon'_\alpha(\rho\cos\alpha_1 - \cos\alpha) + \varepsilon_{sy}]\right]\cos\alpha_1\right.$$

$$\left. + \delta_{k1+1}\frac{\varepsilon'_\alpha}{\varepsilon_{ss}}(\rho\cos\alpha_1 - \cos\alpha)\cos\alpha_1\right\}$$

$$+ \frac{f_{yk}}{f_{ck}}\rho\mu_{\alpha2}\left\{\delta_{k2}\frac{1}{\gamma_s}\left[1 + \frac{c_{sh}}{\varepsilon_{su}-\varepsilon_{sy}}[\varepsilon'_\alpha(\rho\cos\alpha_2 - \cos\alpha) - \varepsilon_{sy}]\right]\cos\alpha_2\right.$$

$$\left.\left. + \delta_{k2+1}\frac{\varepsilon'_\alpha}{\varepsilon_{ss}}(\rho\cos\alpha_2 - \cos\alpha)\cos\alpha_2\right\}\right\},$$

where:

$$(2.18) \qquad n_u = \frac{N_u}{2\pi r_m t f_{ck}}$$

denotes the normalized ultimate normal force,

$$(2.19) \qquad m_u = \frac{M_u}{4\pi r_m^2 t f_{ck}}$$

denotes the normalized ultimate bending moment, $\mu = dA_s/dA$ – the ratio of areas, steel to concrete, $\mu_{\alpha1} = \dfrac{F_{a\alpha1}}{r_m t}$, $\mu_{\alpha2} = \dfrac{F_{a\alpha2}}{r_m t}$ – the ratios of areas, additional reinforcement located at the openings specified by α_1, α_2 to concrete, t - thickness of the cross-section $t = R - r$, $d\varphi$ – element of the angle measured from the axis in the compressive zone.

$$\delta_k = \frac{1}{2}((-1)^k + 1), \qquad k = 1,2,3;$$

$$k1 = 1,2; \qquad\qquad k2 = 2,3.$$

The functions X_1–X_9 and Y_1–Y_9 are defined by the following formulae:

$$X_1(\alpha, \alpha_b) = \sin\alpha - \sin\alpha_b - \cos\alpha(\alpha - \alpha_b),$$

$$X_2(\alpha, \alpha_b) = (0.5 + \cos^2\alpha)(\alpha - \alpha_b) + 0.25(\sin 2\alpha - \sin 2\alpha_b)$$
$$- 2\cos\alpha(\sin\alpha - \sin\alpha_b),$$

$$X_3(\alpha_{a1}, \alpha_{a2}) = \rho(\sin\alpha_{a2} - \sin\alpha_{a1}) - \cos\alpha(\alpha_{a2} - \alpha_{a1}),$$

(2.20)
$$X_4(\alpha, \alpha_b) = \sin\alpha_b - \sin\alpha_1 - \cos\alpha(\alpha_b - \alpha_1),$$

$$X_5(\alpha, \alpha_{a1}) = \rho(\sin\alpha_{a1} - \sin\alpha_1) - \cos\alpha(\alpha_{a1} - \alpha_1),$$

$$X_6(\alpha, \alpha_{a2}) = \rho(\sin\alpha_2 - \sin\alpha_{a2}) - \cos\alpha(\alpha_2 - \alpha_{a2}),$$

$$X_7(\alpha_b) = \alpha_b - \alpha_1,$$

$$X_8(\alpha_{a1}) = \alpha_{a1} - \alpha_1,$$

$$X_9(\alpha_{a2}) = \alpha_2 - \alpha_{a2}.$$

$$Y_1(\alpha, \alpha_b) = 0.5(\alpha - \alpha_b) + 0.25(\sin 2\alpha - \sin 2\alpha_b)$$
$$- \cos\alpha(\sin\alpha - \sin\alpha_b),$$

$$Y_2(\alpha, \alpha_b) = (1 + \cos^2\alpha)(\sin\alpha - \sin\alpha_b) - \frac{1}{3}(\sin^3\alpha - \sin^3\alpha_b)$$
$$- \cos\alpha[\alpha - \alpha_b + 0.5(\sin 2\alpha - \sin 2\alpha_b)],$$

$$Y_3(\alpha_{a1}, \alpha_{a2}) = \rho\{\rho[0.5(\alpha_{a2} - \alpha_{a1}) + 0.25(\sin 2\alpha_{a2} - \sin 2\alpha_{a1})]$$
$$- \cos\alpha(\sin\alpha_{a2} - \sin\alpha_{a1})\},$$

(2.21)
$$Y_4(\alpha, \alpha_b) = 0.5(\alpha_b - \alpha_1) + 0.25(\sin 2\alpha_b - \sin 2\alpha_1)$$
$$- \cos\alpha(\sin\alpha_b - \sin\alpha_1),$$

$$Y_5(\alpha, \alpha_{a1}) = \rho[0.5(\alpha_{a1} - \alpha_1) + 0.25(\sin 2\alpha_{a1} - \sin 2\alpha_1)]$$
$$- \cos\alpha(\sin\alpha_{a1} - \sin\alpha_1),$$

$$Y_6(\alpha, \alpha_{a2}) = \rho[0.5(\alpha_2 - \alpha_{a2}) + 0.25(\sin 2\alpha_2 - \sin 2\alpha_{a2})]$$
$$- \cos\alpha(\sin\alpha_2 - \sin\alpha_{a2}),$$

$$Y_7(\alpha_b) = \sin\alpha_b - \sin\alpha_1,$$

$$Y_8(\alpha_{a1}) = \sin\alpha_{a1} - \sin\alpha_1,$$

$$Y_9(\alpha_{a2}) = \sin\alpha_2 - \sin\alpha_{a2}.$$

In a similar way one can analyze the section wholly being in compression.

3. GENERALIZATION OF THE OBTAINED FORMULAE FOR THE SECTION WITH m OPENINGS

The presented model can be generalized for the cross-section weakened by more than two openings. Let us consider the annular cross-section weakened by m openings situated symmetrically with respect to the bending direction. By this assumption, the locations of the openings are determined by couples of the angular coordinates (α_1, α_2), (α_3, α_4), ..., (α_{m-1}, α_m), $0 \leq \alpha_1 \leq \alpha_2 \leq \ldots \leq \alpha_{m-1}, \leq \alpha_m \leq \pi$ (Fig. 2). Using the principle of mathematical induction one can obtain a solution that takes a similar form as (2.11)–(2.17). It covers all locations of the neutral axis and takes account of possible plastic ranges of concrete and reinforcing steels. The functions X_1–X_9 and Y_1–Y_9 are given in this case by:

$$X_1(\alpha, \alpha_b) = \sum_{l+1}^{k} (-1)^{i-1} \sin \alpha_i - \delta_l \sin \alpha_b + \delta_k \sin \alpha$$

$$- \cos \alpha \left(\sum_{l+1}^{k} (-1)^{i-1} \alpha_i - \delta_l \alpha_b + \delta_k \alpha \right),$$

$$X_2(\alpha, \alpha_b) = (0.5 + \cos^2 \alpha) \left(\sum_{l+1}^{k} (-1)^{i-1} \alpha_i - \delta_l \alpha_b + \delta_k \alpha \right)$$

$$+ 0.25 \left(\sum_{l+1}^{k} (-1)^{i-1} \sin 2\alpha_i + \delta_l \sin 2\alpha_b + \delta_k \sin 2\alpha \right)$$

(3.1)
$$- 2 \cos \alpha \left(\sum_{l+1}^{k} (-1)^{i-1} \sin \alpha_i - \delta_l \sin \alpha_b + \delta_k \sin \alpha \right),$$

$$X_3(\alpha, \alpha_{a1}, \alpha_{a2}) = \rho \left(\sum_{k1+1}^{k2} (-1)^{i-1} \sin \alpha_i - \delta_{k1} \sin \alpha_{a1} + \delta_{k2} \sin \alpha_{a2} \right)$$

$$- \cos \alpha \left(\sum_{k1+1}^{k2} (-1)^{i-1} \alpha_i - \delta_{k1} \alpha_{a1} + \delta_{k2} \alpha_{a2} \right),$$

$$X_4(\alpha, \alpha_b) = \sum_{l=1}^{l} (-1)^{i-1} \sin \alpha_i + \delta_l \sin \alpha_b$$

$$- \cos \alpha \left(\sum_{i=1}^{l} (-1)^{i-1} \alpha_i + \delta_l \alpha_b \right),$$

$$X_5(\alpha, \alpha_{a1}) = \rho \left(\sum_{i=1}^{k1} (-1)^{i-1} \sin \alpha_i + \delta_{k1} \sin \alpha_{a1} \right)$$
$$- \cos \alpha \left(\sum_{i=1}^{k1} (-1)^{i-1} \alpha_i + \delta_{k1} \alpha_{a1} \right),$$

$$X_6(\alpha, \alpha_{a2}) = \rho \left(\sum_{k2+1}^{m} (-1)^{i-1} \sin \alpha_i + \delta_{k2} \sin \alpha_{a2} \right)$$
$$- \cos \alpha \left(\sum_{k2+1}^{m} (-1)^{i-1} \alpha_i + \delta_{k2} \alpha_{a2} \right),$$

$$X_7(\alpha_b) = \sum_{i=1}^{l} (-1)^{i-1} \alpha_i + \delta_l \alpha_b,$$

$$X_8(\alpha_{a1}) = \sum_{i=1}^{k1} (-1)^{i-1} \alpha_i + \delta_{k1} \alpha_{a1},$$

$$X_9(\alpha_{a2}) = \sum_{k2+1}^{m} (-1)^{i-1} \alpha_i - \delta_{k2} \alpha_{a2} + \pi.$$

(3.1)
[cont.]

$$Y_1(\alpha, \alpha_b) = 0.5 \left(\sum_{l+1}^{k} (-1)^{i-1} \alpha_i - \delta_l \alpha_b + \delta_k \alpha \right)$$
$$+ 0.25 \left(\sum_{l+1}^{k} (-1)^{i-1} \sin 2\alpha_i - \delta_l \sin 2\alpha_b + \delta_k \sin 2\alpha \right)$$
$$- \cos \alpha \left(\sum_{l+1}^{k} (-1)^{i-1} \sin \alpha_i - \delta_l \sin \alpha_b + \delta_k \sin \alpha \right),$$

(3.2)
$$Y_2(\alpha, \alpha_b) = (1 + \cos^2 \alpha) \left(\sum_{l+1}^{k} (-1)^{i-1} \sin \alpha_i - \delta_l \sin \alpha_b + \delta_k \sin \alpha \right)$$
$$- \frac{1}{3} \left(\sum_{l+1}^{k} (-1)^{i-1} \sin^3 \alpha_i - \delta_l \sin^3 \alpha_b + \delta_k \sin^3 \alpha \right)$$
$$- \cos \alpha \left[\sum_{l+1}^{k} (-1)^{i-1} \alpha_i - \delta_l \alpha_b + \delta_k \alpha \right.$$
$$\left. + 0.5 \left(\sum_{l+1}^{k} (-1)^{i-1} \sin 2\alpha_i - \delta_l \sin 2\alpha_b + \delta_k \sin 2\alpha \right) \right],$$

$$(3.2)_{\text{[cont.]}} \quad Y_3(\alpha, \alpha_{a1}, \alpha_{a2}) = \rho \left\{ \rho \left[0.5 \left(\sum_{k1+1}^{k2} (-1)^{i-1} \alpha_i - \delta_{k1} \alpha_{a1} + \delta_{k2} \alpha_{a2} \right) \right. \right.$$

$$+ 0.25 \left(\sum_{k1+1}^{k2} (-1)^{i-1} \sin 2\alpha_i - \delta_{k1} \sin 2\alpha_{a1} + \delta_{k2} \sin 2\alpha_{a2} \right) \Bigg]$$

$$\left. - \cos \alpha \left(\sum_{k1+1}^{k2} (-1)^{i-1} \sin \alpha_i - \delta_{k1} \sin \alpha_{a1} + \delta_{k2} \sin \alpha_{a2} \right) \right\},$$

$$Y_4(\alpha, \alpha_b) = 0.5 \left(\sum_{i=1}^{l} (-1)^{i-1} \alpha_i + \delta_l \alpha_b \right)$$

$$+ 0.25 \left(\sum_{i=1}^{l} (-1)^{i-1} \sin 2\alpha_i + \delta_l \sin 2\alpha_b \right)$$

$$- \cos \alpha \left(\sum_{i=1}^{l} (-1)^{i-1} \sin \alpha_i + \delta_l \sin \alpha_b \right),$$

$$Y_5(\alpha, \alpha_{a1}) = \rho \left[0.5 \left(\sum_{i=1}^{k1} (-1)^{i-1} \alpha_i + \delta_{k1} \alpha_{a1} \right) \right.$$

$$+ \left(0.25 \sum_{i=1}^{k1} (-1)^{i-1} \sin 2\alpha_i + \delta_{k1} \sin 2\alpha_{a1} \right) \Bigg]$$

$$- \cos \alpha \left(\sum_{i=1}^{k1} (-1)^{i-1} \sin \alpha_i + \delta_{k1} \sin \alpha_{a1} \right),$$

$$Y_6(\alpha, \alpha_{a2}) = \rho \left[0.5 \left(\sum_{k2+1}^{m} (-1)^{i-1} \alpha_i + \delta_{k2} \alpha_{a2} \right) \right.$$

$$+ 0.25 \left(\sum_{k2+1}^{m} (-1)^{i-1} \sin 2\alpha_i + \delta_{k2} \sin 2\alpha_{a2} \right) \Bigg]$$

$$- \cos \alpha \left(\sum_{k2+1}^{m} (-1)^{i-1} \sin \alpha_i + \delta_{k2} \sin \alpha_{a2} \right),$$

$$Y_7(\alpha_b) = \sum_{i=1}^{l} (-1)^{i-1} \sin \alpha_i + \delta_l \sin \alpha_b,$$

$$Y_8(\alpha_{a1}) = \sum_{i=1}^{k1} (-1)^{i-1} \sin \alpha_i + \delta_{k1} \sin \alpha_{a1},$$

$$Y_9(\alpha_{a2}) = \sum_{k2+1}^{m} (-1)^{i-1} \sin \alpha_i + \delta_{k2} \sin \alpha_{a2}.$$

$k = 0, 1, ..., m$ – the index of the interval satisfying the condition $\alpha \in \langle \alpha_k, \alpha_{k+1} \rangle$, where α is the angle describing the location of the neutral axis of the section, l denotes the index of the interval satisfying the condition $\alpha_b \in \langle \alpha_l, \alpha_{l+1} \rangle$, $l = 0, 1, ..., k$, $k1$ – the index of the interval satisfying the condition $\alpha_{a1} \in \langle \alpha_{k1}, \alpha_{k1+1} \rangle$, $k1 = 0, ..., k$, $k2$ – the index of the interval satisfying the condition $\alpha_{a2} \in \langle \alpha_{k2}, \alpha_{k2+1} \rangle$, $k2 = k + 1, ..., m$.

In the above formulae it is assumed that if $m1 > m2$ then $\sum\limits_{m1}^{m2}() = 0$.
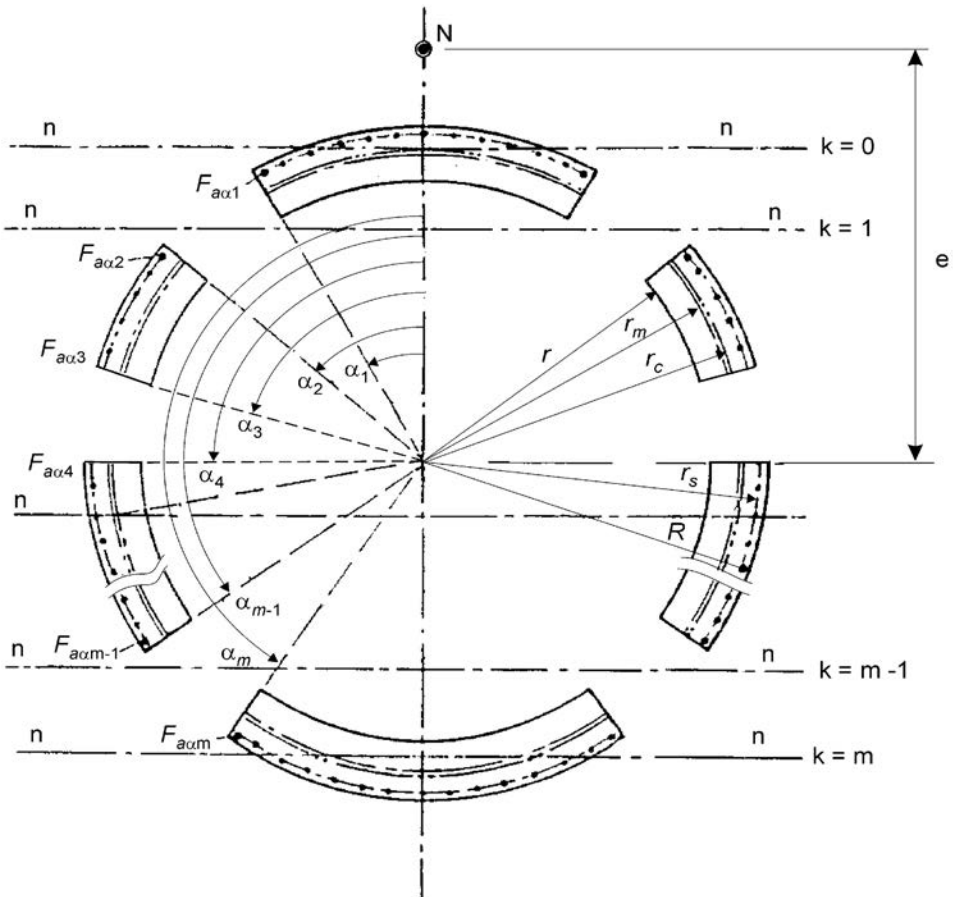

FIG. 2. The cross-section weakened by m openings located symmetrically with respect to the bending direction.

The effects of the additional reinforcements at the openings are determined by the following conditions:

– with respect to n_u:

$$(3.3) \quad \frac{f_{yk}}{f_{ck}} \left\{ -\frac{1}{\gamma_s} \sum_{i=1}^{k1} \mu_{ai} \left[1 - \frac{c_{sh}}{\varepsilon_{su} - \varepsilon_{sy}} [\varepsilon'_\alpha (\rho \cos \alpha_i - \cos \alpha) + \varepsilon_{sy}] \right] + \right.$$

$$+ \frac{\varepsilon'_\alpha}{\varepsilon_{ss}} \sum_{i=k1+1}^{k2} \mu_{ai} (\rho \cos \alpha_i - \cos \alpha)$$

$$\left. + \frac{1}{\gamma_s} \sum_{i=k2+1}^{m} \mu_{ai} \left[1 + \frac{c_{sh}}{\varepsilon_{su} - \varepsilon_{sy}} [\varepsilon'_\alpha (\rho \cos \alpha_i - \cos \alpha) - \varepsilon_{sy}] \right] \right\}$$

– with respect to m_u:

$$(3.4) \quad 0.5 \frac{f_{yk}}{f_{ck}} \rho \left\{ -\frac{1}{\gamma_s} \sum_{i=1}^{k1} \mu_{ai} \left[1 - \frac{c_{sh}}{\varepsilon_{su} - \varepsilon_{sy}} [\varepsilon'_\alpha (\rho \cos \alpha_i - \cos \alpha) + \varepsilon_{sy}] \right] \cos \alpha_i \right.$$

$$+ \frac{\varepsilon'_\alpha}{\varepsilon_{ss}} \sum_{i=k1+1}^{k2} \mu_{ai} (\rho \cos \alpha_i - \cos \alpha) \cos \alpha_i$$

$$\left. + \frac{1}{\gamma_s} \sum_{i=k2+1}^{m} \mu_{ai} \left[1 + \frac{c_{sh}}{\varepsilon_{su} - \varepsilon_{sy}} [\varepsilon'_\alpha (\rho \cos \alpha_i - \cos \alpha) - \varepsilon_{sy}] \right] \cos \alpha_i \right\}.$$

To prove validity of the formulae (3.1)–(3.2) in a general case, the mathematical induction is employed. Substituting $m = 4$, $k = 2$, $l = 2$ in the formulae (3.1) and (3.2), the relationships given by (2.20)–(2.21) for the section weakened by two openings are obtained (Fig. 1a):

$$X_1(\alpha, \alpha_b) = \sum_3^2 (-1)^{i-1} \sin \alpha_i - \delta_2 \sin \alpha_b + \delta_2 \sin \alpha$$

$$- \cos \alpha \left(\sum_3^2 (-1)^{i-1} \alpha_i - \delta_2 \alpha_b + \delta_2 \alpha \right) = -\sin \alpha_b + \sin \alpha - \cos \alpha (-\alpha_b + \alpha),$$

$$Y_1(\alpha, \alpha_b) = 0.5 \left(\sum_3^2 (-1)^{i-1} \alpha_i - \delta_2 \alpha_b + \delta_2 \alpha \right)$$

$$+ 0.25 \left(\sum_3^2 (-1)^{i-1} \sin 2\alpha_i - \delta_2 \sin 2\alpha_b + \delta_2 \sin 2\alpha \right)$$

$$- \cos \alpha \left(\sum_3^2 (-1)^{i-1} \sin \alpha_i - \delta_2 \sin \alpha_b + \delta_2 \sin \alpha \right)$$

$$= 0.5(-\alpha_b + \alpha) + 0.25(-\sin 2\alpha_b + \sin 2\alpha) - \cos \alpha (-\sin \alpha_b + \sin \alpha),$$

due to $\sum_3^2 () = 0$.

In a similar way the functions X_2–X_9 and Y_2–Y_9 given by (2.20) and (2.21) can be obtained.

Let us in turn assume validity of the formulae (3.1)–(3.2) for the section weakened by m openings, $k = 1, 2, ..., m$, and let us consider the section weakened by two additional, symmetrically situated openings, the locations of which are determined by a couple of angular coordinates $(\alpha_{m+1}, \alpha_{m+2})$, $0 \leq \alpha_1 \leq \alpha_2 \leq ... \leq \alpha_m \leq \alpha_{m+1} \leq \alpha_{m+2} \leq \pi$ (Fig. 2).

The task leads to two additional cases of location of the neutral axis α to be considered: $\alpha_{m+1} \leq \alpha \leq \alpha_{m+2}$ or $\alpha_{m+2} \leq \alpha \leq \pi$.

Integrating the equilibrium equation (2.9) in the first case, the function X_1 (α, α_b) takes the following form ($k = m + 1$):

$$X_1(\alpha, \alpha_b) = \sum_{l+1}^{m-1} (-1)^{i-1} \sin \alpha_i - \delta_l \sin \alpha_b + \sin \alpha_{m+1} - \sin \alpha_m$$

$$- \cos \alpha \left(\sum_{l+1}^{m-1} (-1)^{i-1} \alpha_i - \delta_l \alpha_b + \alpha_{m+1} - \alpha_m \right)$$

$$= \sum_{l+1}^{m+1} (-1)^{i-1} \sin \alpha_i - \delta_l \sin \alpha_b - \cos \alpha \left(\sum_{l+1}^{m+1} (-1)^{i-1} \alpha_i - \delta_l \alpha_b \right), \qquad (\delta_{m+1} = 0).$$

For the case $\alpha_{m+2} \leq \alpha \leq \pi$ ($k = m + 1$):

$$X_1(\alpha, \alpha_b) = \sum_{l+1}^{m+1} (-1)^{i-1} \sin \alpha_i - \delta_l \sin \alpha_b + \sin \alpha - \sin \alpha_{m+2}$$

$$- \cos \alpha \left(\sum_{l+1}^{m+1} (-1)^{i-1} \alpha_i - \delta_l \alpha_b + \alpha - \alpha_{m+2} \right)$$

$$= \sum_{l+1}^{m+2} (-1)^{i-1} \sin \alpha_i - \delta_l \sin \alpha_b + \delta_{m+2} \sin \alpha$$

$$- \cos \alpha \left(\sum_{l+1}^{m+2} (-1)^{i-1} \alpha_i - \delta_l \alpha_b + \delta_{m+2} \alpha \right), \qquad (\delta_{m+2} = 1).$$

The remaining functions X_2–X_9 and Y_1–Y_9 can be checked in a similar way. Thus, the general formulae (3.1) and (3.2) are proved.

4. NUMERICAL EXAMPLES

The presented approach enables the determination of the resistance of the sections under consideration. Using the derived formulae (2.11)–(2.17) and

(3.1)–(3.4), the interaction curves with the design values of the normalized, cross-sectional forces n_u and m_u have been obtained for the section weakened by two or four openings (Fig. 3, Fig. 4). Each curve refers to the corresponding value of reinforcement ratio $\mu f_{yk}/f_{ck}$. The maximum compressive strain in concrete is calculated at the extreme fibre in the compression zone of the section. The two numbers $\varepsilon_c/\varepsilon_s$ at each indication point are concrete strain and steel strain in ‰. The points located on the n_u axis are related to pure compression and on the m_u axis – to pure bending. The points denoted by $\varepsilon_c/0$ can be interpreted as transition from the state $\varepsilon_c/(\varepsilon_s < 0)$ described as whole compression (uncracked) to the one $\varepsilon_c/(\varepsilon_s > 0)$ characterized by the occurrence of the tensile strains which cause the crack formation in concrete (cracked).
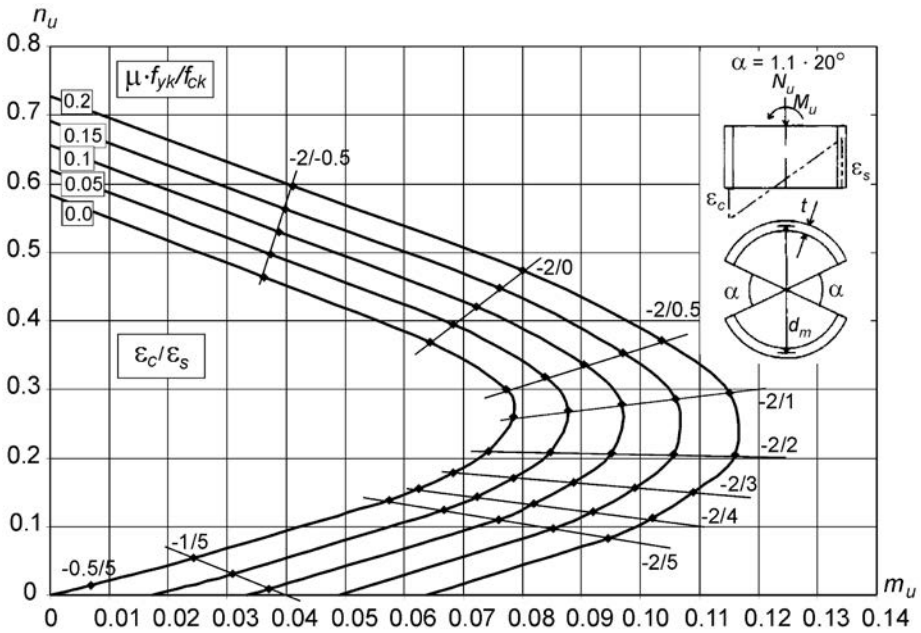

FIG. 3. Interaction diagram with the design values of the normalized cross-sectional forces n_u and m_u for the section weakened by two openings: $f_{yk} = 220$ MPa; $\gamma_c = 1.5$; $\gamma_s = 1.15$, $\varepsilon_0 = 2.0$, $c_{cs} = c_{sh} = 0$.

The effect of the additional lumped reinforcement at an opening was examined under the assumption that the cross-sectional area of the additional steel bars at the sides of the opening is equal to that which would have passed through it. The comparison presented in Fig. 5. indicates that the section resistance determined by the values of n_u, m_u increases due to the additional reinforcement at a single opening by more than 10%, depending on the opening size and the ultimate values ε_{cu} and ε_{su}.
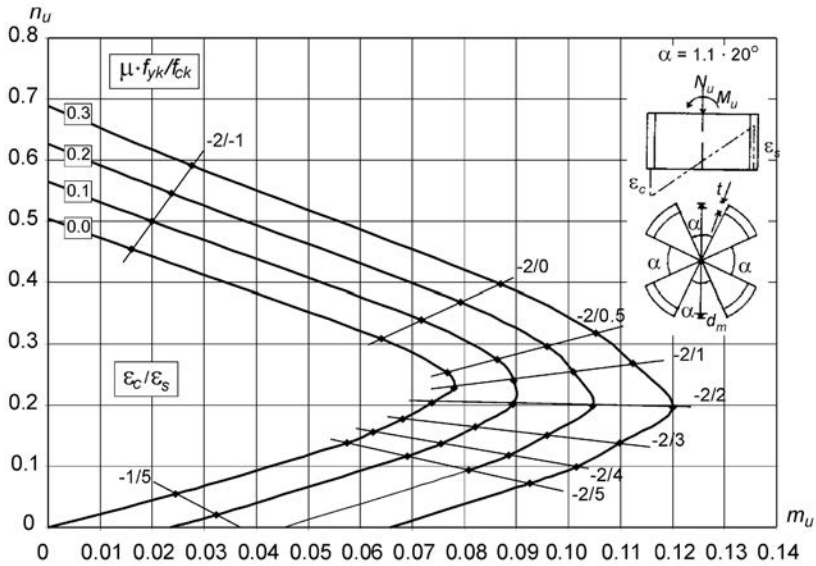
FIG. 4. Interaction diagram with the design values of the normalized cross-sectional forces n_u and m_u for the section weakened by four openings: $f_{yk} = 500$ MPa; $\gamma_c = 1.5$; $\gamma_s = 1.15$, $\varepsilon_0 = 2.0$, $c_{cs} = c_{sh} = 0$.

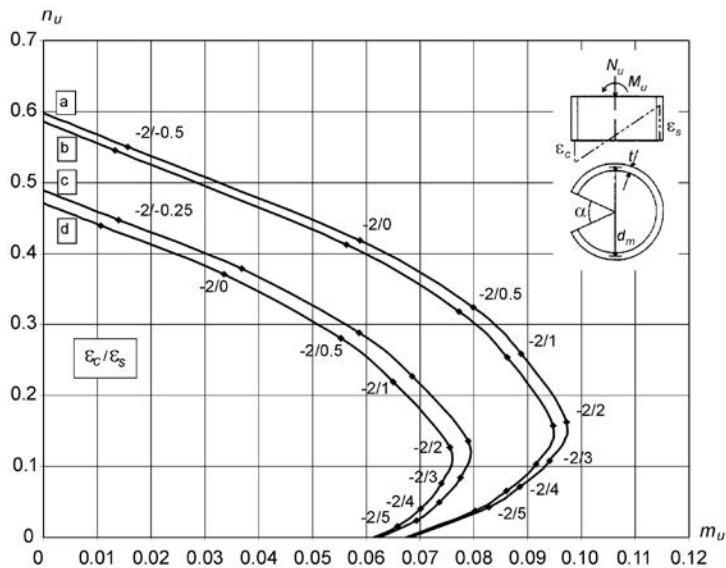FIG. 5. The effect of the additional reinforcement at the opening on the resistance of the section with a single opening: curves a, b – $\alpha = 44°$, $F_{a\alpha 1} = 21.85$ cm^2 (a), $F_{a\alpha 1} = 0$ (b); curves c, d – $\alpha = 66°$, $F_{a\alpha 1} = 32.78$ cm^2 (c), $F_{a\alpha 1} = 0$ (d); $f_{yk} = 410$ MPa; $\gamma_c = 1.5$; $\gamma_s = 1.15$; $\mu = 1\%$, $\varepsilon_0 = 2.0$, $c_{cs} = c_{sh} = 0$.
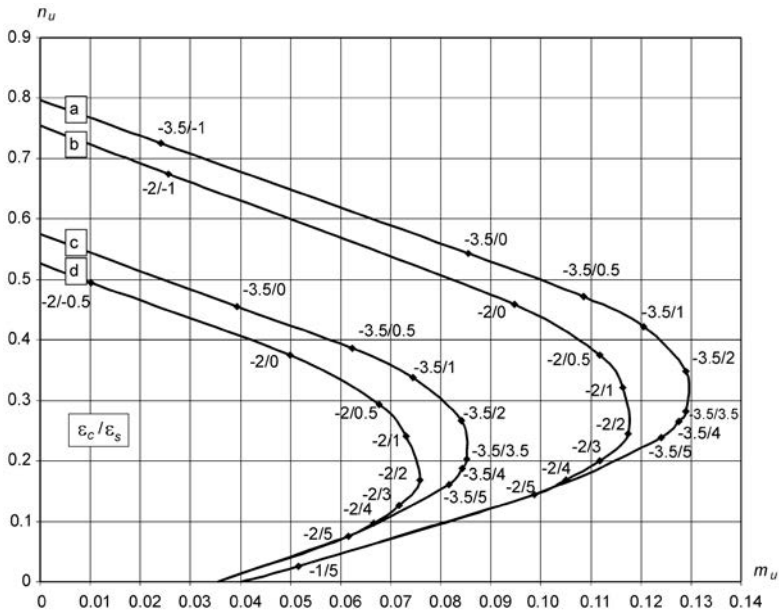
FIG. 6. The effect of a single opening of the size of 44° on the section resistance: curves a, b
– the closed ring section; curves c, d – the ring section weakened by single opening;
$f_{yk} = 410$ MPa; $\gamma_c = 1.5$; $\gamma_s = 1.15$; $\mu = 1\%$, $\varepsilon_0 = 2.0$, $c_{cs} = c_{sh} = 0$.

FIG. 7. Comparison of the section resistance determined by stress-strain relationship for the
concrete given by (2.1) (b) with that based on the parabolic-rectagular one (a);
$f_{yk} = 410$ MPa; $f_{ck} = 20$ MPa; $\gamma_c = 1.5$; $\gamma_s = 1.15$; $\mu = 0.5\%$, $\varepsilon_0 = 2.0$, $c_{cs} = 0.15$, $c_{sh} = 0$.

FIG. 8. Resistance of the annular cross-section as a function of the t/R ratio; $f_{yk} = 410$ MPa; $f_{ck} = 20$ MPa; $\gamma_c = 1.5$; $\gamma_s = 1.15$; $\mu = 0.5\%$, $\varepsilon_0 = 2.0$, $c_{cs} = c_{sh} = 0$.

As the next problem, the effect of openings on the section resistance has been determined. The curves presented in Fig. 6 indicate that a single opening of the size of 44° results in reduction in the section resistance by 30–40% with respect to the normal force n_u and the bending moment m_u.
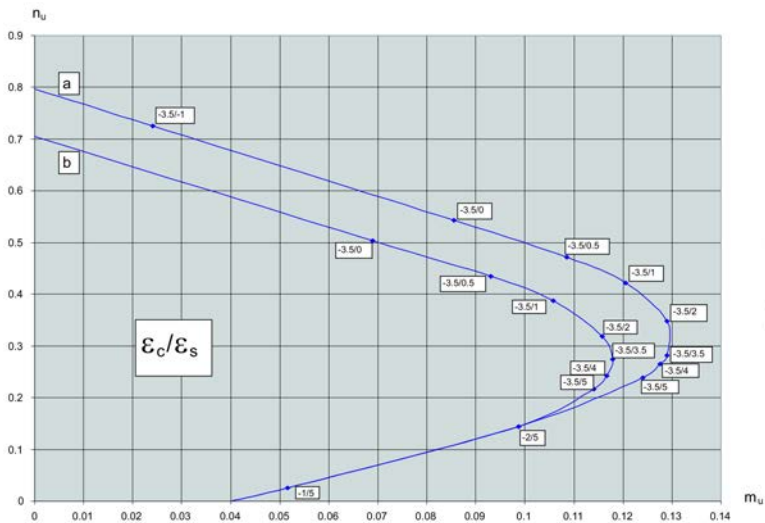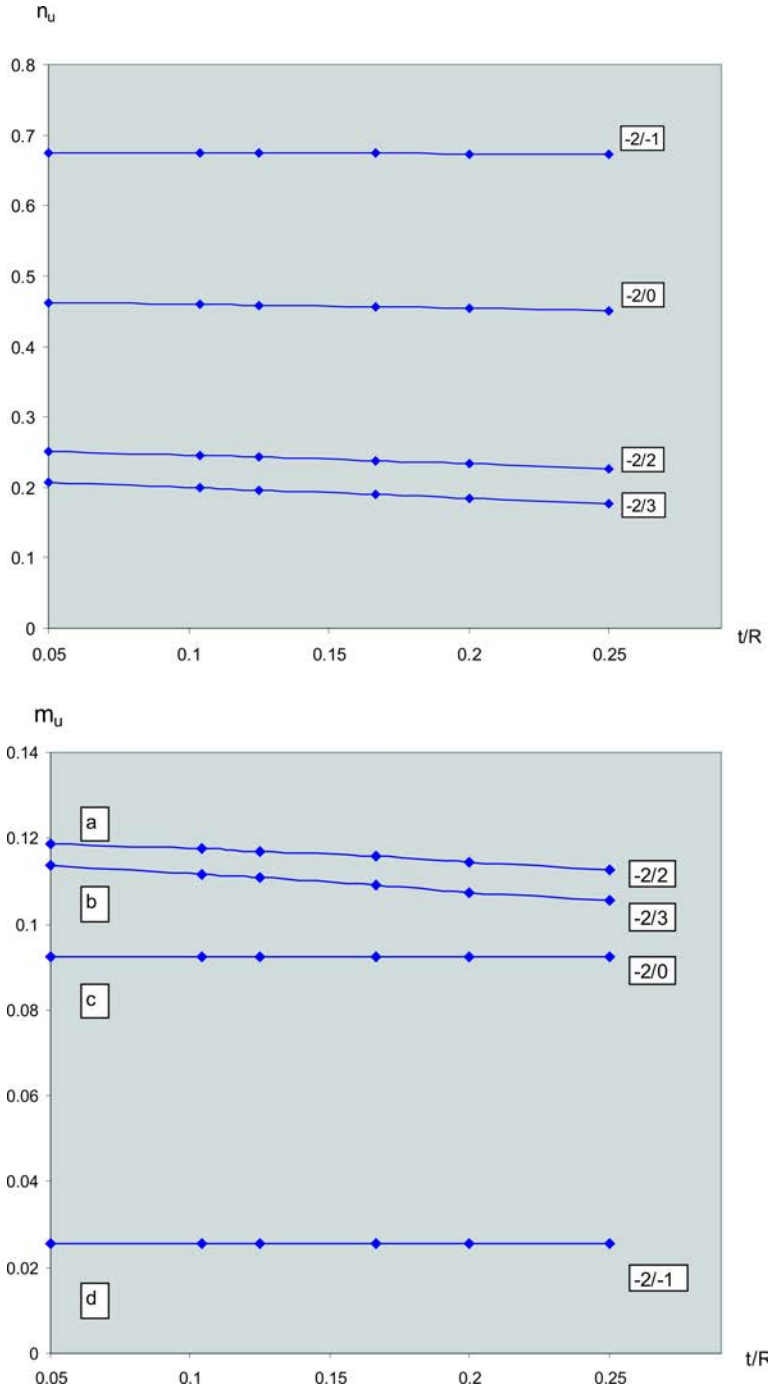
The comparison of the section resistance determined by the stress-strain relationship given by (2.1) with that based on the parabolic-rectangular one is presented in Fig. 7. It shows that the concrete softening in the plastic range results in decreasing the section resistance by 9–11% with respect to n_u and 8–19% with respect to m_u.

In Fig. 8 the values of n_u and m_u are shown as functions of the t/R ratio for different ultimate values ε_{cu} and ε_{su}. The increasing value of t/R ratio results in lower section resistance. It is reduced in the considered range $\langle 0.05; 0.25 \rangle$ by up to 14% with respect to n_u and by up to 7% with respect to m_u.

Table 1. **Comparison of the calculated values with those specified in the DIN 1056 code; $f_{yk} = 420$ MPa, $\gamma_c = 1.5$, $\gamma_c = 1.25$, α – opening size, RD – relative difference.**

Type of Section	α [°]	$\mu \dfrac{f_{yk}}{f_{ck}}$	$\varepsilon_c/\varepsilon_s$	n_u			m_u		
				DIN	Proposed model	RD [%]	DIN	Proposed model	RD [%]
Closed		0.2	$-2/2$	0.260	0.244	6.6	0.14	0.138	1.7
with 1 opening	22	0.2	$-2/1$	0.305	0.293	4.1	0.11	0.108	2.1
with 1 opening	33	0.3	$-2/1$	0.30	0.286	5.1	0.111	0.109	1.4
with 2 openings	22	0.15	$-2/1$	0.30	0.287	4.6	0.10	0.098	1.7
with 2 openings	44	0.1	$-2/4$	0.100	0.105	4.7	0.059	0.0589	0.1

The calculated design values of the normalized, cross-sectional forces n_u and m_u for the sections weakened by one and two openings have been compared with those given according to DIN 1056 [2, 3] (Table 1). The resulting differences do not exceed 7%. In the author's opinion, they result from the differences in the models used and partly from the inaccuracies of reading the DIN diagrams.

5. Conclusions

Based on this study, the following conclusions can be drawn:
1. Using combinatorial approach and the method of mathematical induction, general analytical formulae have been derived for determining the resis-

tance and elasto-plastic analysis of RC annular cross-sections, weakened by an arbitrary number of openings located symmetrically with respect to the bending direction.

2. The obtained solutions are presented in the form of interaction diagrams with the design values of the normalized cross-sectional forces n_u and m_u that can be easily used in structural design.

3. The proposed section model seems to have a wider application field than the previous ones due to the assumptions of non-central layout of reinforcement, additional steel bars at openings and wall edge strains.

4. The resistance of the section increases due to the additional reinforcement at the opening by more than 10%, depending on the opening size and the ultimate values ε_{cu}, ε_{su}.

5. A single opening may result in reduction in the section resistance by 30–40% with respect to the normal force n_u and the bending moment m_u.

6. Concrete softening in the plastic range as well as increasing value of the t/R ratio result in a lower section resistance.

7. The proposed model works well in most cases encountered in engineering practice.

8. The range of validity of the obtained solutions is limited to such number, sizes and locations of openings which assure that plane sections remain plane.

9. If the assumption that plane sections remain plane is not satisfied, the method may still be used provided that the openings are treated as enlarged, as described in the CICIND 2001 Code [4] and the Eurocode EN 13084-2:2006 [7].

10. The model serves for dimensioning the cross-sections and enables to design strenghtening of RC structures by means of the external reinforcement.

References

1. M. Pinfold, *Reinforced concrete chimneys and towers*, Second ed., Viewpoint Publications, London 1984.

2. H. Nieser, V. Engel, *Industrieschornsteine in Massivbau*, Beuth, Berlin 1986.

3. DIN 1056, *Freistehende Schornsteine in Massivbauart*, 1984.

4. CICIND, *Model Code for Concrete Chimneys*, 2001.

5. M. LECHMAN, P. LEWIŃSKI, *Generalized Section Model for Analysis of Reinforced Concrete Chimney Weakened by Openings*, Engineering Transactions, **49**, 1, 4–28, 2001.

6. M. LECHMAN, A. STACHURSKI, *Nonlinear section model for analysis of RC circular tower structures weakened by openings*, Structural Engineering and Mechanics, an International Journal, **20**, 2, May 30 2005.

7. EN-13084-2:2006 *Free-standing chimneys – Part 2: Concrete chimneys.*

SENSITIVITY ANALYSIS IN A FATIGUE DELAMINATION PROBLEM OF AN ELASTIC TWO-LAYER COMPOSITE

Ł. F i g i e l [1)], B. L a u k e [2)], M. K a m i ń s k i [3)]

[1)] **Department of Engineering Science, University of Oxford, Parks Road**
OX1 3PJ, Oxford, United Kingdom

[2)] **Leibniz Institute of Polymer Research Dresden**
Hohe Str. 6, 01069, Dresden, Germany

[3)] **Chair of Mechanics of Materials, Technical University of Łódź**
Al. Politechniki 6, 93-590, Łódź, Poland

Several parameters can affect the fatigue delamination growth in laminates – these include e.g. constituent material properties and/or composite shape. Knowledge about effects of these parameters can lead to a better understanding of the fatigue delamination behaviour and can also pinpoint directions for optimum composite design. These effects can be elucidated by carrying out an appropriate sensitivity analysis. A FEM-based computational approach to sensitivity analysis is proposed in this work to study composite parameter effects in a fatigue delamination problem of an elastic two-layer composite. It is used to calculate and analyse sensitivity gradients of the fracture parameter and fatigue cycle number with respect to composite design parameters such as layer elastic constants. It is observed that sensitivities computed from this approach are generally numerically stable. Obtained sensitivities pinpoint quantitatively the most and least important composite parameters that govern a fatigue delamination process. Sensitivity results are verified by another computational approach and a very good agreement is found.

Key words: layered structures, fatigue delamination, sensitivity analysis, finite element analysis.

1. Introduction

Composite laminates, such as classical fibre-reinforced laminates or hybrid composites, are utilised in many fields of modern engineering, where they are subjected to either static or cyclic (fatigue) loads [1]. The most common mode of failure of these materials is interlaminar fracture (delamination). Delamination growth can lead to a loss of structural integrity and hence – to catastrophic composite failure [2]. Therefore, a large amount of research, both experimental and theoretical, has been already undertaken to better understand that phenomenon under applied static or cyclic loads.

It is known that several factors can affect delamination growth such as environmental conditions, constituent material properties or a component geometry [3–5]. However, to the best knowledge of the authors there has not yet been carried out any detailed research concerning effects of these parameters on the fatigue delamination behaviour of composite laminates. The authors believe that it is necessary for a better understanding of a delamination phenomenon and for further, improved design and optimisation of layered materials. Therefore, an attempt to elucidate the effects of composite parameters is undertaken in this work by exploiting a concept of sensitivity analysis [6].

The sensitivity analysis is an introductory step to structural system optimisation [7] and reliability estimation [8]. Evaluation of sensitivities is a central point of the sensitivity analysis. These sensitivities map the changes of system design parameters (e.g. elastic constants or geometry) onto changes in the system objective parameters such as a composite effective property [9, 10] or composite fatigue life [11]. This in turn provides a relationship between design and objective parameter changes and enables to estimate the significance (or insignificance) of design parameters. This information can further be used in design optimisation of e.g. composite fatigue performance [12] or probabilistic fatigue analysis [13]. The sensitivities can be obtained using various approaches, e.g. by analytical derivation of partial derivatives, by finite difference approximation of partial derivatives, by automatic differentiation of numerical procedure, by computational implementation of explicit differentiation in the finite element method (FEM) codes or some probabilistic approaches [6, 8, 14–19]; utilisation and efficiency of each of these approaches depends on the boundary value problem at hand. From the engineering point of view, the sensitivity analysis is particularly very useful, when it is formulated in the framework of one of the numerical methods such as the finite element method (FEM) or the boundary element method (BEM). The advanced state of the FEM and related software provides a reliable tool for composite analysis, but it gives a composite engineer only little help in identifying the ways to modify composite design to improve the desired qualities. Using the design sensitivity information generated by strategies exploiting the FEM formulation and software, the composite engineer would be able to carry out a systematic trade-off analysis and improve the composite design.

The main goal of this paper is to present a computational approach for calculation and analysis of sensitivities for a fatigue delamination problem of an elastic two-component laminate. This approach combines a fatigue delamination model with the concept of finite differences and it is implemented using the FEM-based program ANSYS. The developed approach is used to compute sensitivities of the total energy release rate and fatigue life, to reveal the most crucial design parameters of a two-component composite laminate. This paper starts with a description of the fatigue delamination model and sensitivity calcu-

lation with finite differences. Further, computer implementation of the approach is presented. A computational illustration utilising a two-component laminate subjected to cyclic shear loads is presented and discussed.

2. Fatigue delamination model and senstivities

A composite system composed of two layers, Ω_1 and Ω_2 is considered here and shown in Fig. 1. The two layers are assumed as isotropic linear-elastic materials defined by the elasticity tensor C_n in terms of two elastic engineering constants, i.e. Young's modulus E_n and Poisson's ratio ν_n, and n denotes the n-th ($n = 1, 2$ in this work). It is assumed that there exists a delamination over some portion of a curved interface between those two layers, denoted by $\Gamma_{c(n)}$. The other part of the curved interface is assumed as perfectly bonded and denoted by Γ_I. The interface itself is assumed to have a vanishing thickness, i.e. $t_I \to 0$ and its curvature is denoted by a radius R_I.
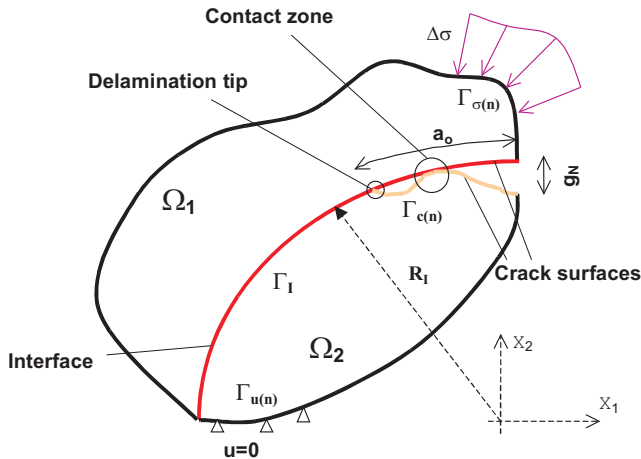

Fig. 1. Two-component model of a delaminated composite laminate.

The composite system is subjected to cyclic loads of constant amplitude $\Delta\sigma = \sigma_{\max} - \sigma_{\min} = \text{const.}$ and load ratio $R = \sigma_{\min}/\sigma_{\max} = 0$ applied to the composite boundary $\Gamma_{\sigma(n)}$ (cf. Fig. 1); $\sigma_{\max}$ and $\sigma_{\min}$ denote the maximum and minimum values of applied loads. The composite is supported on the portion of its boundary denoted by $\Gamma_{u(n)}$ (cf. Fig. 1).

It is assumed that under these boundary conditions the fatigue delamination growth per cycle N can be described by the modified Paris law as follows:

$$(2.1) \qquad \frac{da}{dN} = C(G_T)^m,$$

where G_T is the total energy release rate (the crack driving force parameter) such that $G_T = \Delta G_T = G_{T,\max}$ – it is assumed that the minimum total energy release rate at a cycle does not influence the fatigue delamination growth under $R = 0$ ($G_{T,\min} = 0$). Then, C and m are the empirical constants. The model describes a stable fatigue crack growth along the selected crack path.

Then, two situations that can occur at the delamination tip during propagation under applied fatigue load are considered in this work, i.e. 1) opened and 2) closed delamination tips as shown in Fig. 2.
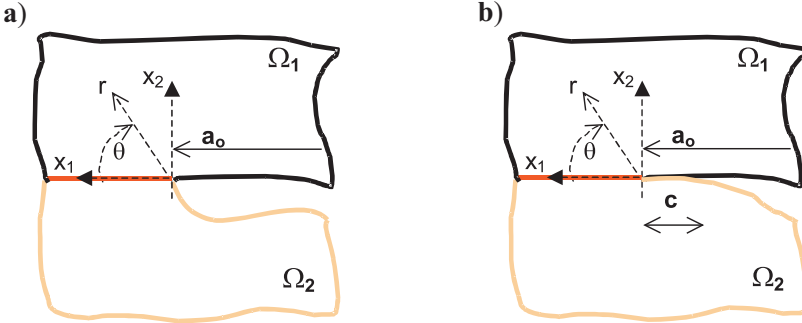

FIG. 2. Near-tip behaviour during fatigue delamination a) opened crack tip
b) closed crack tip.

In the case when the tip is opened during propagation, i.e. when the gap g_N at the tip is larger than zero (cf. Fig. 1), the stress distribution around the tip is assumed to be governed by the so-called oscillatory solution of the linear fracture mechanics for interface cracks [21]. In addition, since the crack propagation along the interface (without kinking out or branching) is analysed here, therefore it is sufficient to account for stresses ahead of the delamination tip i.e. for $\theta = 0$ as follows:

$$(2.2) \qquad \sigma_{22(t)} + i\sigma_{12(t)} = \frac{1}{\sqrt{2\pi r}}(K_1 + iK_2)r_o^{i\varepsilon}\left(\frac{r}{r_o}\right)^{i\varepsilon},$$

where $\sigma_{22(t)}$ and $\sigma_{12(t)}$ denote normal and shear stresses near the delamination tip – since $R = 0$ then $\sigma_{ij(t)} = \Delta\sigma_{ij(t)} = \sigma_{ij(t,\max)}$, where $\sigma_{ij(t,\max)}$ denotes the tip stresses at the maximum applied load during a single cycle. Then, K_1 and K_2 are real and imaginary components of the complex stress intensity factor K, which similarly to crack tip stresses correspond to maximum load in a single cycle. Further, r_o is a characteristic length as an attempt to produce dimensionally meaningful results for K_1 and K_2. Finally, ε is an oscillation index (or mismatch parameter) given as follows [21]:

$$(2.3) \qquad \varepsilon = \frac{1}{2\pi}\ln\left(\frac{1-\beta}{1+\beta}\right),$$

where β is the second Dundurs mismatch parameter given by

$$(2.4) \qquad \beta = \frac{\mu_1 \left(\kappa_2 - 1\right) - \mu_2 \left(\kappa_1 - 1\right)}{\mu_1 \left(\kappa_2 + 1\right) + \mu_2 \left(\kappa_1 + 1\right)},$$

where μ_n is the shear modulus and κ_n denotes the Kolosov constant such that $\kappa_n = 3 - 4\nu_n$ for plane strain conditions and $\kappa_n = (3 - \nu_n)/(1 + \nu_n)$ under plane stress conditions; n denotes the n-th layer.

Then, for the cyclic variation of applied stress and $R = 0$, propagation of a delamination with an opened tip is controlled by the total energy release rate, expressed as follows:

$$(2.5) \qquad G_T = \frac{\left(1 - \beta^2\right)}{E^{\mathrm{eff}}} \left[(K_1)^2 + (K_2)^2\right],$$

where the effective Young's modulus E^{eff} is given by

$$(2.6) \qquad E^{\mathrm{eff}} = \frac{2\overline{E}_1 \overline{E}_2}{\overline{E}_1 + \overline{E}_2},$$

where $\overline{E}_n = E_n \big/ \left(1 - \nu_n\right)^2$ under plane strain conditions and $\overline{E}_n = E_n$ under plane stress conditions. In order to calculate the total energy release rate one needs to know K_1 and K_2. They can be obtained from stresses (Eq. (2.2)) and the well-known Euler relations

$$(2.7) \qquad e^{i\varphi} = \cos\varphi + i\sin\varphi \qquad \text{and} \qquad e^{-i\varphi} = \cos\varphi - i\sin\varphi,$$

as follows:

$$(2.8) \qquad K_1 = \sqrt{2\pi r} \left\{ \sigma_{22(t)} \cos\left(\varepsilon \ln\left[\frac{r}{r_o}\right]\right) + \sigma_{12(t)} \sin\left(\varepsilon \ln\left[\frac{r}{r_o}\right]\right) \right\},$$

$$(2.9) \qquad K_2 = \sqrt{2\pi r} \left\{ \sigma_{12(t)} \cos\left(\varepsilon \ln\left[\frac{r}{r_o}\right]\right) - \sigma_{22(t)} \sin\left(\varepsilon \ln\left[\frac{r}{r_o}\right]\right) \right\}.$$

In the case when the delamination propagates with a closed tip (cf. Fig. 2b), i.e. when the gap g_N at the crack tip equals zero (cf. Fig. 1) and delamination surfaces slide over each other, shear stresses along the interface ahead of the crack tip are assumed to have the following form:

$$(2.10) \qquad \sigma_{12(t)} = \frac{K_2}{(2\pi r)^\lambda},$$

where λ describes a stress singularity that depends on the friction coefficient f in the following way:

$$(2.11) \qquad\qquad\qquad\qquad \cot(\lambda\pi) = f\beta,$$

where β is described by Eq. (2.4).

Then, the delamination propagation with a closed tip under applied cyclic loads of $R = 0$ is governed by the following total energy release rate [22]:

$$(2.12) \qquad G_T = \frac{(K_2)^2 \sin\lambda\pi}{2\gamma(1-\lambda)(2\pi)^{2\lambda}} \Delta a^{1-2\lambda} \left[\frac{\Gamma(2-\lambda)\,\Gamma(1-\lambda)}{\Gamma(3-2\lambda)} - \frac{\cos\lambda\pi}{2(1-\lambda)} \right],$$

where γ is a parameter described in terms of μ_n, κ_n and β and given by

$$(2.13) \qquad\qquad\qquad \gamma = \frac{4\mu_1\mu_2}{\mu_2\kappa_1(1+\beta) + \kappa_2\mu_1(1-\beta) + 2},$$

and $\Gamma(.)$ is the Euler gamma function. The delamination driving force G_T described in Eq. (2.12) is dependent on the crack extension, Δa, which must be finite because G_T diminishes as $\Delta a \to 0$ and $\lambda < 0.5$, while it becomes unbounded as $\Delta a \to 0$ and $\lambda > 0.5$ as reported in [22].

Then, the fatigue life of a delaminated composite can be predicted by integrating Eq. (2.1) from an initial delamination length, a_o, to the one that corresponds to a composite failure, a_f, as follows:

$$(2.14) \qquad\qquad\qquad\qquad N_f = \int_{a_o}^{a_f} \frac{da}{C(G_T)^m}.$$

In order to determine numerically the fatigue cycles number at failure, the delamination length range from a_o to a_f is divided into equal crack increments, $\Delta a = a_{i+1} - a_i$. Hence, the fatigue life is obtained as the sum of all fatigue cycle number increments as follows:

$$(2.15) \qquad\qquad N_f = \sum_{i=1}^{n} N_i \quad \text{and} \quad N_i = \int_{a_i}^{a_{i+1}} \frac{da}{C(G_T(a_i))^m}.$$

As it can be seen directly from Eqs. (2.14) and (2.15), the fatigue life or increment of fatigue cycles depends on the initial delamination length a_o, constants C and m, the crack driving force G_T and material properties such as the n-th layer Young's modulus E_n. The sensitivity analysis allows to estimate the influence of each model parameter on the fracture parameter, fatigue cycle increment during delamination propagation, and finally on the composite fatigue life. In this

work, that influence is estimated in terms of sensitivity gradients (sensitivities). The sensitivity gradients of the composite fatigue life are approximated by the forward finite difference as follows:

$$(2.16) \qquad S = \frac{N_f\left(b_k + \Delta b_k\right) - N_f\left(b_k\right)}{\Delta b_k}$$

or by an alternative expression using the central finite difference

$$(2.17) \qquad S = \frac{N_f\left(b_k + \Delta b_k\right) - N_f\left(b_k - \Delta b_k\right)}{2\Delta b_k},$$

where b_k denotes a nominal value of a design parameter such as E_n or h_n and Δb_k is an infinitesimally small variation of a design parameter about its nominal value b_k.

The main issue related to sensitivity calculations through finite and central difference approaches is the numerical stability (or instability) of sensitivities. Therefore, a proper choice of the design parameter increment, Δb_k, is required. The main advantage of the central finite difference approximation over the forward one is that it allows a larger value of Δb_k to be selected. This also permits avoiding problems associated with small parameter increments, such as numerical round-offs. However in practice, it is usually possible to find an appropriate parameter increment associated with the forward finite difference that provides numerically stable sensitivities.

Eqs. (2.16)–(2.17) express a sensitivity measure, which is inconvenient in cases where sensitivities of N_f with respect to different design parameters must be characterised and compared. Since it is the case in this work, thus, the relative sensitivity or classical sensitivity due to BODE [23] is utilised here and given by

$$(2.18) \qquad S_{\mathrm{rel}} = \frac{\partial(\ln N_f)}{\partial(\ln b_k)} = \frac{\partial N_f/N_f}{\partial b_k/b_k} = \frac{\partial N_f}{\partial b_k}\frac{b_k}{N_f},$$

which provides a dimensionless sensitivity measure appropriate for comparative purposes. It is mentioned that an analogous expression for the fracture parameter G_T can be obtained by replacing N_f.

It must be mentioned that in this work, the sensitivities are calculated with respect to a single parameter change, Δb_k, i.e. only a single design parameter is subjected to a perturbation when the sensitivity is calculated. Calculation of sensitivities, when more than one design parameter is perturbed, would be more general, but it should account for some correlations between particular design parameters. In that case it might be more appropriate to use a probabilistic approach for calculation of sensitivities [24] rather than the current concept.

3. Computer implementation using ANSYS

Efficient numerical evaluation of relative sensitivities, given by Eq. (2.18), demands a development of a numerical approach and its computer implementation. In this work, the FEM is chosen as a tool to solve a boundary value problem for displacements, and then strains and stresses. Hence, the fatigue delamination model and relevant equations for sensitivity measure are combined together and implemented into the FEM-based package ANSYS. In particular, the advantage is taken of the ANSYS Parametric Design Language (APDL), which permits obtaining sensitivities from equations coded up in the postprocessor. Hence, this implementation does not demand any access to the source code of ANSYS.

A numerical strategy proposed to compute sensitivities in this work, is sketched schematically in Fig. 3 and described below in a detail.

Selection
- Design parameter
- Design parameter perturbation
- Delamination growth range
- Delamination increment

FEM-based model
- Model
- Boundary value problem solution

Computation
- Fracture parameter
- Cumulative fatigue cycles number

Computation of absolute sensitivity gradients
- Forward finite difference
- Central finite difference

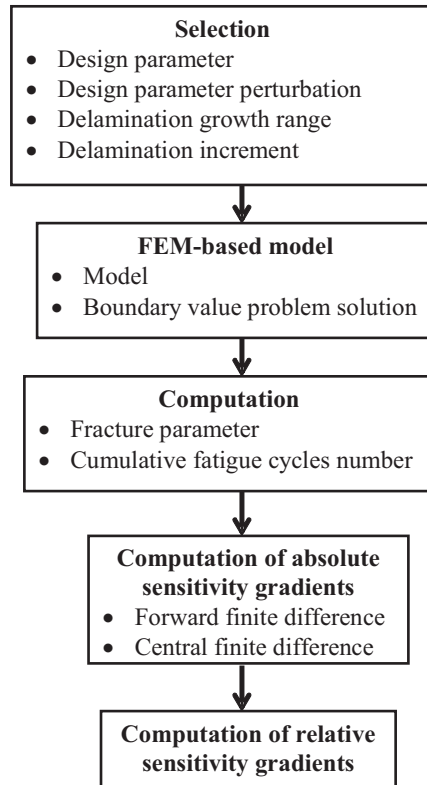**Computation of relative sensitivity gradients**

Fig. 3. Flowchart for computation of sensitivities.

The first step is to select a design parameter (e.g. layer Young's modulus), its perturbation as well as to define delamination propagation range (using a_o and a_f) and delamination increment (Δa_i). In the next step, a FEM model of

the problem must be built using a pre-processor of ANSYS. Each FEM model parameter such as material or geometrical parameter is defined parametrically to allow for a full flexibility for sensitivity computations. Then, a boundary value problem needs to be solved using the FEM for a selected design parameter value and its increment, at required delamination lengths. Hence, considering a two-layer composite with a delamination (Fig. 1) subjected to arbitrarily prescribed loads, one needs to solve the following general differential boundary value problem:

$$\text{(3.1)} \qquad \text{Div}(\boldsymbol{\sigma}_n) = 0 \qquad\qquad\qquad\qquad \mathbf{x} \in \Omega_n,$$

$$\text{(3.2)} \qquad \boldsymbol{\varepsilon}_n = \frac{1}{2}\left[\nabla(\mathbf{u}_n) + \nabla(\mathbf{u}_n)^T\right] \qquad\qquad \mathbf{x} \in \Omega_n,$$

$$\text{(3.3)} \qquad \boldsymbol{\sigma}_n = \mathbf{C}_n \boldsymbol{\varepsilon}_n \qquad\qquad\qquad\qquad \mathbf{x} \in \Omega_n,$$

$$\text{(3.4)} \qquad \boldsymbol{\sigma}_n \mathbf{n}_n = \mathbf{t}_n \qquad\qquad\qquad\qquad \mathbf{x} \in \Gamma_{\sigma(n)},$$

$$\text{(3.5)} \qquad \mathbf{u}_n = 0 \qquad\qquad\qquad\qquad\qquad \mathbf{x} \in \Gamma_{u(n)},$$

$$\text{(3.6)} \qquad \tau = f|p| \qquad \text{for} \qquad g_N \le 0 \qquad \mathbf{x} \in \Gamma_{c(n)},$$

$$\text{(3.7)} \qquad \tau = p = 0 \qquad \text{for} \qquad g_N > 0 \qquad \mathbf{x} \in \Gamma_{c(n)},$$

where $\boldsymbol{\sigma}_n = \boldsymbol{\sigma}_n(b_k)$ is the stress tensor at a point in the interior of the n-th composite constituent Ω_n; $\boldsymbol{\varepsilon}_n = \boldsymbol{\varepsilon}_n(b_k)$ is the strain tensor written in terms of the displacement field in $\mathbf{u}_n = \mathbf{u}_n(b_k)$; $\mathbf{n}_n$ is the unit vector that is normal to the surface of the composite constituent; $\mathbf{t}_n$ denotes the applied surface tractions on $\Gamma_{\sigma(n)}$; f is the friction coefficient that approximates roughness of delaminated composite parts (contact surfaces); p and τ denote the contact pressure and frictional stresses along the crack surfaces remaining in contact.

The boundary value problem (3.1)–(3.7) is complemented by conditions of stress equilibrium (normal and shear components only) and continuity of displacement across the uncracked portion of the interface, denoted by Γ_I. It should be mentioned that the boundary value problem presented above is general, and its specific form, i.e. under prescribed shear loads, is solved using ANSYS in this work.

The problem is primarily solved for displacements, and then strains and stresses are computed for each value of the design parameter b_k. Then, the total energy release rate, G_T, can be obtained using crack-tip stresses from Eqs. (2.8)–(2.9), what in turn enables calculation of the fatigue cycles number, N_f. It is mentioned that stress intensity factors K_1 and K_2 required to calculate

G_T are obtained by a linear extrapolation of stress intensity factors determined at finite element nodes at $\theta = 0$ over a selected distance r (cf. Fig. 2). The extrapolation technique is based on the least squares method to give

$$(3.8) \qquad K_{1,2} = \frac{\sum\limits_{i=1}^{n_k} K_{i(1,2)} - d \sum\limits_{i=1}^{n_k} y_i}{n_k},$$

where

$$(3.9) \qquad d = \frac{n_k \left(\sum\limits_{i=1}^{n_k} K_{i(1,2)} y_i \right) - \left(\sum\limits_{i=1}^{n_k} K_{i(1,2)} \right) \left(\sum\limits_{i=1}^{n_k} y_i \right)}{n_k \left(\sum\limits_{i=1}^{n_k} y_i^2 \right) - \left(\sum\limits_{i=1}^{n_k} y_i \right)^2},$$

where y_i is the distance between the i-th node n_i and the delamination tip; n_k is the number of nodes used in the extrapolation of nodal stress intensity factors $K_{i(1,2)}$.

The boundary value problem described by Eqs. (3.1)–(3.7) is solved for a selected design parameter at subsequent crack lengths until the final delamination length a_f is reached. When that is the case, the entire procedure (i.e. solution of the boundary value problem and fracture parameter calculation as well as fatigue cycle increment) is repeated for a new design parameter increment. This is done to study the numerical stability of sensitivities calculated from the finite difference concept. Results of calculations, in terms of the fracture parameter and fatigue cycle number are written to output files at each delamination length and design parameter increment. After the computational procedure is completed for the last design parameter increment, then sensitivity calculations begin. The absolute sensitivities are calculated first, using forward and/or central finite difference methods. Then, relative sensitivities are obtained by appropriate scaling of absolute sensitivities according to Eq. (2.18). The entire computational process is repeated for all design parameters of interest. That process is coded up into ANSYS such that it does not need any user interference, when sensitivities are calculated for a single design parameter – i.e. the computational process is run automatically at each delamination length and design parameter perturbation until $a = a_f$. However for the time being, a change in the design parameter (e.g. Young's modulus) to the layer thickness must be done manually by the user.

The solution of the boundary value problem is the most expensive step of the approach, in terms of computational time. It will obviously be less expensive for linear elastic problem, while the computational costs will increase with introduction of geometrical and physical nonlinearities.

4. Computational example

4.1. FEM model

Accuracy and applicability of the approach presented in the Sec. 3 is evaluated on an example related to a two-component boron/epoxy-aluminium (B/Ep-Al) curved composite (cf. Fig. 4). This composite laminate represents a simplified repeated element of a hybrid-like composite laminate, which is utilised in aerospace applications – frequently in large curved parts of the aircraft fuselage. Both layers have the same nominal thickness $h_1 = h_2 = 2.5 \times 10^{-3}$ m, then composite width is $w = 5 \times 10^{-3}$ m, while the interface curvature is described by the nominal radius value $R_I = 5.25 \times 10^{-2}$ m. B/Ep component is considered as a linear elastic and isotropic material with the Young modulus $E_1 = 207$ GPa and Poisson's ratio $\nu_1 = 0.21$. This is only a rough approximation to the real situation where B/Ep component behaves as an anisotropic and viscoelastic material, depending on the volume fraction of the boron reinforcement. The Al component is also considered as linear elastic and isotropic with the corresponding material properties $E_2 = 70.8$ GPa and $\nu_1 = 0.33$. Here the real situation is simplified by assuming that the yield stress of aluminum is very high. The interface is modelled as a zero thickness layer with no assigned material properties.
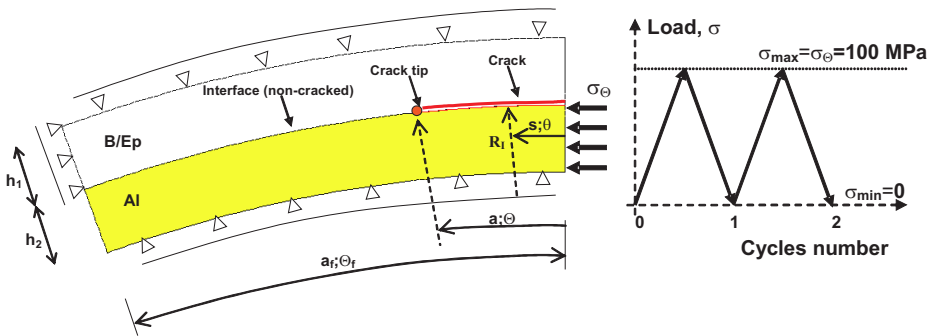

FIG. 4. Two-layer boron/epoxy-aluminium curved composite under cyclic shear.

The composite structure contains an initial delamination of length $a = a_o = 5.498 \times 10^{-3}$ m ($\Theta = \Theta_o = 6$ deg) located at the interface between layers. Then, the total interface length, including cracked and perfectly bonded parts of the interface, is equal to $a = a_f = 1.835 \times 10^{-2}$ m ($\Theta = \Theta_f = 20$ deg). The nominal value of the interface friction coefficient is selected arbitrarily and equal to $f = 0.05$. Then, the nominal value of the fatigue law exponent is equal to $m = 10$. The nominal value of the fatigue law constant is equal to $C = 1 \times 10^{-29}$ and it was evaluated based on the knowledge of the total energy

release rate threshold, $G_{T,th} = 100$ J/m^2 as well as the delamination growth threshold, $(da/dN)_{th} = 1 \times 10^{-9}$ m/cycle according to the concept reported in [25].

The composite laminate is subjected to cyclic shear loads with a triangular profile shown in Fig. 4. Shear type of loading is designed by constraining composite edges in the radial direction and additionally imposing supports on the upper component in the angular direction. The cyclic load of $\sigma_\Theta = 100$ MPa is applied to lower composite constituent (with thickness h_2) in the angular direction. It is noted that the aforementioned boundary conditions simulate those of a proposed compression shear fracture test for curved and flat layered specimens [26].

Both layers are discretised by eight-node solid elements PLANE82, while the crack surfaces – by contact elements pairs CONTA172-TARGE169 as shown in Fig. 5. The mesh is designed here in such a way that the contact elements number changes only along with the crack length from 42 ($a/a_o = 1$) to 94 ($a/a_o = 3.167$), while the solid elements number is fixed and equal to 2224. Special attention is focused on the discretisation of the near-tip domain to simulate properly the stress singularity. A single row of quarter-point elements with radius $r_1 = 1 \times 10^{-6}$ m discretises the crack tip vicinity and the mesh becomes coarser far away from the crack tip as shown in Fig. 5. Investigation of the influence of different r_1 values on the total energy release rate is shown in the following subsection.
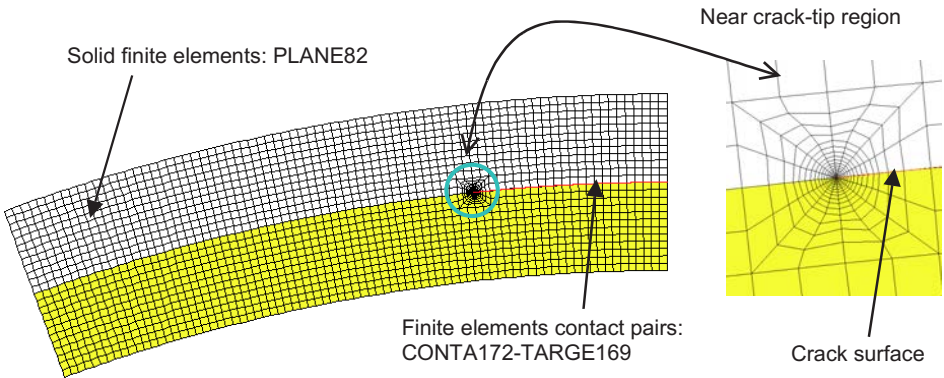

Fig. 5. FEM discretisation of composite domain and crack surfaces.

The augmented Lagrange method implemented in ANSYS was utilised to compute contact constraints. Computation of frictional stresses and resulting slip was possible with the so-called radial return algorithm available in ANSYS. Solution was obtained *via* the full Newton–Raphson incremental-iterative technique, and the line search option was used to enhance the solution convergence.

4.2. Total energy release rate

Accurate calculation of the total energy release rate is a key step in determination of fatigue cycle number and then proper evaluation of relative sensitivities of fracture parameter and fatigue life. Therefore, results obtained from the current model are verified by those obtained using the virtual crack closure method (VCCM) as reported in [27]. Mixed mode formulation of the VCCM for singular elements is used. Results are compared for three different values of $r_1 = 0.5 \times 10^{-6}$, 1×10^{-6} and 5×10^{-6}. It must be mentioned that a careful investigation of the delamination growth revealed that the crack tip was opened for all crack lengths under the considered boundary conditions. However, the delamination was opened only in the vicinity of the crack tip, while delaminated surfaces were in frictional contact with each other, away from the crack tip.

Table 1. Comparison of the fracture parameter G_T for $a/a_o = 1$.

r_1 [m]	G_T [J/m^2] (from Eq. (2.5))	G_T [J/m^2] (from the VCCT)
5×10^{-6}	123.826	118.603
1×10^{-6}	121.648	120.579
0.5×10^{-6}	120.661	127.466

Therefore, the fracture parameter was computed from Eq. (2.5) and its results are verified against those obtained from the VCCT, and shown in Table 1 for the normalised crack length $a/a_o = 1$. In addition, the fracture mode 2 of the fracture parameter, G_2, prevails for all crack lengths, so $G_T \approx G_2$. Fracture parameter values obtained from Eq. (2.5) are only slightly sensitive to the value of r_1 as shown in Table 1, contrary to those obtained from the VCCT, which increase as r_1 decreases. However, a good agreement between these two approaches is obtained for $r_1 = 1 \times 10^{-6}$. Therefore, the total energy release rate determined from Eq. (2.5) and that value of r_1 is used in all sensitivity calculations.

4.3. Interpretation of sensitivity analysis results

Interpretation of sensitivity results is presented with some selected examples, where the relative sensitivity S_{rel} of the total energy release rate and the fatigue cycles number is obtained with respect to composite parameters. The sensitivities are calculated for three different parameter increments, 0.1%, 1% and 10%. A simple engineering interpretation of relative sensitivity gradients of the fracture parameter and fatigue cycle number, is that if a particular gradient is less than 0, an increase of composite parameter (e.g. layer Young's modulus) accompanies the reduction of the objective parameter (fracture parameter and/or fatigue cycle number). Otherwise (the relative sensitivity greater than 0), an increase of the design parameter results in an appropriate increase of the objective

parameter. Ultimately, if the sensitivity is comparable to 0, then the given design parameter does not influence the objective parameter.
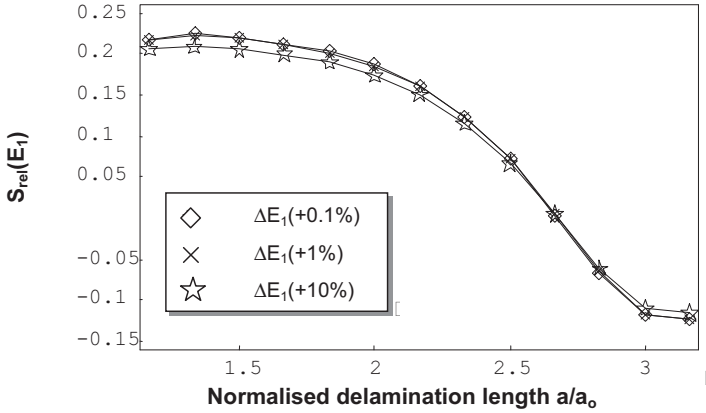

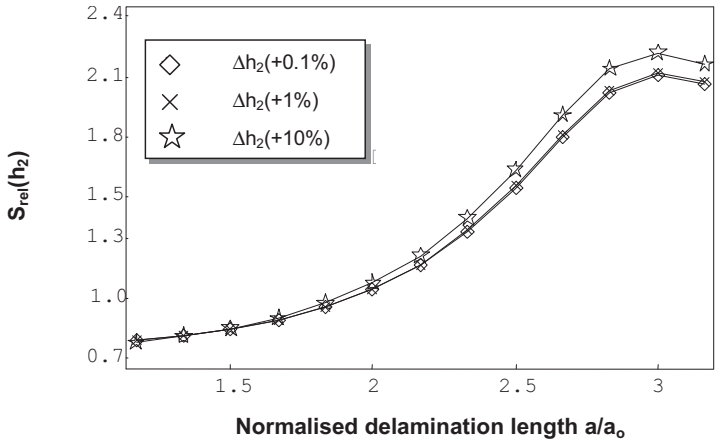FIG. 6. Relative sensitivities of the fracture parameter with respect to the Young's modulus E_1.

FIG. 7. Relative sensitivities of the fracture parameter with respect to the layer thickness h_2.

For example, results of relative sensitivities of the total energy release rate with respect to the Young's modulus of the upper layer $S_{\text{rel}}(E_1)$, thickness of the lower layer $S_{\text{rel}}(h_2)$ and the interface radius $S_{\text{rel}}(R_I)$, are shown in Figs. 6–8, as functions of a normalised delamination length, a/a_o. This enables to demonstrate evolution of relative sensitivities as the crack propagates. An interesting behaviour is shown in Fig. 6, where the relative sensitivity is positive at short delamination lengths and then changes its sign for large crack lengths. Thus, an increase of the upper layer Young modulus leads to an increase of the fracture

parameter at short delamination lengths, whereas an opposite situation (reduction of the fracture parameter for increasing Young's modulus) is observed at large crack lengths. Hence, there exists a point where the sensitivity equals zero so the fracture parameter value is not affected by the change of the investigated design parameter (the upper layer Young's modulus in this case). Then, the relative sensitivities of the total energy release rate with respect to the thickness of the lower layer, h_2, are shown in Fig. 7. It is possible to observe from that figure that the fracture parameter increases with increasing layer thickness. Additionally, the relative sensitivities increase as the delamination propagates. A similar situation is observed in Fig. 8, where the relative sensitivities are positive during nearly entire range of crack growth (excluding some numerical instabilities near the shortest delamination length). However, a quantitative difference between results in Figs. 7 and 8 is observed. The relative sensitivities obtained with respect to the lower layer thickness (Fig. 7) are larger, at the order of two, than those calculated with respect to the interface radius (Fig. 8).
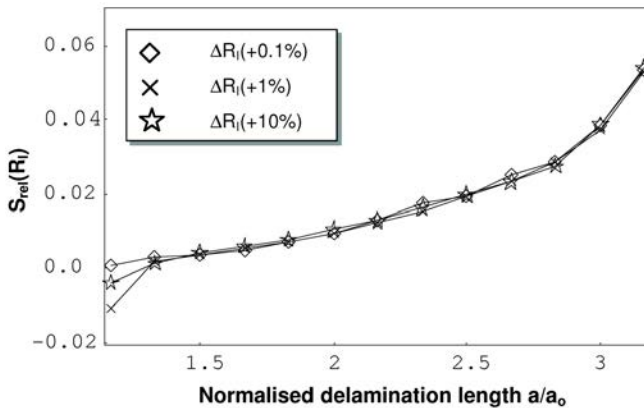

FIG. 8. Relative sensitivities of the fracture parameter with respect to the interface radius R_I.

Relative sensitivity results shown in Figs. 6–8 demonstrate usefulness of the sensitivity analysis in general. In particular, they enable to pinpoint exactly the importance of a particular composite parameter. In order to show that aspect in a more detail, the relative sensitivities of the fatigue cycles number were calculated with respect to several parameters and compared. Outcome of these computations is shown in Table 2 as a function of the normalised delamination length. Thus, the importance of each design parameter on the fatigue cycle number can be compared at consecutive delamination lengths. Here, it is only focused on the sensitivity values obtained at the largest crack length (last line of Table 2 marked in bold). These sensitivities enable to judge the importance of each parameter on the fatigue life of the analysed composite. It is shown in

Table 2 that two parameters associated with the lower component of the composite, i.e. Young's modulus E_2 and the thickness h_2, are the most significant parameters for the fatigue life. In particular, positive value of the relative fatigue life sensitivity gradient, $S_{\mathrm{rel}}(E_2)$, corresponds to the fact that an increase in the lower layer Young's modulus extends considerably the composite fatigue life. This is directly connected with the fact that by increasing the lower layer Young's modulus, E_2, the normalised crack tip opening and tangential displacements decrease, as shown in Figs. 9 and 10 for two normalised crack lengths as a function of the arc length s ($s = 0$ for $a = 0$). This in turn, results in a reduction of stress component values around the crack tip (interestingly without a change of stress distribution) as shown in Fig. 12 for a single normalised delamination length, and compared with the reference (unperturbed) stress values in Fig. 11. Reduction of crack tip displacements and near tip stresses leads to a reduction of the crack driving force (total energy release rate), as demonstrated later, in Figs. 13 and 14, by negative values of relative sensitivities of the fracture parameter with respect to the lower layer Young's modulus, E_2. Hence, altogether it leads to the conclusion that delamination demands more loading cycles to propagate from a_o to a_f with increasing E_2. Thus, an increase in the component stiffness ratio E_2/E_1 might retard the fatigue failure of the analysed composite.

Table 2. Relative sensitivity gradients of the fatigue cycles number (parameter perturbation +1%).

| a/a_o	$S_{\mathrm{rel}}(E_1)$	$S_{\mathrm{rel}}(E_2)$	$S_{\mathrm{rel}}(\nu_1)$	$S_{\mathrm{rel}}(\nu_2)$	$S_{\mathrm{rel}}(h_1)$	$S_{\mathrm{rel}}(h_2)$	$S_{\mathrm{rel}}(\mu)$	$S_{\mathrm{rel}}(R_I)$
1.167	-2.292	12.957	-1.662	3.016	-3.220	-8.732	0.814	-1.467
1.333	-2.210	13.060	-0.878	3.171	-3.202	-8.119	0.808	-0.638
1.500	-2.204	13.024	-0.620	3.216	-3.228	-8.004	0.918	-0.412
1.667	-2.192	12.993	-0.493	3.266	-3.258	-8.034	1.011	-0.305
1.833	-2.171	12.959	-0.415	3.312	-3.286	-8.144	1.096	-0.247
2.000	-2.139	12.914	-0.366	3.349	-3.313	-8.317	1.173	-0.215
2.167	-2.097	12.860	-0.333	3.372	-3.334	-8.535	1.238	-0.198
2.333	-2.049	12.801	-0.312	3.381	-3.347	-8.767	1.287	-0.191
2.500	-2.006	12.749	-0.300	3.378	-3.352	-8.957	1.316	-0.189
2.667	-1.982	12.721	-0.295	3.372	-3.351	-9.058	1.327	-0.189
2.833	-1.975	12.713	-0.294	3.370	-3.349	-9.082	1.329	-0.189
3.000	-1.974	12.713	-0.294	3.370	-3.349	-9.084	1.329	-0.189
3.167	-1.974	12.713	-0.294	3.370	-3.349	-9.084	1.329	-0.189
3.333	$\mathbf{-1.974}$	$\mathbf{12.713}$	$\mathbf{-0.294}$	$\mathbf{3.370}$	$\mathbf{-3.349}$	$\mathbf{-9.084}$	$\mathbf{1.329}$	$\mathbf{-0.189}$
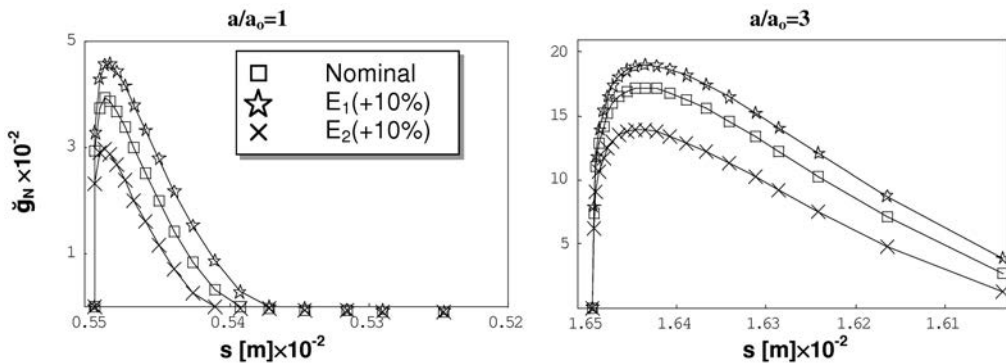
FIG. 9. Effects of Young's moduli variations on delamination tip opening displacements.
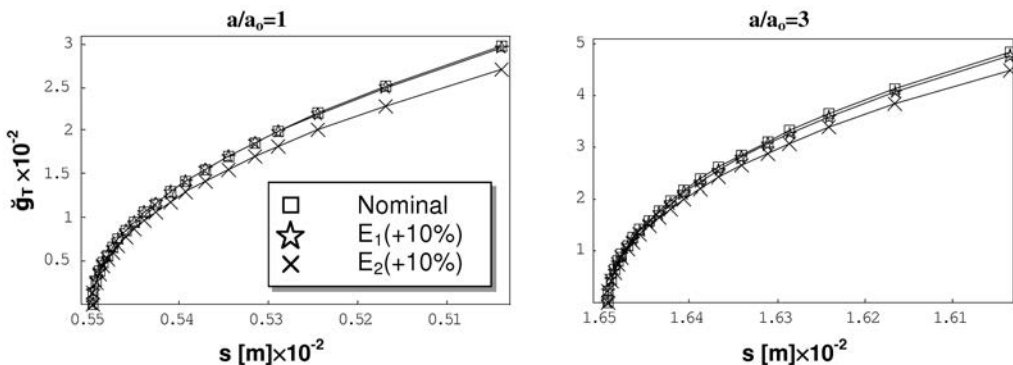

FIG. 10. Effects of Young's moduli variations on delamination tip tangential displacements.
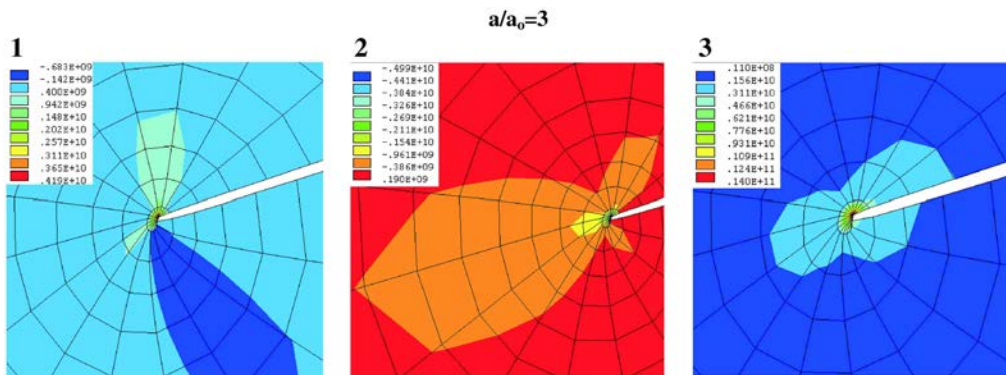

FIG. 11. Near-tip stress distribution for nominal design parameter values [Pa]
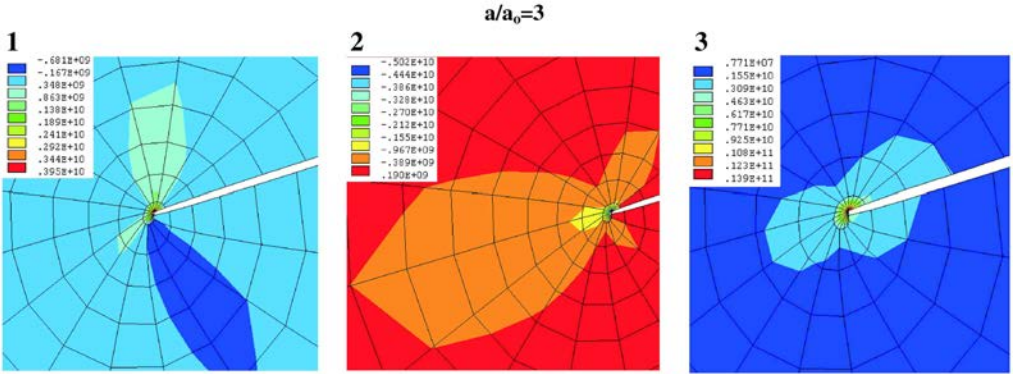(1) normal (2) shear (3) von Mises.

FIG. 12. Near-crack tip stress distribution $(+\Delta E_2 = 10\%)$ [Pa]
(1) normal (2) shear (3) von Mises.

Then, it has been already mentioned that the lower layer thickness, h_2, is the next, after E_2, most important composite parameter that affects the composite fatigue life. However, it is not yet fully clear if the high value of the relative sensitivity is actually because of a large significance of that composite parameter, or it is rather caused by an increase in a load area. The latter fact obviously implies larger forces acting on the composite, that increase considerably the crack tip displacement and near tip stresses, and thereby the crack driving force. This leads finally to a serious reduction of the composite fatigue life. This issue must be investigated further, to conclude about an actual importance of h_2 on the composite fatigue life. It can be carried out by replacing the force (stress)-controlled loading conditions by displacement (strain)-controlled ones, hence avoiding any change in load when perturbing h_2. Finally, the least important composite parameters are the interface radius and the Poisson's ratio of the lower component, R_I and ν_1, respectively. The lack of significance of ν_1 and especially R_I is caused by the specific boundary conditions considered in this work. In a more general (complex) case of boundary conditions such as bending or compression, one might expect a much larger significance of composite curvature. Hence, the next step in application of the sensitivity analysis to composite fatigue delamination problems should consider other, more general boundary conditions.

It is believed that the information shown in Table 2 (particularly in the last line) might help a composite engineer to choose appropriate design directions to optimise the fatigue fracture performance of the composite. However, at the time being one should be careful with a direct translation of these results into design. It is due to the fact that the composite models used here, do not include other important composite parameters such as those connected with all inelastic damage micro-phenomena. Nevertheless, a change (enrichment) of the model

will not change the sensitivity approach presented in this work. It will solely introduce new design parameters in calculations. Hence, the results should be more useful with respect to composite design and optimisation.

4.4. Numerical stability of sensitivity analysis results

An important issue of sensitivity computations with the finite difference approach is the numerical stability of calculated sensitivities. Therefore, this aspect is briefly discussed herein. In order to analyse it, the sensitivities are calculated with respect to three different composite parameter increments, as it has been already mentioned above, i.e. promiles (0.001), percents (0.01) and tenths (0.1). Most of the sensitivities showed a very good numerical stability, i.e. the sensitivities computed for different parameter increments were nearly the same and did not show any oscillations (cf. Figs. 6–8). However, there were some cases in which the sensitivities were affected by parameter increments, as it is shown e.g. in Fig. 13 for the Young's modulus of the lower layer, E_2. In that case, the sensitivities obtained for the largest parameter increment $(+10\%)$ were different from those calculated for smaller increments $(+0.1$ and $1.0\%)$. Thus, the design parameter change equal to $+10\%$ was too large in the problem at hand to obtain reliable sensitivities. Therefore, the sensitivities were calculated once more for three increments using the central finite differences. The outcome is shown in Fig. 14, where the parameter-increment dependence is absent as compared with Fig. 13. Thus, on the one hand it shows that the dependences are caused by too large parameter increments, which is a common feature associated with an application of the forward finite difference approach. On the other hand, it points out that if any numerical instabilities arise due to the utilisation of that approach, then a user might avoid it by switching it to the central finite differences.
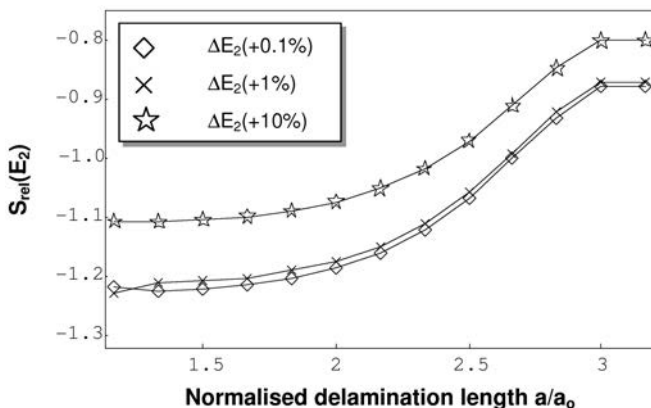

Fig. 13. Relative sensitivities of the fracture parameter with respect to the Young's modulus E_2 – forward finite difference.
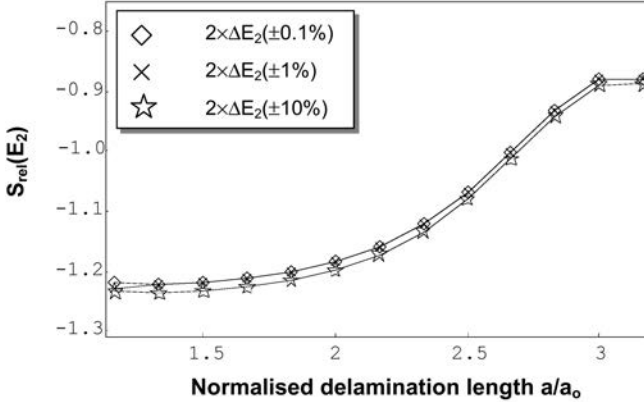
FIG. 14. Relative sensitivities of the fracture parameter with respect
to the Young's modulus E_2 – central finite difference.

In general it was observed that the relative sensitivities of G_T and N_i obtained from the forward difference approach showed a good numerical stability for the parameter increment $(+1\%)$.

4.5. Verification of relative sensitivities

Another important aspect was to verify the accuracy of calculated relative sensitivities with other existing approaches. Since no closed-form solution related to the problem considered was found, the numerical probabilistic approach reported in [24] was taken as a reference case. The reference approach is based on the Monte–Carlo simulation concept that helps to generate a design parameter spectrum according to a specified statistical distribution. Then, FEM-based simulations are run for each generated parameter from which the corresponding fracture parameters are calculated. Then, functions describing relations between the design and objective parameters (such as crack driving force) are numerically evaluated, differentiated with respect to a design parameter and normalised to obtain relative sensitivities.

Herein, the relative sensitivity values of the total energy release rate with respect to the Young's modulus of the lower layer, E_2, are compared. Results from both approaches are collected in Table 3 as a function of the normalised delamination length. The sensitivities from the current (finite-difference) approach were calculated for the parameter increment $+1\%$.

It is shown in Table 3 that results from both approaches are in a very good agreement – sensitivities obtained from the reference approach are only slightly higher, especially for larger delamination lengths. This confirms the conclusion that current sensitivity calculations are correct from the computational point of view.

Table 3. Relative sensitivities of the total energy release rate G_T.

a/a_o	$S_{\text{rel}}(E_2)$	
	Current approach	Reference approach
1.0	-1.210	-1.230
1.167	-1.228	-1.226
1.333	-1.211	-1.225
1.5	-1.207	-1.220
1.667	-1.200	-1.214
1.833	-1.190	-1.203
2.0	-1.173	-1.186
2.167	-1.148	-1.160
2.333	-1.110	-1.122
2.5	-1.058	-1.069
2.667	-0.992	-1.003
2.833	-0.923	-0.933
3.0	-0.923	-0.933
3.167	-0.872	-0.933
3.333	-0.872	-0.933

5. Conclusions

A computational approach to sensitivity analysis was proposed in this work to study composite parameter effects in a fatigue delamination problem of a two-layer composite. The main conclusions that stem from this work are as follows:

1. The calculated relative sensitivities enabled to point out, both qualitatively as well as quantitatively, the importance (or lack of importance) of composite parameters, such as layer Young's modulus or thickness, on the fatigue life of a delaminated composite subjected to shear fatigue loads of constant amplitude. Results of the current investigation revealed an important fact that the relative sensitivities of the fracture parameter and fatigue cycle number are not constant but vary during delamination growth.

2. Relative sensitivities determined by the forward finite difference concept showed a satisfactory numerical stability – i.e. results were generally independent of the composite parameter increment. In cases where relative sensitivity results were parameter increment-dependent, the application of the central finite difference concept improved considerably their numerical

stability. However, in nearly all cases it was possible to find the appropriate parameter increment when using the forward finite differences.

3. Relative sensitivity values obtained from the current approach were verified and found to be in a very good agreement with relative sensitivity results of a sample-based approach to sensitivity analysis.

4. ANSYS post-processing environment appeared as a very convenient tool in implementing and executing the sensitivity analysis by solely using its parametric design language without a direct access to its source code. More computational details and parts of the implementation can be found in [20].

5. Actually it is not possible to conclude that the current approach can be applied to carry out the sensitivity analysis of other delamination problems in composite laminates. Therefore, it would be interesting and necessary to consider other, more general, boundary conditions such as cyclic bending or compression. This issue is left for future research.

References

1. B. Harris [Ed.], *Fatigue in Composites*, CRC Press/Woodhead Publishing, 2003.

2. A. C. Garg, *Delamination – a damage mode in composite structures*, Eng. Fract. Mech., **29**, 557–584, 1988.

3. V. V. Bolotin, *Mechanics of Fatigue*, CRC Press, 1999.

4. Ł. Figiel, M. Kamiński, *Mechanical and thermal fatigue delamination in curved layered composites*, Comput. Struct., **81**, 1865–1873, 2003.

5. Ł. Figiel, N. E. Zafeiropoulos, B. Lauke, *Numerical analysis of the elastic constants' effects on the delamination propagation in a curved layered composite beam under cyclic shear loading*, Compos. Part A Appl-S, **A36**, 153–162, 2005.

6. H. J. Haug, K. K. Choi, V. Komkov, *Design Sensitivity Analysis of Structural Systems*, Academic Press, 1986.

7. S. Kibsgaard, *Sensitivity analysis – the basis for optimisation*, Int. J. Numer Meth. Eng., **34**, 901–932, 1992.

8. M. Kleiber, H. Antunez, T. D. Hien, P. Kowalczyk, *Parameter Sensitivity in Nonlinear Mechanics: Theory and Finite Element Computations*, John Wiley & Sons, 1997.

9. M. Kamiński, *Computational mechanics of composite materials. Sensitivity, randomness and multiscale behaviour*, Springer Verlag, 2005.

10. J. Fish, A. Ghoualli, *Multiscale analytical sensitivity analysis for composite materials*, Int. J. Numer. Meth. Eng., **50**, 1501–1520, 2001.

11. Ł. Figiel, M. Kamiński, *Fatigue sensitivity analysis for the curved composite beam*, pp. 477–484, [in:] *Brittle Matrix Composites 7*, A. M. Brandt, V. Li, I. C. Marshall [Eds.], Woodhead Publishing,2003.

12. M. E. M. El-Sayed, E. H. Lund, *Structural optimization with fatigue life constraints*, Eng. Fract. Mech., **37**, 1149–1156, 1990.

13. M. KAMIŃSKI, *On probabilistic fatigue models for composite materials*, Int. J. Fatigue, **24**, 477–495, 2002.

14. J. S. ARORA, *Introduction to Optimum Design*, 2-nd Edition, Academic Press, 2004.

15. E. LAPORTE, P. LE TALLEC, *Numerical Methods in Sensitivity Analysis and Shape Optimisation*, Birkhäuser, Boston 2003.

16. A. GRIEWANK, *Evaluating Derivatives: Principles and Techniques of Algorithmic Differentiation*, Frontiers in Applied Mathematics 19, SIAM, 2000.

17. E. LUND, *FEM-based Design Sensitivity and Optimisation*, PhD thesis, Aalborg University, Denmark, 1994.

18. T. BURCZYŃSKI, *Applications of BEM in sensitivity analysis and optimisation*, Comput. Mech., **13**, 29–44, 1993.

19. K. DEMS, Z. MRÓZ, *Sensitivity analysis methods* [in Polish], pp. 647–721, [in:] *Handbook of Computational Solid Mechanics*, M. KLEIBER [Ed.], PWN, 1995.

20. Ł. FIGIEL, *Sensitivity analysis of interface fatigue crack propagation in elastic composite laminates*, PhD Thesis, Technical University of Dresden, SLUB Dresden, 2004.

21. J. W. HUTCHINSON, Z. SUO, *Mixed Mode Cracking in Layered Materials*, Adv. Appl. Mech., **29**, 63–191, 1992.

22. W. QIAN, C. T. SUN, *A frictional interfacial crack under combined shear and compression*, Composites Sci Technol., **58**, 1753–1761, 1998.

23. P. M. FRANK, *Introduction to System Sensitivity Theory*, Academic Press, 1978.

24. Ł. FIGIEL, M. KAMIŃSKI, *Deterministic and probabilistic sensitivity analysis of fatigue fracture for a curved two-layer composite*, Lecture Series on Computer and Computational Sciences, **4**, 1062–1064, Brill Academic Publishers, Leiden 2005.

25. J. SCHÖN, *A model of fatigue delamination in composites*, Composites Science and Technology, **60**, 553–558, 2000.

26. Ł. FIGIEL, M. KAMIŃSKI, B. LAUKE, *Analysis of a compressive shear fracture test for curved interfaces in layered composites*, Eng. Fract. Mech., **71**, 967–980, 2004.

27. I. S. RAJU, *Calculation of strain-energy release rates with higher order and singular finite elements*, Engineering Fracture Mechanics, **28**, 3, 251–274, 1987.